Norwegian University of Life Sciences

Master's Thesis 2020 30 stp.
Faculty of Science and Technology

Alkaline fuel cell system fed with hydrogen derived from ammonia, for electric power and heat generation during the winter season in Longyearbyen

Alkalisk brenselcellesystem drevet av hydrogen lagret i ammoniakk, for produksjon av elektrisk energi og varme under vinterhalvåret i Longyearbyen.

Pål Denstad
Mechanics and Process Technology

Denne oppgaven e skreve te min lille Tiger. Takk førr all støtte du har gidd mæ under arbeie me denne oppgaven. Æ e veldig gla i dæ!

- lille Bjørn

Preface

This master thesis is written at the Faculty of Science and Technology at the Norwegian University of Life Sciences (NMBU), during the spring semester of 2020. The project case was presented to me by the Advisor of Energy Conversion at Longyearbyen Community Council, as part of their ongoing search for a new energy system.

First, I would like to thank my supervisor, associate Professor Volha Shapaval at NMBU, for her guidance and advice throughout the work with this thesis. I would also want to thank co-supervisors Rasmus Bøckman, Advisor of Energy Conversion at Longyearbyen Community Council, and Petter H. Heyerdahl, associate Professor at NMBU, for presenting me with this opportunity and having valuable insight on the Longyearbyen community and the on-going energy conversion process.

Furthermore, I extend my thanks to Øystein Ulleberg, Principal Scientist at the Norwegian Institute for Energy Technology (IFE), who found time in his schedule to meet with me during the start-up of this thesis. His extensive knowledge of hydrogen and stand-alone power systems were valuable in the early stages of this project.

I would like to thank Bjørn Thorud of Multiconsult and Thomas Tronstad of HYON for taking the time and sharing their views on Longyearbyen's future energy supply in the preliminary phases of this thesis.

Lastly, I would like to thank my girlfriend, Nina, whom I have been lucky to share a home office with over the last couple of months. Nina has motivated me throughout a challenging process, believing in me all the way.

Thank you all!

Abstract

As of today, electricity and district heating in Longyearbyen are exclusively based on fossil fuels. It serves as a paradox, that the Norwegian settlement experiencing the impact of climate change the most, has the largest carbon footprint per capita. The coal-fired power plant of Longyear Energiverk provides a large share of the energy produced for Longyearbyen, causing 65000 tonnes worth of CO_2-emissions every year. A state analysis performed by OEC Consulting, concludes that the life span of the power plant extends to 2038. With the decommissioning of the power plant coming up, it calls for the opportunity of converting the energy supply with the largest carbon footprint in Norway to being based on renewable energy.
This thesis came to be when I was put in contact with Advisor of Energy Conversion at Longyearbyen Community Council, Rasmus Bøckman, through co-supervisor Petter H. Heyerdahl. Bøckman filled me in with the problem in hand, presented a concept system based on renewables and proposed that I could look into how various technologies for electrolyzers and fuel cells would affect the system and its interaction with the district heating.
The energy system presented by Longyearbyen Community Council should be referred to as a concept under development, where local renewable energy was intended to cover large variations in energy demand throughout the year. The system was set to use hydrogen as seasonal storage for electric energy produced by solar PV and wind power, by producing hydrogen in periods with excess power during the summertime. A modelling study of Longyearbyen's transition to a renewable energy system, conducted by Ringkjøb et al., was used to determine the feasibility of the system presented by Longyearbyen Community Council. The modelling study concluded that a stand-alone energy system based of renewables entailed a cost four times higher than a scenario with the combination of local renewable energy production and imported hydrogen from the mainland, and about eight times higher than a scenarios allowing the import of fossil fuels.
On this basis, the system proposed by Longyearbyen Community Council was rejected, and in favor of a scenario combining the production of local renewable energy and hydrogen imported from the mainland. A review of large-scale hydrogen storage technologies, by Andersson et al., made the basis for determining the most suitable form of storing hydrogen for the Longyearbyen application. Ammonia proved to be the preferred method for storing hydrogen, a fuel cell system developed by Karl Kordesch was adapted for the production of electricity and heat. Then the objective of the thesis became to calculate the energy utilization of the fuel cell system when using appropriate technologies, and determine how various operational temperatures for the district heating influence the efficiency of the system.
Three operational temperatures were selected for the district heating, 60°C, 80°C and 120°C, and the fuel cell system's energy conversion was calculated in Excel. The total efficiency of the system, from the chemical energy of the hydrogen bond in ammonia, to heat and electrical energy is calculated to be 59,1%, 54,4% and 42,2% for the respective

operational temperatures.
The thesis concludes with energy imported in the form hydrogen stored in ammonia is feasible with the technology of today, and can provide Longyearbyen with an entirely renewable energy supply. The selected fuel cell system is considered a system in development, with small changes in design able to provide considerable improvements in efficiency. It is emphasized that other technologies, such as gas turbines, compression engines and direct ammonia fuel cells, are currently being researched and developed extensively and may prove to give systems of higher efficiencies than the one presented in this thesis.

Sammendrag

Per dags dato er elektrisitet- og fjernvarmeproduksjon i Longyearbyen utelukkende driftet på fossile kilder. Det er et paradoks at den bosettingen i Norge som føler klimaendringene tettest på kroppen, har det største klimaavtrykket pr. Innbygger. Hovedvekten av energiproduksjon til Longyearbyen stammer fra kullkraftverket i Longyear Energiverk, som alene produserer 65000 tonn CO2 årlig. En tilstandsanalyse utført av OEC Consulting, konkluderer med at kullkraftverket har estimert levetid til 2038. Denne situasjonen gir muligheten for at den energiforsyningen som i dag har Norges største kilimaavtrykk, kan konverteres til å være basert på fornybar energi.
Denne oppgaven ble til ved at jeg, gjennom bi-veileder Petter H. Heyerdahl, kom i kontakt med Rasmus Bøckman, som er rådgiver for energiomstilling ved Longyearbyen lokalstyre. Bøckmann forklarte problemstillingen, presenterte en konseptskisse for et fornybart energisystem, og ønsket at jeg skulle se nærmere på hvordan ulike elektrolysør- og brenselscelleteknologier vil påvirke systemet og samspillet med fjernvarmeanlegget.
Energisystemet som ble foreslått av Longyearbyen lokalstyre betegnes som en konseptskisse, hvor et energisystem basert på lokal fornybar energi var tiltenkt å dekke store variasjoner i energibehov gjennom året. Systemet skulle benytte hydrogen for sesonglagring av elektrisk energi fra fotoceller og vindmøller, ved å produsere hydrogen i perioder med effektoverskudd i sommerhalvåret. En modelleringsstudie for Longyearbyens overgang til et fornybart energisystem, utført av Ringkjøb med flere, ble benyttet i oppgaven til å bedømme om systemet presentert av Longyearbyen lokalstyre var gjennomførbart. Modelleringsstudiet konkluderte med at kostnaden ved et stand-alone fornybar energisystem var fire ganger høyere enn ved et scenario med kombinasjon av lokal fornybar energiproduksjon og import av hydrogen fra fastlandet, og rundt åtte ganger høyere enn et scenario som tillot import av fossile brensler.
Systemet foreslått av Longyearbyen lokalstyre ble dermed forkastet i oppgaven, til fordel for et scenario som kombinerer produksjon av lokal fornybar energi med hydrogen importert fra fastlandet. En gjennomgang av storskala hydrogenlagringsteknologi, av Andersson med flere, ble lagt til grunn for å bestemme den mest hensiktsmessige lagringsformen for hydrogen i Longyearbyen. På dette grunnlaget ble ammoniakk valgt som lagringsform, og et brenselscellesystem utviklet av Karl Kordesch ble tilpasset for produksjon av elektrisitet og varme. Målet for oppgaven ble dermed å beregne hvordan ulike driftstemperaturer for fjernvarmesystemet vil påvirke energiutnyttelsen til brenselcellesystemet ved bruk av egnede teknologier.
Tre ulike driftstemperaturer for fjernvarmesystemet ble valgt 60°C, 80°C og 120°C, og brenselcellesystemets energikonvertering ble beregnet i Excel. Systemets totaleffektivitet, fra kjemisk energi i hydrogenet som er bundet i ammoniakk til varme og elektrisk energi er beregnet til å være 59,1%, 54,4% og 42,2% for de respektive driftstemperaturene.
Oppgaven konkluderer med at energi importert i form av hydrogen lagret i ammoniakk er gjennomførbar med dagens teknologi, og kan gi Longyearbyen en kraftforsyning som er fullstendig fornybar. Løsningen med det valgte brenselscellesystemet anses for

å trenge videre utvikling, ettersom små designendringer kan føre til betydelige effektivitetsforbedringer. Det er viktig å understreke at andre teknologier for forbrenning av ammoniakk, som gassturbin, stempelmotor og direkte ammoniakk brenselscelle, er under rivende utvikling og kan vise seg å gi høyere effektivitet enn systemet presentert i denne oppgaven.

Contents

1 Introduction **1**
- 1.1 Regarding Longyearbyen and Svalbard . . . 1
- 1.2 Current energy supply . . . 2
  - 1.2.1 Power generating units . . . 2
  - 1.2.2 Power grid . . . 4
  - 1.2.3 District heating and distribution . . . 4
- 1.3 Current energy consumption . . . 5
  - 1.3.1 Heat consumption . . . 6
  - 1.3.2 Electricity consumption . . . 7
- 1.4 Summary . . . 7

2 Presented system **8**

3 Modeling study of Longyearbyen **10**

4 System selection **15**
- 4.1 Large-scale hydrogen storage technologies . . . 15
  - 4.1.1 Liquid hydrogen . . . 17
  - 4.1.2 Ammonia . . . 18
  - 4.1.3 Summary . . . 18
- 4.2 System for power generation . . . 19
  - 4.2.1 Fuel cell system . . . 19
  - 4.2.2 Combustion engines . . . 20
  - 4.2.3 Gas turbine . . . 20
  - 4.2.4 Summary . . . 20

5 System description **21**

6 System components **24**
- 6.1 Ammonia storage . . . 24
- 6.2 Heat exchanger for H_2-mixture and NH_3 . . . 24
- 6.3 Ammonia cracker . . . 26
- 6.4 Alkaline fuel cell . . . 27
  - 6.4.1 Electrodes . . . 30
  - 6.4.2 Electrolyte . . . 31
  - 6.4.3 Electrolyte system design . . . 31
  - 6.4.4 Stack design . . . 32
  - 6.4.5 Operating temperature . . . 33
  - 6.4.6 Operating pressure . . . 35
  - 6.4.7 Fuel utilization . . . 35
- 6.5 Condensing heat exchanger for H_2O and air . . . 35

6.6 Heat exchanger for flue gas and combustion reactants . . . 36
6.7 CO_2-scrubber . . . 37
6.8 Electrolyte system . . . 39
6.9 Power conditioner . . . 40
6.10 Pumps, compressors and fans . . . 41

7 Mass balances **45**
7.1 Ammonia storage . . . 45
7.2 Vaporizing heat exchanger . . . 46
7.3 Ammonia cracker . . . 46
7.3.1 Endothermic reaction . . . 47
7.3.2 Combustion reaction . . . 47
7.3.3 Summary . . . 50
7.4 Alkaline fuel cell . . . 50
7.5 Condensing heat exchanger for H_2O and air . . . 51
7.6 Heat exchanger for exhaust gas and combustion reactants . . . 52
7.7 CO_2-scrubber . . . 53
7.8 Electrolyte system . . . 57

8 Energy balances **59**
8.1 Ammonia storage . . . 59
8.2 Heat exchanger for vaporization of NH_3 . . . 59
8.3 Ammonia cracker . . . 61
8.3.1 Temperature rise . . . 61
8.3.2 Endothermic reaction . . . 61
8.3.3 Combustion reaction . . . 62
8.3.4 Summary . . . 63
8.4 Alkaline fuel cell . . . 64
8.4.1 Incoming H_2 . . . 64
8.4.2 Unreacted H_2 . . . 65
8.4.3 Electricity . . . 65
8.4.4 Latent heat in H_2O . . . 72
8.4.5 Heat in electrolyte . . . 72
8.4.6 Summary . . . 72
8.5 Condensing heat exchanger . . . 73
8.6 Heat exchanger for exhaust gas and combustion reactants . . . 74
8.7 CO_2-scrubber . . . 76
8.8 Electrolyte system . . . 77
8.9 Power conditioner . . . 80
8.10 Pumps, compressors and fans . . . 83
8.11 Total system . . . 84

9 Discussion **89**
9.1 Presented system . . . 89
9.2 Modeling study . . . 89
9.3 Large-scale storage and method for power generation . . . 90
9.4 Selected system and its technologies . . . 91
9.5 System components . . . 92

10 Conclusion **95**

1. Introduction

1.1 Regarding Longyearbyen and Svalbard

Svalbard is an archipelago extending from 74°to 81°North and 10°to 35°East. Its position compared to mainland Europe is seen in figure 1.1, and its largest settlement, Longyearbyen is marked with a red dot. The climate is arctic, and the archipelago has a very long winter with four months of polar night, and an equally long period of midnight sun. Politically, Svalbard is in a special position as it is ruled under the Svalbard Treaty, which ensure Norwegian sovereignty, but grants other countries, who have signed the treaty, to extract resources and establish settlements on the archipelago. This special position makes Svalbard subject for continuous debate of how the fishery in its territorial sea is managed.[1]

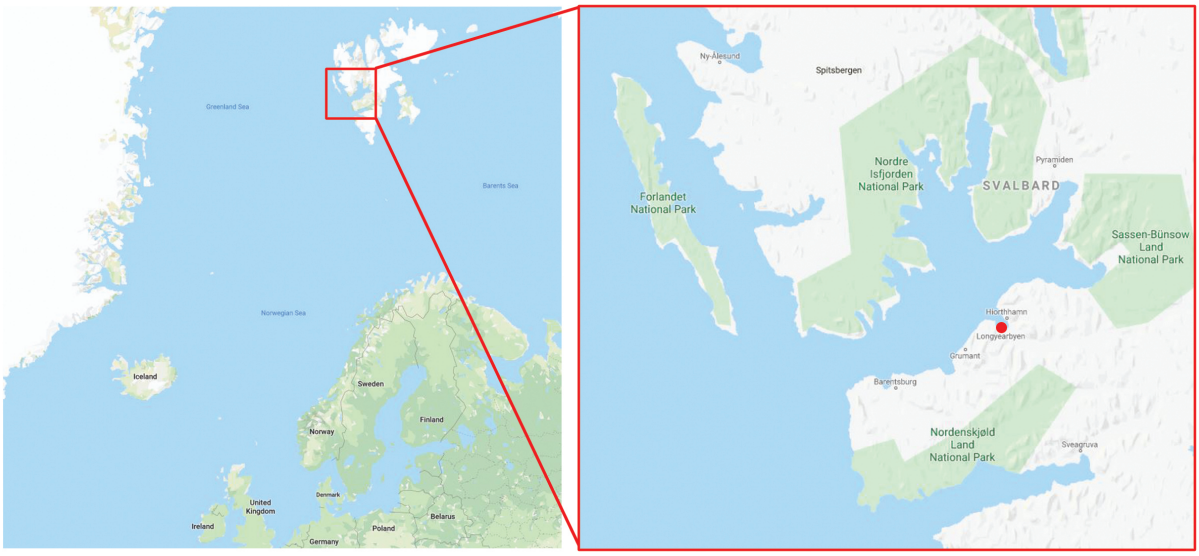

Figure 1.1: Svalbard's and mainland Europe. Longyearbyen is marked with the red dot.

During the 17th and 18th centuries, Svalbard was mainly used as a basecamp for whaling vessels, and settlements were established and abandoned frequently. In the early 1900s, the mining of the archipelago's coal resources started, leading to mining companies establishing permanent settlements, one of them being Longyearbyen. The settlement's population fluctuated in line with the business cycle of the mining activities, before stabilizing as a result of the emergence of new industries such as tourism and research. Longyearbyen has a population of roughly 2100, and in 2018, 101 full-time equivalents were registered for mining and quarrying, showing the decline of what used to be the settlement's main economy. In March 2020, Svea Nord was closed, leaving Gruve 7 as the only mine still in operation in Longyearbyen.[2][3]

The interest for Svalbard and Longyearbyen is currently bigger than ever. Its arctic location makes results of climate change very noticeable compared to other parts of the world, and has led to the establishment of The University Center in Svalbard and several research institutes. In addition to climate change, research at UNIS is linked with the satellite station SvalSat and the radar system EISCAT Svalbard Radar (EAR). SvalSat is used to track, control and communicate with satellites in polar orbit, while EAR is used for researching how the activity of aurora borealis and solar wind affects the atmosphere.[4][5]

1.2 Current energy supply

Over the next subsections, the current energy system of Longyearbyen is presented with its power generating units and energy consumption.

1.2.1 Power generating units

Longyear Energiverk

Since 1982, a coal-fired power plant, Longyear Energiverk, has supplied Longyearbyen with heat and electricity. Longyear Energiverk is seen in figure 1.2 On average, the plant has an annual consumption of 25 000 tonnes of coal, resulting in 65,000 tonnes of carbon dioxide emissions. A scrubbing system used for cleaning the flue gas of nitrogen oxides, sulfur dioxide and soot particles was implemented in 2015.

Figure 1.2: Longyear Energiverk[6]

Longyear Energiverk consists of two coal-fired boilers and two steam turbines as seen in

figure 1.3. The steam turbines have a theoretical effect of 5,5 MW each. From turbine 1, steam is extracted and is used to produce district heating with a theoretical effect of 22 MW. In total, the power plant has a theoretical effect of 11 MW electricity and 22 MW district heating. Due to the gas scrubber having limited capacity, both boilers can not be operated simultaneously, resulting in a maximum electrical power production of 7,5 MW. At maximum electrical power production, Longyearbyen Community Council estimates the district heating production to be limited to 16 MW. In practice, one boiler supplies the total heat and electric power demand, while the other boiler provides back-up power. A 5 MW diesel boiler is installed to provide back-up steam production for the district heating. A state analysis by OEC Consulting in 2013, concluded that the life span of the power plant extends to 2038.[7]

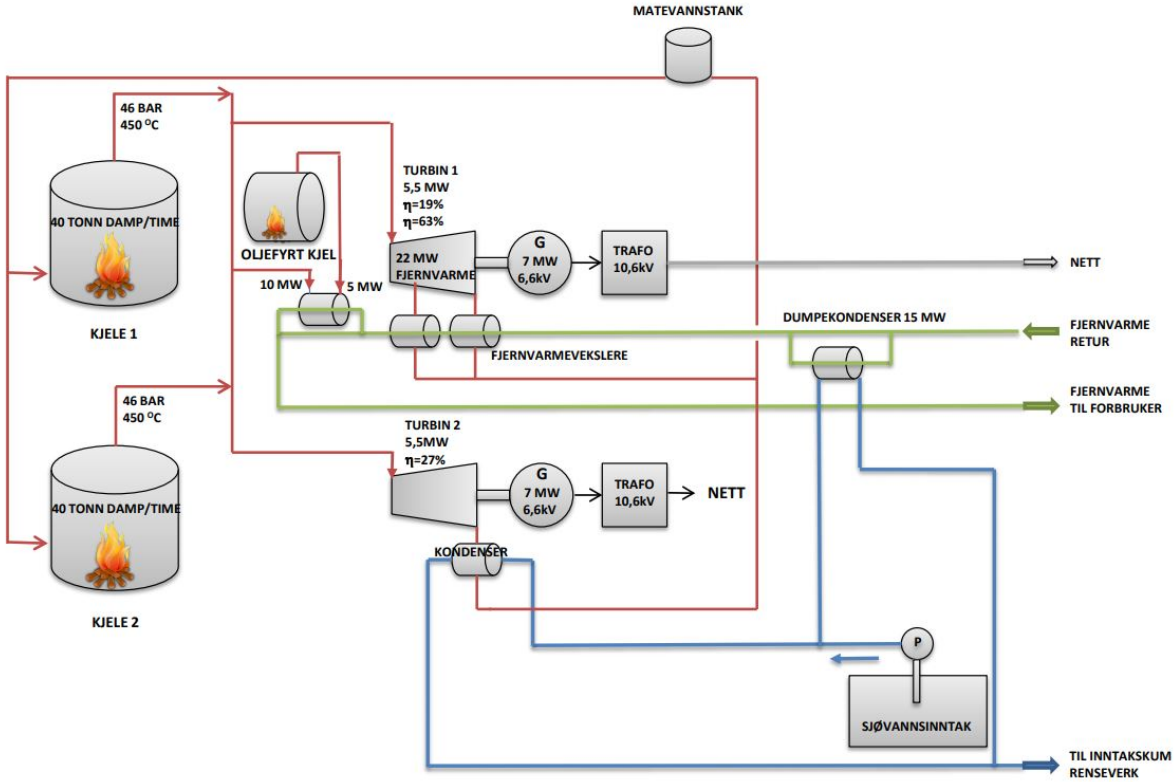

Figure 1.3: Process schematic for Longyear Energiverk[7]

Reserve power plant

If the energy supply from the coal-fired power plant proves to be insufficient, a back-up power plant is installed near the University. The plant consists of three diesel engines of 1,5 MW each. There are plans for constructing a new modular reserve power plant with a combined effect of 6 MW, split over three diesel engines.[8]

Emergency generators

There are multiple emergency generators associated with various consumers, which are are not part of the ordinary power supply. In total the emergency generators have an installed electric effect of about 4,4 MW.

Decentralized diesel boilers

To supply peak load and serve as back-up power for the district heating, six diesel boilers are installed in what is referred to as Boiler houses throughout Longyearbyen. The installed Boiler house effect ranges from 1,2 to 4,5 MW and totaling at 15,7 MW.

Summary power generating units

Table 1.1 presents all power generating units part of the current energy system in Longyearbyen.

Unit	Energy source	Electricity generated	Heat generated
Coal-fired power plant	Coal	7,5 MW	14 MW
Back-up diesel boiler	Diesel	-	5 MW
Back-up power plant	Diesel	4,5 MW	-
Emergency generators	Diesel	4,4 MW	-
Boiler houses	Diesel	-	15,7 MW
Total capacity	-	16,4 MW	34,7 MW

Table 1.1: Total installed electric power and heat in the Longyearbyen energy system.[9]

1.2.2 Power grid

The electrical distribution system consists of a total of 45 km of lines, where 16 km is overhead lines and 29 km is grounded cables. The high-voltage grid operates at two set voltages, 11 or 22 kV. While low-voltage section spans over 1 kV, 400 V TN and 230 V IT. Parts of the grid have come of age, and plans are made for re-investments in the overhead lines.[10]

1.2.3 District heating and distribution

The district heating of Longyearbyen is adapted to heat from combustion processes, making it less suited for low-temperature sources, like geothermic heat and solar heat. The main applications for the district heating are space heating, ventilation air heating and heating of tap water inside buildings. There are significant heat losses in both the pipeline and boiler houses. The losses are partly due to system design, where district heating contributes to preventing water and sewer pipes from freezing. The annual heat loss for a district heating facility situated on mainland of Norway is typically 10%. Power meters are not installed on the consumer side of the Longyearbyen district heating system, so currently there is no data available for the heat losses. But calculations show that the district heat consume in Longyearbyen is 40% higher per square meter than on the mainland.[11][12]
The heating is distributed through a network which consists of a primary- and a secondary network. The construction of the distribution network started in 1950, with the secondary network being built as local networks distributing heat from the separate Boiler houses. With the construction of the coal-fired power plant in 1982, the establishment of a primary network began. This led to the primary network tying together the various secondary networks. At heavy loads, the primary network delivers outgoing temperatures

up to 120°C while the secondary network delivers temperatures at 90°C. The heat from the network is then heat exchanged to installations in each housing, requiring temperatures of 70°C.
A recent state analysis concludes that the remaining lifetime of the primary network is about 15-20 years. The state of the secondary network varies greatly, with expansions and re-investments are done sporadically over 70 years.
There are concerns regarding the systems ability to supply future capacity demands. At the same time, there is a considerable amount of energy that could be utilized through optimizing the system for heat loss. THEMA and Multiconsult concludes with this being the ideal time for making investments which prepares the system for utilization of low-temperature sources of energy.[13]

1.3 Current energy consumption

In 2018 Longyearbyen consumed 40 GWh of electricity and 70 GWh of heat from the district heating, peaking at 12 MW of electricity and 15 MW of heat. The heat production is plotted through a year in figure 1.4. The heat is mainly consumed by households and municipal services, while commercial activity, like Gruve 7, EAR and SvalSat, consumes considerable parts of the electricity. Due to its design, and its built-in flue gas treatment system, the coal-fired power plant has a relatively high of electricity consumption of its own.[14]

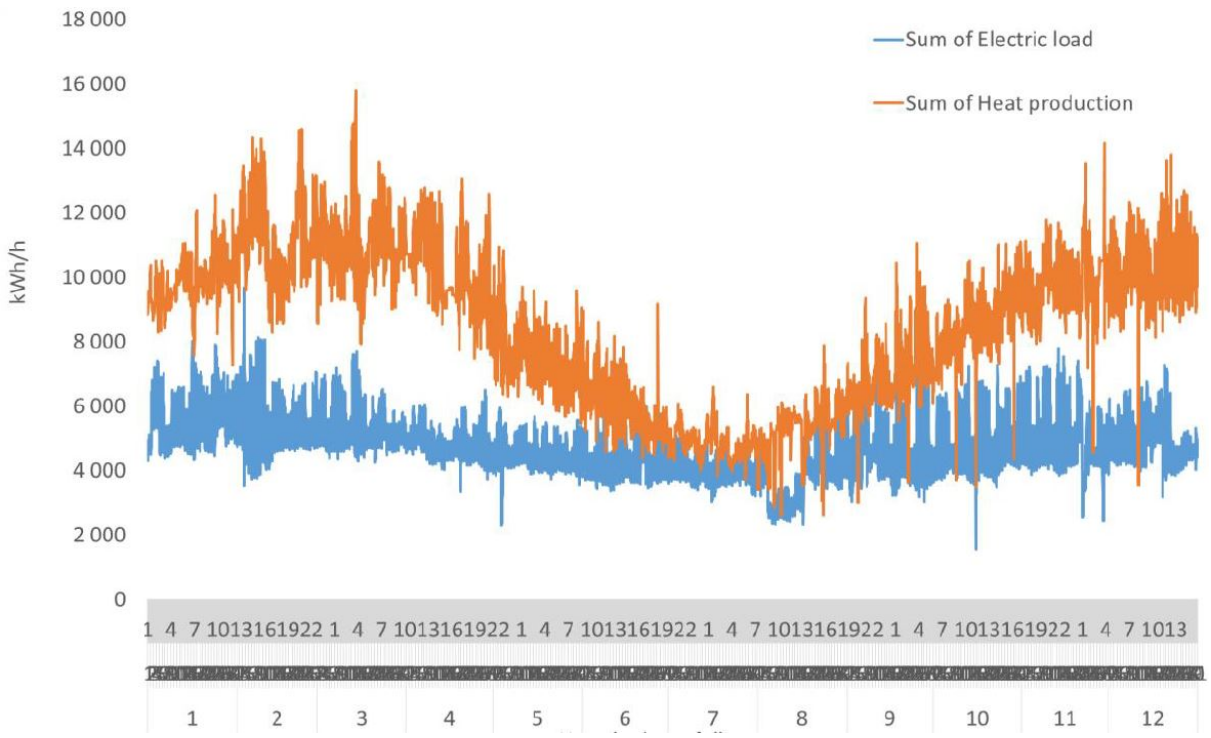

Figure 1.4: Total heat production and electric load hour-by-hour for 2018. Heat production in orange, electric load in blue.[15]

1.3.1 Heat consumption

Without power meters installed, the data given for the district heating is based on data from Longyear Energiverk, meaning heat production from the Boiler houses are not included. Heat consumption in Longyearbyen is temperature dependent, meaning that production varies throughout the year. In 2017, about 70% of the heat production was temperature-dependent, while the remaining 30% is mainly due to the heating of tap water. During winter, the heat consumption of Longyearbyen averages between 10-12 MW, while during summer averaging between 5-6 MW. Load-profiles for winter and summer days are presented in figure 1.5 and 1.6. The heat consumption is stable throughout the week, not fluctuating in weekends.[16]

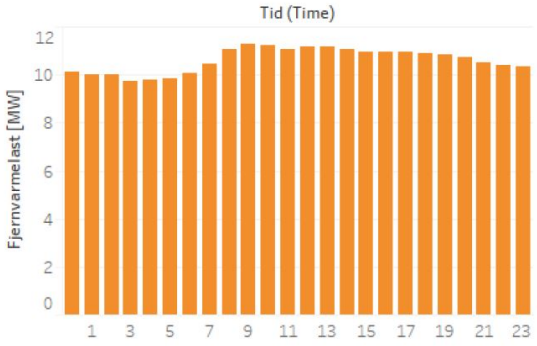

Figure 1.5: Average day profile for heat production from December to March[16]

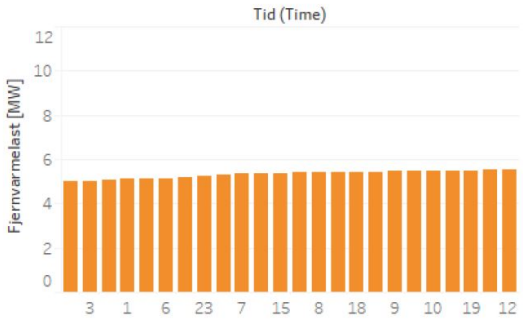

Figure 1.6: Average day profile for heat production from June to August[16]

Peak heat production at Longyear Energiverk in 2017, occurred on March 11th, and was registered to about 14 MW, while the outdoor temperature had been -20°C earlier the same morning. As the data does not include heat given from the boiler houses, the total heat consumption for Longyearbyen is higher than stated. Figure 1.7 plots the average heat production per hour on the 11th of March along with the varying outdoor temperature.

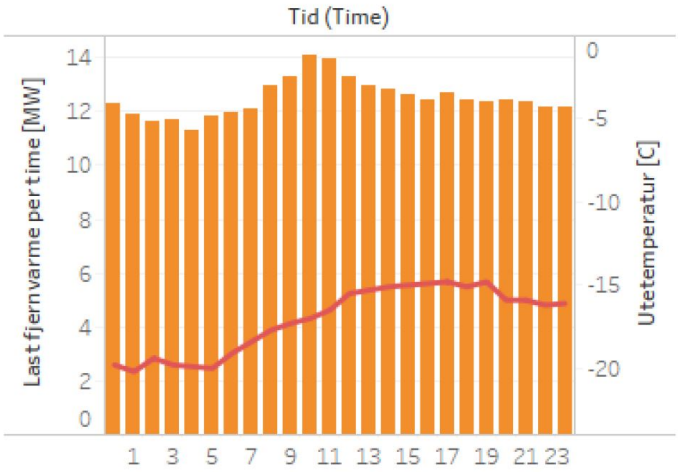

Figure 1.7: Profile of heat production and the altering outdoor temperature on March 11, the day in the year with the largest heat consumption.[16]

1.3.2 Electricity consumption

As electricity is not used for heating purposes, the electricity consumption is quite stable and less dependent on the outdoor temperature. In general, the need for electricity is lower at night and on the weekend, than during the week. Approximately 15% of the electricity consumption fluctuates due to changes in outdoor temperatures. During winter, the electric power demand is about 6 MW in the day time and 4 MW at night, while in summer averaging at 4 MW. The profiles for an average day in winter and summer are presented in the figure 1.8 1.9.

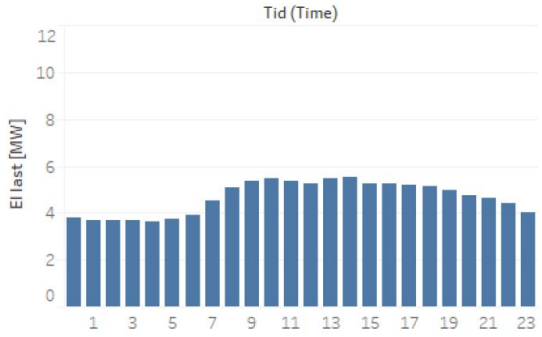

Figure 1.8: Average day profile for electricity production from December to March[14]

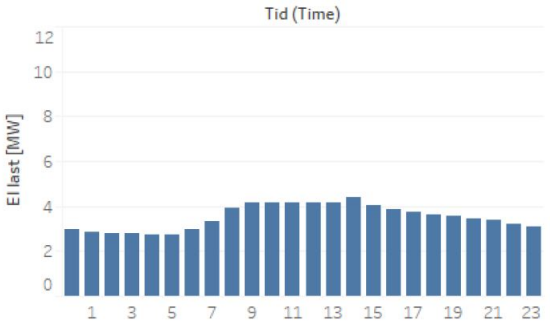

Figure 1.9: Average day profile for electricity production from June to August[14]

1.4 Summary

From the previous sections, it is evident that the energy system in Longyearbyen is coming of age, and is the result of a series of system additions over 70 years. OEC Consulting has concluded that the coal-fired power plant's lifespan extends to 2038. The district heating operates at high temperatures, with significant losses throughout the system. There are large seasonal variations in heat demand due to the fluctuating outdoor temperature, while electric power demand remains quite stable throughout the year.
In their report for a future energy supply for Svalbard, THEMA and Multiconsult conclude with this being the ideal time for making investments that enables the utilization of low-temperature heat sources for heat distribution.

2. Presented system

Starting this thesis, a concept sketch for a future stand-alone energy system was presented by the Advisor of Energy Conversion at Longyearbyen Community Council. A representation of the sketch is seen in figure 2.1.

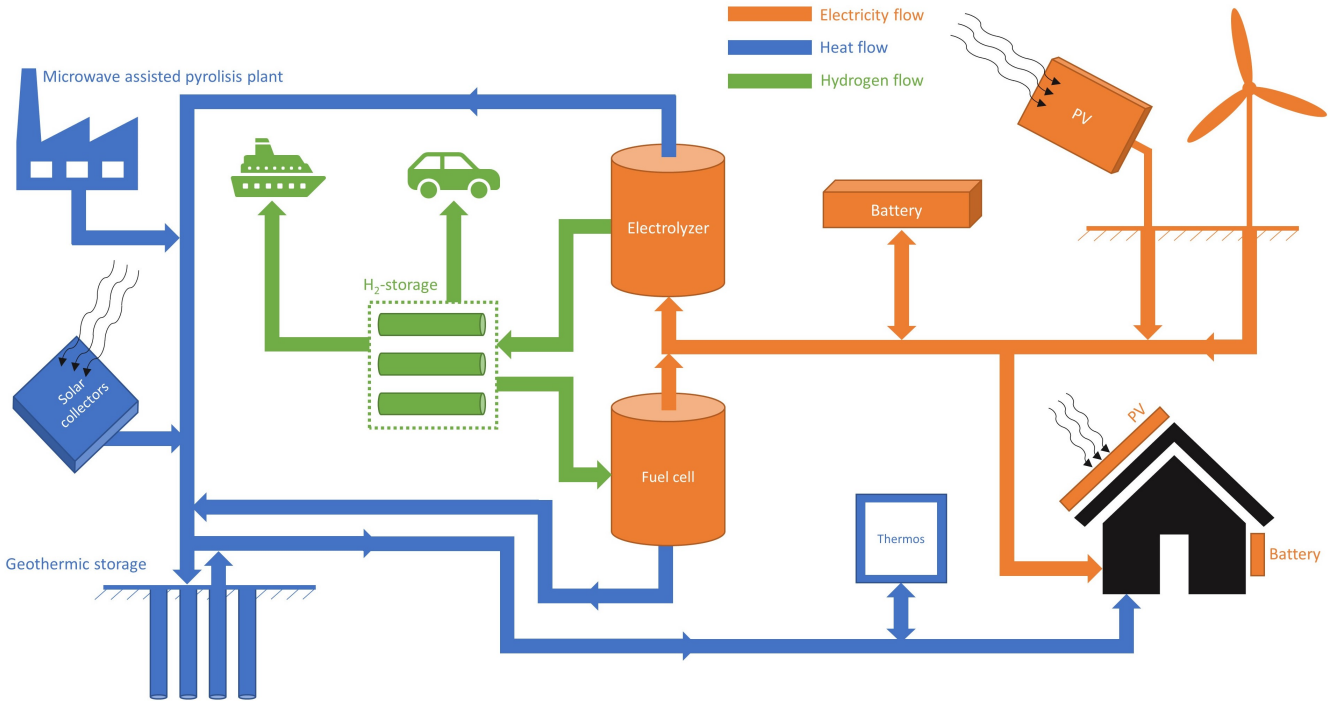

Figure 2.1: Interpretation of the concept system presented at the start of the thesis.

The concept is based on electric power generation through large-scale solar PV and wind power, which could be stored for shorter periods in a battery, or through seasons as hydrogen. An electrolyzer generates large amounts of hydrogen during the summer, which is stored and utilized for electricity and heat generation in a fuel cell throughout the winter, when renewable power access is low. Surplus hydrogen could be used to fuel local transport needs such as snowmobiles and cars, even providing hydrogen for docking ships. Roof installed solar PV with battery storage is assumed to be a standard for buildings throughout Longyearbyen.
Heat from a Microwave Assisted Pyrolysis (MAP) is intended to serve as baseload for the settlement. MAP is a technology enabling the production of 3rd generation biofuels from the rapid heating of plastic waste under oxygen-absent conditions. The concept sketch relies on a scenario where plastic or rubber waste, is imported from mainland Norway. The MAP process adds value to the waste imports, as its products of carbon, oil, tar and organic acids can be exported or consumed locally.[17]
A thermal solar farm assists with seasonal fluctuations in heat demand. During summer,

solar radiation is converted to heat in the water passing through the solar collectors, the heat is transferred to the geothermal storage, consisting of bedrock, through conduction. In the winter, the bedrock heats the water passing through the storage, and the water's temperature is lifted to the district heating's operating temperature through the use of heat pumps.
Small-scale thermal energy storage are placed near critical heat loads throughout Longyearbyen, and are used for leveling short spanned fluctuations of heat demand in the district heating grid.

The thesis objective presented by Longyearbyen Community Council, was to perform a theoretical evaluation of the heat generated by various electrolyzer and fuel cell configurations and technologies, and how the generated heat will interact with the district heating system, when operating under low- and high-temperature conditions. As no guidelines were set for the operating temperature of the district heating at the time of system presentation, scenarios of 60°C, 80°C and 120°C were selected. The system boundaries were then limited as seen in figure 2.2.

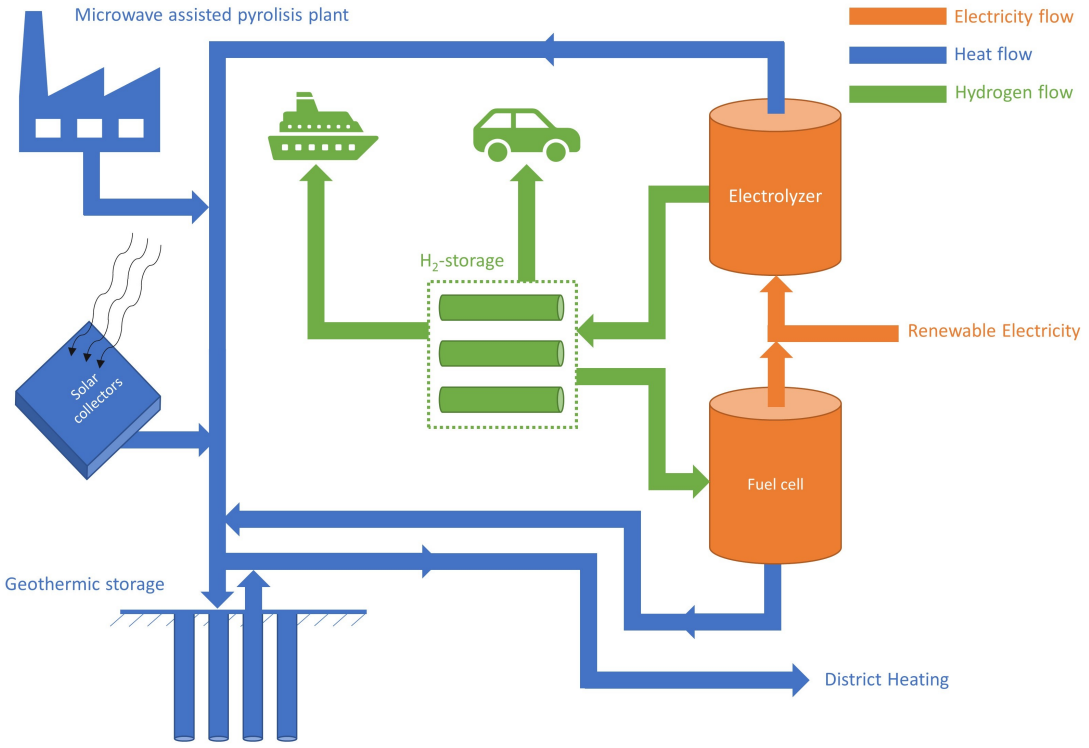

Figure 2.2: Interpretation of the system presented at the start of the thesis.

Since no thorough calculations were made prior to the presentation of the concept energy system, its feasibility is highly questionable. Through discussion with senior-scientist at IFE, Ø. Ulleberg, it was determined that a thesis regarding an energy system which proves to be unfeasible, is of little to no value.
The presented system is far too complex for its feasibility to be determined based on the scarce data made available for this thesis. Instead, a modeling study by Ringkjøb et al. provides a basis for determining the concept energy system's feasibility and is presented in the upcoming chapter.

3. Modeling study of Longyearbyen

Since the desired energy system is based on variable renewables, an accurate representation of their short-term variability in energy output is crucial for selecting the most beneficial system. In 2019, Ringkjøb et al. conducted a techno-economic energy modeling study for Longyearbyen, utilizing the TIMES framework to develop a stochastic model that was applied for the Arctic settlement. The TIMES energy modeling system is an evolution of a system named MARKAL, and both are developed by the Energy Technology Systems Analysis Programme (ETSAP) of the International Energy Agency (IEA). TIMES is a bottom-up energy model generator using linear programming, combining a technical engineering and an economic approach, to produce a least-cost energy system. The system produced is optimized in accordance to a number of constraints set by the user, and the system is simulated several decades into the future. As stated by ETSAP, TIMES is intended for exploring possible energy futures based on contrasting scenarios.[18]

TIMES-Longyearbyen

With a basis in the TIMES modeling framework, Ringkjøb et al. developed the stochastic long-term energy model TIMES-Longyearbyen. With the model being stochastic, means that it is controlled by probability laws. The model base-year is 2015, with and the simulation runs until 2050. Each year is represented by four seasons, with one weekday and one day of weekend for each season, each day is split into 24 hours, resulting in one year being represented by 192 time-slices, as seen in figure 3.1.[19][20]

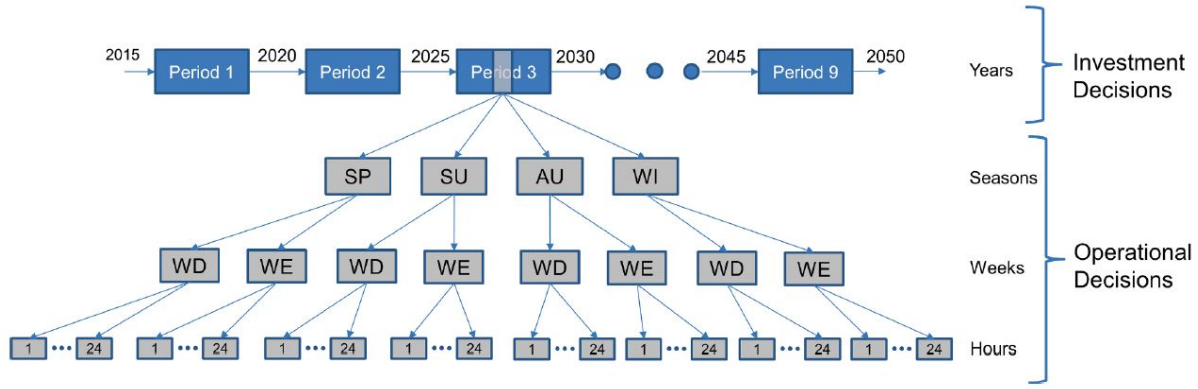

Figure 3.1: Representation of a year through 192 time-slices in TIMES-Longyearbyen[19]

Each time-slice is then assigned with a demand for heat and electricity from data sets retrieved from Longyear Energiverk, along with hourly wind and solar electricity generation estimates based on data from possible PV and wind power locations in and around Longyearbyen. The heat and electricity demands must then be covered by the energy

resources, through using a set of technologies made available for the model.
The technologies made available for TIMES-Longyearbyen are: solar photovoltaics, solar thermal, onshore- and offshore wind, hydrogen electrolysers, hydrogen storage, hydrogen fuel cells, lithium-ion batteries, geothermal and seawater-based heat pumps, electric boilers, underground thermal energy storage, diesel generators, gas turbines and gas cogeneration plants. Hydropower and biomass were left out of the model, due to lacking potential in Longyearbyen.
With each time slice containing heat and electricity demand, the projection of Longyearbyen's future energy demand becomes utterly important for the TIMES-model. The population of Longyearbyen is assumed to be stable at the 2015 level throughout the simulation period. Compared with the current demand, Ringkjøb et al. predict a decreased demand for electricity and heat, by 13 GWh and 34 GWh respectively in 2050, as seen in figure 3.2. Compared with the current demand, Ringkjøb et al. predict a decreasing energy demand, as seen in figure 3.2. According to the projections, energy consumption has decreased by 13 GWh electricity and 34 GWh heat in 2050. The decrease is mainly due to the renewal of Longyearbyen's large share of old building stock, decommissioning of the coal-fired power plant and mining activities shutting down. Ringkjøb et al. emphasize that their energy demand projection only calls for one of several possible scenarios, as the future of Longyearbyen depends highly on political decisions.

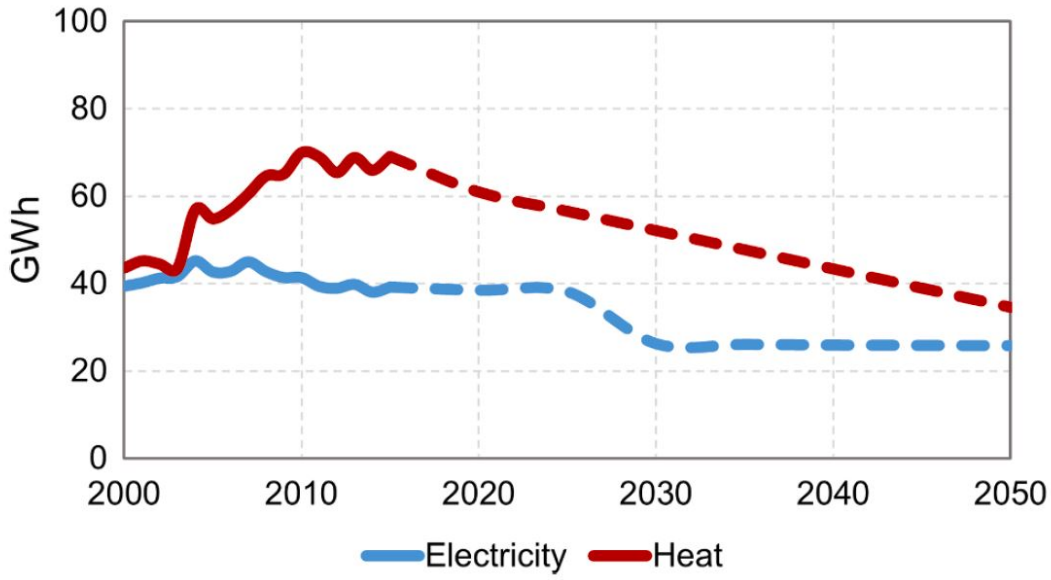

Figure 3.2: Projections of future energy demand[19]

To reflect the weather being highly irregular and hard to predict, seven stochastic parameters are used to describe the solar and wind electric power generation and the demand for energy and heat. Ringkjøb et al. then applied a two-stage model based on the stochastic parameters, illustrated through figure 3.3.
The first stage involves making investment decisions for the whole simulation period, utilizing the given data sets for the process. This process mimics real-life decision making, leading to feasible investments for stage two of the model. In stage two the operational simulation starts, and operational decisions are made every fifth year for sixty different scenarios each generated from a unique set of stochastic parameters. The investment decisions from stage one is then adjusted according to the operational decisions made in stage two, providing sixty different energy systems based on the deviation of 10 000 data

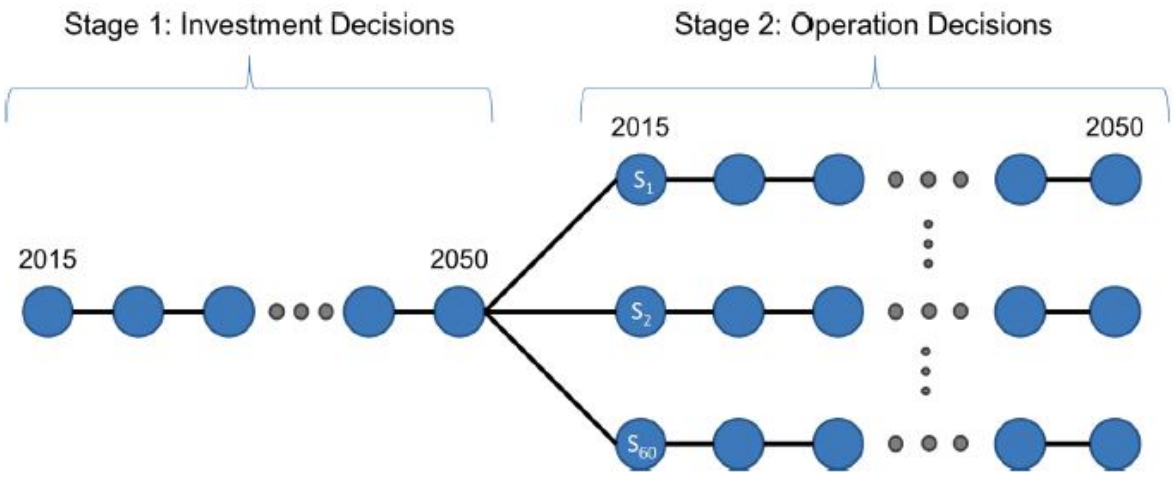

Figure 3.3: Illustration of the two-stage scenario tree, totaling sixty operational scenarios.[19]

sets of equal probability.
The simulation process is then repeated for four model cases, each having different constraints. The model cases are summarized in table 3.1.

Model case	**Method**	**Description**
DET	Deterministic	Deterministic case regarded as unrealistic by Ringkjøb et al.. Included to compare modelling techniques.
ISO	Stochastic	Isolated energy system, all energy is generated by local resources.
HYD	Stochastic	Renewable energy system, allowing for import of renewable hydrogen from mainland Norway.
FOS	Stochastic	Allowing imports of fossil fuels to the energy system.

Table 3.1: Overview of model cases investigated in the study and their constraints.[19]

Results

For all four modeling cases, TIMES-Longyearbyen decides to keep the coal-fired power plant until decommissioning in 2030, adding minor measures for energy efficiency and on-shore wind capacity to the energy mix. Electrification of heating is also seen in all four cases, with electric boilers, heat pumps and heat from hydrogen fuel cells being main sources of heating in the ISO and HYD model cases.
As model case FOS does not fit the description of the system desired by Longyearbyen Community Council, it is cut from further analysis, along with the deterministic case DET as it is considered unrealistic by Ringkjøb et al., and therefore serves no value for this thesis. Further, the outcome of the ISO and HYD model cases are presented.

ISO - Isolated energy system
In the ISO model case, Longyearbyen is a completely isolated energy system, powered by local renewable energy sources from 2030 and onward. The model invests in large capacities of solar and wind, batteries, and a full hydrogen production and storage system.

To cover energy demand in no-wind periods during polar nights, hydrogen is produced, and stored seasonally, during the summertime when large amounts of excess electricity is produced by the solar PV. The production of hydrogen calls for the installation of 119 MW solar PV and 126 MW on-shore wind to provide sufficient reliability in energy supply, which is 50 times larger than the settlement's peak hourly electricity demand. The seasonal difference in system operation for the HYD model case is illustrated in figure 3.4.

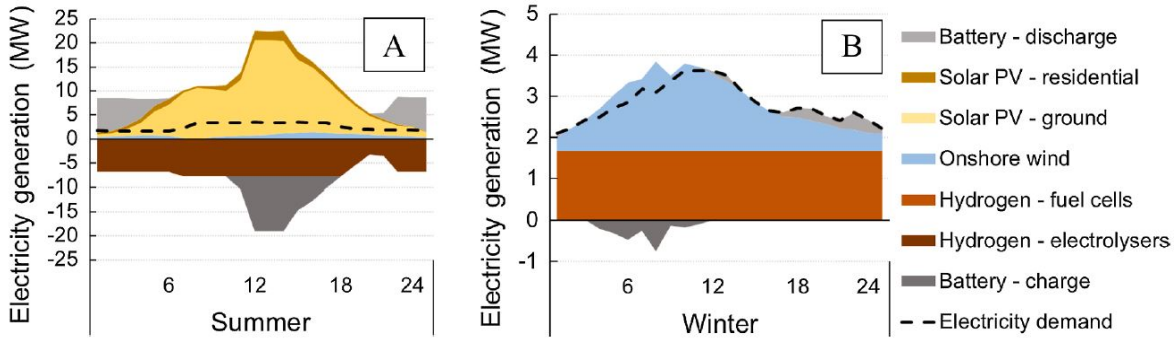

Figure 3.4: Example of system operation in 2050. A is on a summer day, and B is on a winter day, note the difference in scales or electricity generation in the two examples.[19]

HYD - Imported hydrogen

In the HYD model case, Longyearbyen relies on local renewable energy, with the addition of renewable hydrogen shipped from mainland Norway. Entering 2050, the model invests in 14,5 MW of solar PV and 20,5 MW of on-shore wind, with a hydrogen import, averaged across all scenarios, of 89 GWh in 2030 and 60 GWh in 2050. A hydrogen price of 35 NOK/kg is used in the study, which is assumed to be sufficient to produce the hydrogen in mainland Norway and transport it to Longyearbyen.

Result summary

The installed capacity for all model cases is presented in figure 3.5, with the bullets being the total installed capacity, and colored bars giving the share the specific form of technology provides to the system.

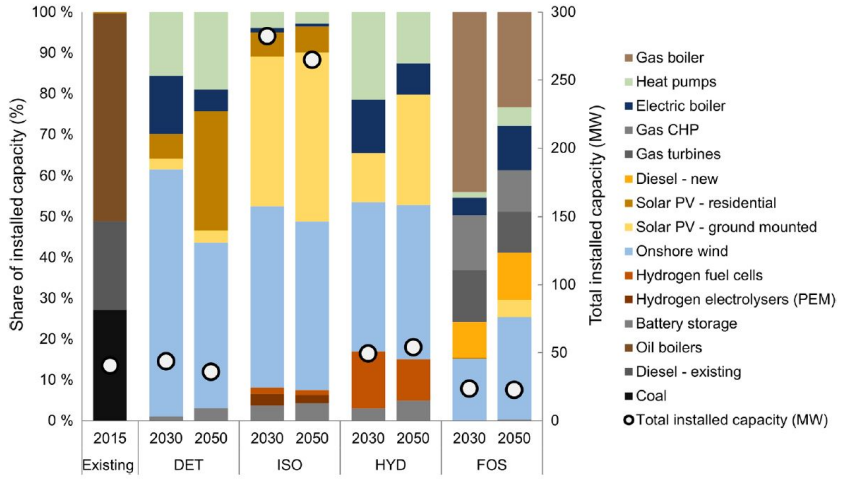

Figure 3.5: The total installed capacity of all model cases, and the share of each technology provides to the total.[19]

As seen in the figure, the ISO model case has by far the largest installed energy capacity, peaking at more than 275 MW in 2030. The HYD model case peaks at right above 50 MW in 2050, with the addition of 60 GWh of hydrogen in the energy mix.
The sensitivity of the annual system cost of the various model cases is presented in figure 3.6, along with the sensitivity of the cost for the HYD model case relative to the price of hydrogen.

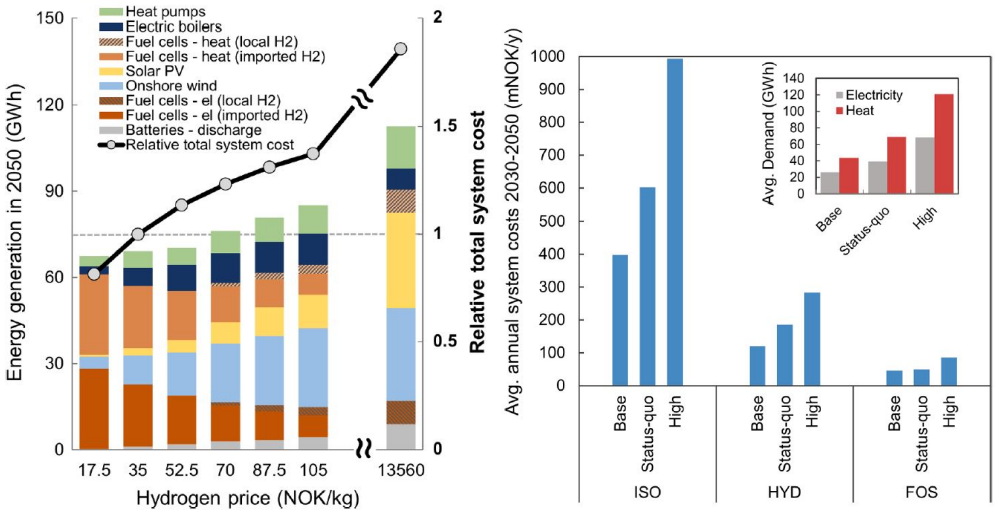

(a) (b)

Figure 3.6: (a) illustrates the HYD model case cost sensitivity due to hydrogen price, and (b) illustrates sensitivity of annual system cost for all cases based on alternative projections of energy demand.[19]

The local production of hydrogen is found to be economically viable if the hydrogen price passes 70 NOK/kg. At 70 NOK/kg, it would still be beneficial to buy large shares from mainland Norway, and for a large scale hydrogen production to be economically viable for power generation in Longyearbyen, the price should surpass 100 NOK/kg.
For an isolated energy system based on renewables, the annual system cost is estimated to be 400 mNOK/year at the projected energy demand, averaging the cost of energy to be 5,73 NOK/kWh from 2030 to 2050. It is worth noting that in a high energy demand climate, as the sensitivity plot in figure 3.6(b) shows, the annual system cost surpass 1000 mNOK/year. For the HYD model case, the annual system cost is estimated to be 125 mNOK/year, averaging the cost of energy to 1,73 NOK/kWh throughout the simulation period. The sensitivity analysis shows that in a case of a high energy demand, the system cost would be just under 300 mNOK/year.

Conclusion

Ringkjøb et al. conclude that transitioning to an energy system based strictly on renewable energy resources is feasible for the Longyearbyen system. Recommending that a future energy system is mainly based on renewable power generation, but emphasize that energy storage, import of hydrogen and sufficient back-up capacity must be considered for the system to apply its demands.
Due to the cost estimations linked with an energy system based solely on local renewable resources, the hydrogen import scenario is used as a basis for the further development of the energy system in this thesis.

4. System selection

Based on the modeling study conducted by Ringkjøb et al., it was decided to move forward with the HYD model case. A system that is based on local renewable resources, but imports energy in the form of hydrogen from mainland Norway.

4.1 Large-scale hydrogen storage technologies

Importing hydrogen for power generation in Longyearbyen calls for the hydrogen being shipped in large volumes, which needs to be stored safely until the energy is demanded by the settlement. Currently, there is no preferred hydrogen storage technology, and due to the vast range of technologies available, it is useful to organize them into categories. A categorization system proposed by Andersson et al. is illustrated in figure 4.1.

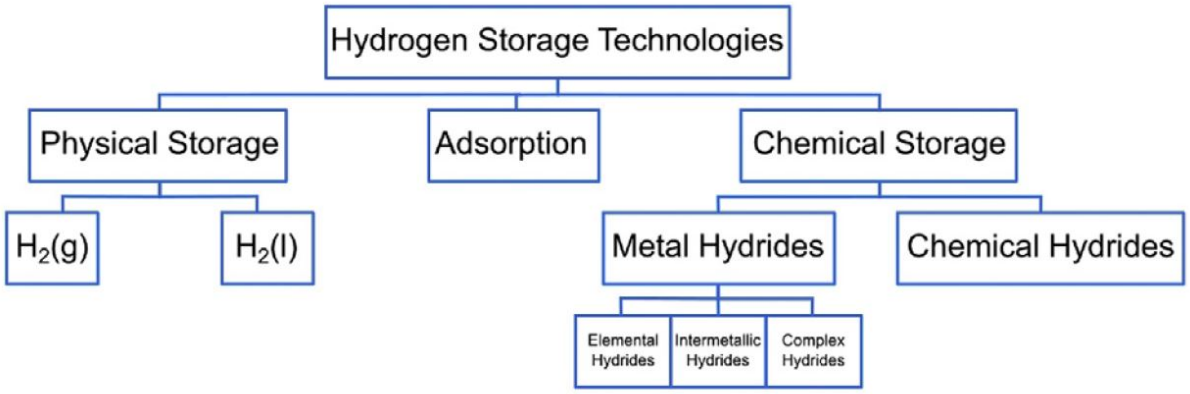

Figure 4.1: Categorization of hydrogen storage technologies by Andersson et al.[21]

Andersson et al.'s categorization system consists of three main categories. The first category is physical storage, where hydrogen is stored in pure form without bonding to other materials. Physical storage is split into two sub-categories, compressed hydrogen and liquid hydrogen. The second category is adsorption, where molecular hydrogen adsorbed onto or into other materials by weak Van der Waals bonds. The last category is chemical storage, where atomic hydrogen is stored through chemical bonds. Chemical storage is split into two sub-categories, metal hydrides and chemical hydrides.[21]
When selecting hydrogen storage technology for large-scale storage applications, an important feature is hydrogen storage density. In figure 4.2, the volumetric and gravimetric density of common large-scale hydrogen storage technologies are presented. Volumetric density means mass per volume unit and gravimetric density meaning the fraction hydrogen constitutes of the storage's complete mass.
With basis in storage density, cost of storage and safety, Andersson et al. found liquid hydrogen(H_2), methanol(CH_3OH), ammonia(NH_3) and dibenzyltoluene($C_{21}H_{20}$) to be

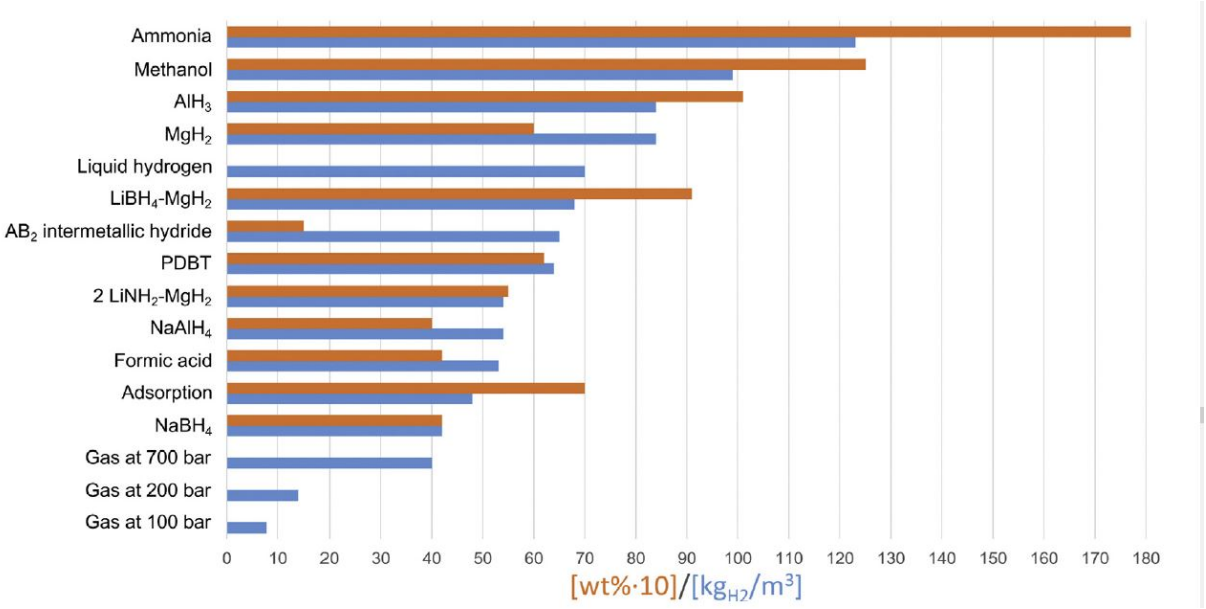

Figure 4.2: Volumetric and gravimetric densities for various hydrogen storage technologies. It is worth noting that the gravimetric density is multiplied by a factor of 10. [21]

suitable technologies for large-scale storage applications. With the wish from Longyearbyen Community Council to promote a green energy value chain, the emissions associated with the production of these substances need to be taken consideration before going forward in selecting based on technology.

Production methods

For hydrogen to be classified as renewable, it must be produced through water electrolysis, and is then often referred to as *green hydrogen*. The total reaction of electrolysis of water is stated in equation 4.1[22].

$$2\,H_2O \longrightarrow 2\,H_2 + O_2 \tag{4.1}$$

The production of green hydrogen is highly feasible, and from 1949 to 1993 hydrogen was produced by Norsk Hydro in Glomfjord, as a step in fertilizer production. With hydrogen catching interest for energy purposes, production in Glomfjord is set to reopen in 2023.[23] An alternative route to hydrogen is stripping fossil gas, methane predominantly, from its hydrogen through the production of synthesis gas, as seen in equation 4.2.

$$CH_4 + H_2O \longrightarrow CO + 3\,H_2 \tag{4.2}$$

This process produces carbon monoxide, which will result in carbon dioxide when reacting with oxygen. If the carbon dioxide is deposited in the atmosphere, the hydrogen produced is considered to be *grey hydrogen*, as it results in the emission of greenhouse gases. Hydrogen produced by synthesis gas derived from carbon, is regarded as *brown ammonia*[24] If the carbon dioxide produced in grey or brown hydrogen production is captured before reaching the atmosphere, it can be stored in underground geological formations. Over time the carbon dioxide will solidify due to the immense heat and pressure, and in this way, it will not reach the atmosphere. This is the fundamental principle of carbon capture

technology, and if it is applied in hydrogen production, the produced hydrogen is considered neutral regarding the global greenhouse gas balance. When hydrogen is produced from fossil sources, and carbon capture technology is used to permanently store the carbon dioxide made during its production, the hydrogen is regarded as *blue hydrogen*. The production of blue hydrogen is feasible, and in early 2020 a group of companies led by energy company BKK, announced a pilot-project producing blue hydrogen at Mongstad Energipark.[25]

The most wide-spread method for producing ammonia is by the Haber-Bosch process, which is stated in equation 4.3.[26]

$$N_2 + 3\,H_2 \longrightarrow 2\,NH_3 \tag{4.3}$$

As ammonia is composed of pure hydrogen, the origin of the hydrogen decides if the ammonia can be considered green, blue or grey. To satisfy the wish set by Longyearbyen Community Council, only *green ammonia* or *blue ammonia* is regarded to be relevant for the Longyearbyen application.
For methanol, its most wide-spread way of synthesizing is through the production of synthesis gas derived from fossil sources such as coal or methane, as seen in equation 4.4.

$$CO + 2\,H_2 \longrightarrow CH_3OH \tag{4.4}$$

Around the globe, methanol is being produced as a bi-product from other carbon dioxide intensive processes, and it has proved its worth, being established for use in cars and electricity generation in China and India. In the future, the hopes are that renewable methanol can be produced through the hydrogenation of captured carbon dioxide, or by using biomass as a source for carbon dioxide. But as of now, and not in the foreseeable future, it is not possible to produce methanol in a large scale which could be considered green.[21]
Dibenzyltoluene is classified as a liquid organic hydrogen carrier (LOHC) by Andersson et al, and is a group of materials characterized by their reversible hydrogenation and dehydrogenation in liquid state. LOHCs as a field are being researched, and no data has been found for the large-scale utilization of dibenzyltoluene.[21]
With the wish from Longyearbyen Community Council to promote a green energy value chain in the renewal of the local energy system, methanol and dibenzyltoluene are not seen as viable options due to their current technological state. Only the use of green and blue liquefied hydrogen and ammonia is deemed to be compliant with the wishes from Longyearbyen Community Council. The feasibility of using the technological solutions for large-scale storage of liquefied hydrogen and ammonia for the Longyearbyen application is explored in the upcoming sections.

4.1.1 Liquid hydrogen

With a volumetric density of 70 kg/m^3 at atmospheric pressure, liquid hydrogen is a sought after hydrogen distribution medium. For hydrogen to liquefy, the gas needs to be compressed and cooled for it to reach its condensing temperature of -253°C. At this temperature, the hydrogen is highly exposed for ambient heat transfer leading to vaporization inside the storage, which causes a pressure build-up in the storage vessel. If the boil-off is not handled, and compressed back into liquid state, the storage vessel needs to

be vented, to avoid the gas pressure reaching hazardous levels. This way the boil-off not only symbolizes an energy loss, but could also cause a loss of hydrogen in mass.
To minimize the boil-off rate, the ambient heat transfer must be held to a minimum. This calls for a sophisticated tank design, which minimizes the surface-to-volume ratio and advanced insulation. The most common design consists of a spherical tank that is isolated through a double wall barrier with a high vacuum in between them, making the heat transfer through conduction and convection minimal. If the execution of the design is successful, the boil-off rates could be lower than 0,1% per day.[21]
An advantage of storing hydrogen in pure form, is that it can be used without going through a dehydrogenation process. As for adsorbed or chemical storage technologies, energy must be applied to break hydrogen from its bonds.

4.1.2 Ammonia

With its favorable volumetric and gravimetric density, ammonia (NH_3) is an attractive hydrogen storage medium. At -33°C and atmospheric pressure, ammonia is in liquid state, having a volumetric density of 681,8 kg/m^3 with 17,7 mass% hydrogen.
Due to being used as a fertilizer, seasonal ammonia storage systems are well tested, and a common way of storage is in liquid state. To minimize ambient heat transfer, storage tanks are insulated with a double wall and to avoid pressure build-up, the boil-off is compressed back into liquid state. A common boil-off rate for an ammonia storage system is stated to be 0,1% per day.[27][28]
The dehydrogenation of ammonia is regarded to be the most challenging aspect of implementing ammonia as a hydrogen storage medium. The most prevalent way of conversion is through thermo-catalytic decomposition, which is the reverse reaction of ammonia synthesis. Ammonia starts to decompose spontaneously at 200°C. Depending on the catalyst temperatures, 600-900°C must be supplied to achieve complete conversion. Research is now focused on finding catalysts that enable high conversion rates at lower temperatures.[21]

4.1.3 Summary

For liquid hydrogen, infrastructure is still under development. At the time of writing, Kawasaki Heavy Industries is completing the world's first liquefied hydrogen carrier, Susio Frontier. The tanker is stated to have a storage capacity of 1250 m^3, and its completion is set to late 2020. Kawasaki states that the tanker will be used primarily for technology demonstration, and as a proof of concept. It is reasonable to believe that when commercialized, the loading capacity of a liquid hydrogen tanker will be far greater than 1250 m^3. At present day, we can hardly assume that the technology will be ready for widespread commercialization by 2030. Especially to be utilized in a scale needed for power generation in Longyearbyen, which is estimated to consume just under 38000 m^3 of liquid hydrogen yearly, based on estimations by Ringkjøb et al..[29]
The large volumes needed, potentially calls for innovation in storage technology for the use of liquid hydrogen in Longyearbyen to be feasible. As of today, the world's largest liquid hydrogen storage was built by NASA in the 1950s-1970s, and holds 3400 m^3.[30]
Infrastructure for shipping and storing ammonia, on the other hand, is already a widespread and proven technology. The needed volume of ammonia to store the energy needed from hydrogen, is calculated to be peaking at just over 22000 m^3 in 2030. When shipping

ammonia, specialist tankers are used with installed cooling- or compression systems to avoid pressure build-up during freight. The class of tanking vessels used are the same as when shipping liquefied petroleum gas (LPG). As reference, LPG-tankers Höegh LNG owned Arctic Princess and Arctic Lady, who are in shuttle service delivering petroleum gas to Melkøya, has a storage capacity of just under 150000 m^3. Making it reasonable to assume that Longyearbyen's yearly ammonia need could be supplied in a single delivery.[31]
As reference for large-scale ammonia storage, engineering company McDerrmott have provided two tanks of 50000 tonnes net capacity to Mesaieed in Qatar. Making it reasonable to believe that the just 15000 tonnes of ammonia supplied to Longyearbyen could be stored in a single storage tank.[32].
On this basis, *ammonia* is considered the most promising method for storing large amounts of hydrogen in Longyearbyen and is selected as hydrogen storage medium for the system.

4.2 System for power generation

With ammonia as the selected form of hydrogen storage, multiple solutions emerge for power generation. The most prominent technologies are fuel cells, combustion engines and gas turbines.

4.2.1 Fuel cell system

Ammonia can be used as fuel for fuel cells in two ways, either injected in pure form through the use of direct ammonia fuel cells, or through decomposing the ammonia and using the decomposed hydrogen as fuel for the fuel cell. Direct ammonia fuel cells are currently being researched, but are yet to be proved feasible for applications outside of the laboratory.[33]
For fuel cell systems fueled on hydrogen derived from ammonia, there are currently two companies offering fuel cells and complete systems within this niche. GenCell Energy offers fuel cell power solutions based on ammonia primarily for telecommunication and reserve power. The GenCell A5 is a system designed for off-grid power generation, and consists of an alkaline fuel cell, an ammonia storage, a thermo-catalytic ammonia decomposer and power conditioning system. The other company offering fuel cell technology for hydrogen derived from ammonia is AFC Energy. Their alkaline fuel cell Hydro-X Cell (L), is capable of providing electric power outputs of 400 kW.[34][35]
For marine applications, the supply vessel Viking Energy is installing a 2 mega watt fuel cell system, fueled by hydrogen derived from ammonia. The innovation is part of a research project led by Equinor, Yara, Prototech and NCE Maritime Clean Tech, and the fuel cell system is set to be installed by 2024.[36]
During the work with this thesis, neither GenCell Energy nor AFC Energy was willing to offer data sheets for their systems, beyond what is already available through their websites. The data available is not sufficient for the systems from GenCell Energy and AFC Energy to be used as reference systems.
Through literature research, other reference systems were found, and a system used to generate power for a fuel cell city car by Karl Kordesch is found suitable for scale-up.

4.2.2 Combustion engines

Combustion engines utilizing ammonia have been tested for nearly a century, but never made its claim, primarily due to its low heat heating value of 18,6 MJ/kg. Which is merely 40% of its competitors' gasoline and diesel. In later years, ammonia has gained new interest because of its ability to provide carbon-free combustion. As a result, ammonia fueled combustion engines are being developed for a wide range of applications all over the world. The issues with low heating value seem to be solved by decomposing a fraction of the ammonia to its compounds, nitrogen and hydrogen before combustion. Hydrogen has a lower heating value of 120 MJ/kg, giving the mixture a diesel-like heating value and promotes a cleaner combustion.[37][38]
Especially the comprehensive investments are being made in the marine industry are worth noting. MAN Energy and Wärtsila are leading the innovation, with both companies announcing ammonia fueled engines targeting to replace equivalent LPG and diesel engines. Additionally aiming to enable rebuilds of existing LPG engines to be fueled of ammonia.[39][40]
For power generation from a combustion engine, the world relies on the rough and rugged diesel cycle. At the time of writing, there are no commercial ammonia fueled compression ignition engines available on the market, and the data found on the subject is scarce. Which may imply that it is in the works, or that few research groups currently exist on the subject. The latter is implied by Dimitriou et al.[37]

4.2.3 Gas turbine

As for combustion engines, the use of ammonia in gas turbines was researched in the 20th century, but abounded because of low combustion efficiencies related to its low heating value. With carbon-free combustion being sought after, the field of ammonia fueled gas turbine has gained new interest, being researched throughout the world.[41]
Studies show that the addition of hydrogen in ammonia combustion improves combustion efficiency effectively, while at the same time reducing the formation of NOx in the exhaust. Hydrogen can easily be decomposed from ammonia under the presence of a catalyst, using parts of the excess heat from the combustion to fuel the decomposition process. Kurata et al., states that research still needs to carried out to determine the combustion characteristics of ammonia and hydrogen blends for the use in gas turbines.[42]
Currently, no ammonia fueled gas turbines are commercially available, but with the addition of hydrogen in the fuel mix they are technically feasible. In the working process, systems of reference have been found, but none of them are developed to extinct that they can be directly implemented as the system of this thesis.

4.2.4 Summary

The utilization of ammonia for power generation is a field of rapid development, which leads to the access to data and reference system being scarce. It is therefore decided to move forward with an up-scaled version of the fuel cell city car system by Kordesch, which is fueled with hydrogen derived from ammonia, as it is the only system found with a fitting reference system.

5. System description

At the time of writing are fuel cell systems fed with H_2 derived from ammonia is a technology under development. Currently Israeli GenCell and British AFC Energy are spearheading this niche market, but neither of them were willing to share system design blueprints as they regard it to be highly sensitive information in such a small and rapidly developing market.
Since the access to state of the art reference systems is limited, a system concept for a fuel cell city car, developed by austrian chemist Karl Kordesch in the early 1970s is used as a reference system, seen in figure 5.1. The system was revisited by Kordesch et al. in 2000, being stated as a proof of concept with further design experiments under investigation at the Technical University of Graz and the Technical Univeristy of Vienna.[43][44]

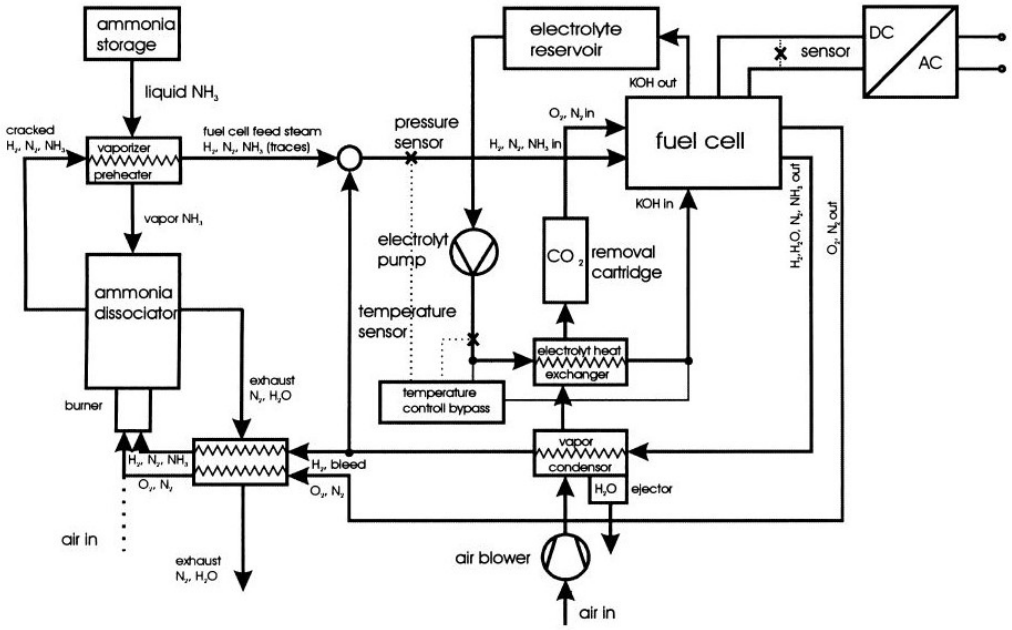

Figure 5.1: Process schematic for fuel cell city car by Kordesch et al.[44]

The system by Kordsech et al. uses a 6 kilowatt a hydrogen-air alkaline fuel cell (AFC), fed by H_2 derived from ammonia to produce a voltage of 90 V. The ammonia, NH_3, is decomposed in an endothermic reaction to H_2 and N_2 under the presence of a catalyst and high temperature maintained by combustion of the surplus H_2 from the AFC. The CO_2 of the incoming air is removed through a soda lime scrubbing system, a system where the absorbent solution is discarded when saturated with CO_2. Circulation of the fuel cells electrolyte acts as a cooling system for the AFC.
While working with the system a few adaptations were made, and the complete system is presented in figure 5.2. Components and sub-systems are numbered and presented in table 5.1.

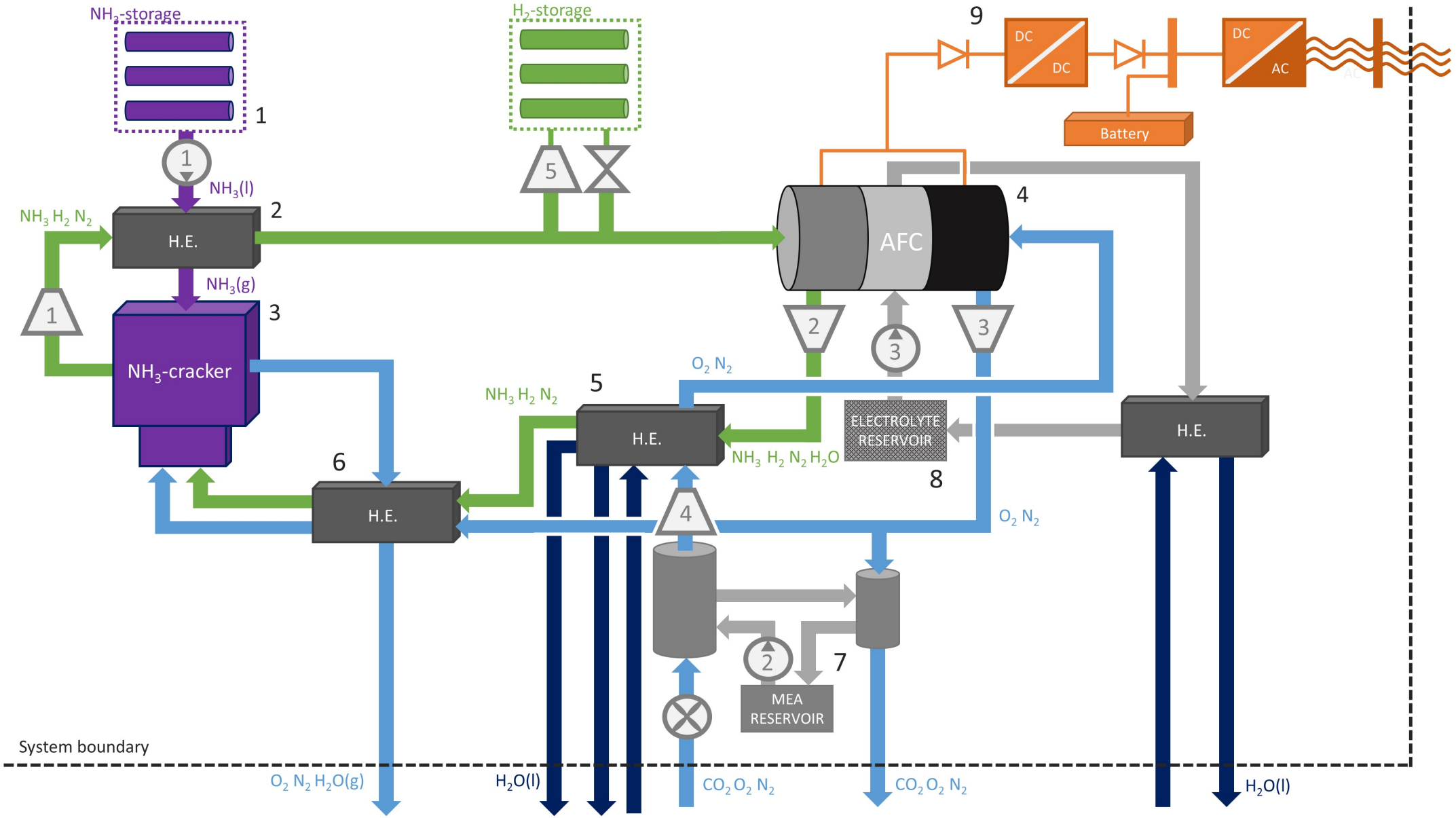

Figure 5.2: AFC-system schematic

Number	Component
1	Ammonia storage
2	Heat exchanger for H_2-mixture and NH_3
3	Ammonia cracker
4	Alkaline fuel cell
5	Condensing heat exchanger, separating H_2O
6	Heat exchanger for exhaust gas and combustion reactants
7	CO_2-scrubber
8	Electrolyte circulation system
9	Power conditioner

Table 5.1: Numbered list of components.

The most prominent system adaptations are the continuous scrubbing of CO_2 through the addition of a regeneration column using surplus air from the AFC as flush gas, and the introduction of a power conditioning system which converts the electric DC power produced by the AFC to high-quality AC power through energy storage and an inverter system. The addition of internal energy storage, in the form of a gaseous H_2-storage and a battery pack, allows the system to be self-sufficient in dealing with load variations with transient times of multiple time constants.
The system boundary is set so the chemical energy of H_2 bound in liquid ammonia is entering from storage, and energy leaves as electricity and heat transferred to the district heating system. The AFC-system's interaction with the district heating have been examined, and three operational scenarios have been calculated, when the operating temperature of the district heating is 60°C, 80°C and 120°C.
The upcoming chapter gives a more detailed insight into the AFC-system's components and sub-systems.

6. System components

6.1 Ammonia storage

Seasonal ammonia storage systems are well tested. For the system it is decided that *the Ammonia is stored as a liquid, refrigerated to -33°C, at atmospheric pressure.* To minimize ambient heat transfer, storage tanks are insulated with a double-wall, and to avoid pressure buildup, the boil-off is compressed into liquid state. In a way, seasonal storage facilities mimic refrigeration plants as seen in the figure below.

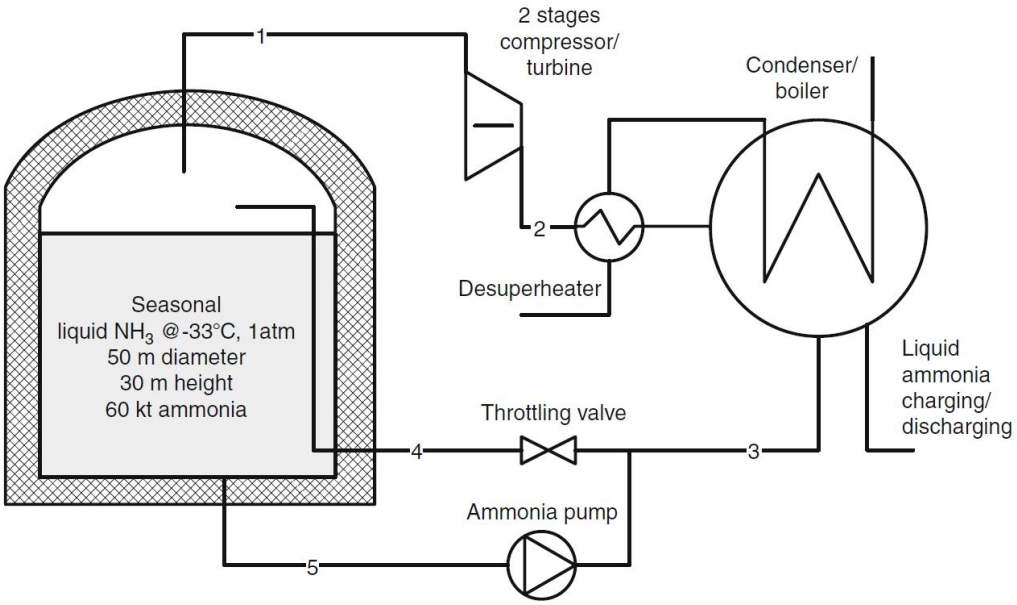

Figure 6.1: Example of a seasonal ammonia storage system[27]

For the storage temperature and pressure to be kept constant, the circulation of ammonia through the refrigeration system must compensate for the boil-off rate. The daily boil-off for the storage system is about 0,1%. At atmospheric pressure, ammonia has the latent heat of 1370 kJ/kg. Which results in about 1,4 kJ of heat that needs to be deposited per kilogram of liquid ammonia each day.[27][21] [28]

6.2 Heat exchanger for H_2-mixture and NH_3

Heat exchangers enable heat to transfer between fluid streams of different temperatures within a system, utilizing surplus heat which in other cases would have been wasted. The

heat transfer takes place through conduction, by leading the fluids on opposite sides of a metal sheet or tube. To maximize the heat transfer, the surface area of the fluid touching the metal is maximized by the fluid flow having such velocity that it acts turbulent.[45]
In general heat exchangers are classified into tubular heat exchangers, plate heat exchangers, extended surface heat exchangers and regenerators. These classifications are then split further into sub-categories, based on their operational properties.
Tubular heat exchangers essentially consists of a tube fitted into another tube or shell, where the fluids flow through in their separate casings, and heat is transferred through the metal wall touching both fluids.
Plate heat exchangers consist of sheets of metal laid in layers, with the hot and cold fluids flowing through every other cavity, ensuring a large surface area for the heat transfer to occur. Number of sheets and flow directions are important parameters for the plate heat exchanger.
Extended surface heat exchangers are used in applications where the heat transfer coefficient is low. To increase the heat transferred, fins and plates are inserted into the heat exchanger, increasing the fluid's length of travel through the system.
In a regenerative heat exchanger, also known as a regenerator, the heat from the hot fluid is passed through a thermal storage medium before being transferred to the cold fluid. The medium can be another fluid as well as a solid, for example as a rotating disc which is in direct contact with both the hot and the cold fluid.[46]
Since different needs apply to each specific heat transfer the categories stated above could be combined, and numerous design variations have been developed with flow direction, surface area, construction materials and phases of fluid being important system parameters.[47]

For the liquid ammonia and H_2-mixture heat exchanger, the objective is to cool the freshly decomposed H_2 from the ammonia cracker's temperature of 600°C to the AFC's working temperature of 125°C. Simultaneously, the liquid ammonia is vaporized, and its temperature is raised as much as possible, before entering the ammonia cracker. The operating pressure is 2,2 bar. The basic schematic for the heat exchanger is seen in figure 6.2.

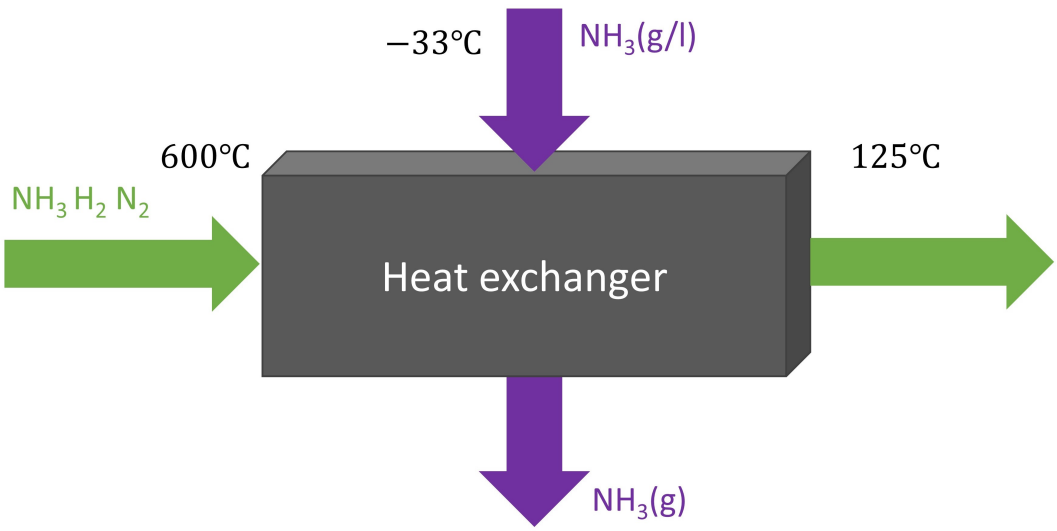

Figure 6.2: Basic schematic for the H_2/N_2-mixture and NH_3 heat exchanger

The selected design is a counter-current shell-and-tube heat exchanger, and is preferred due to its ability to act as an evaporator, with the ammonia transitioning to gas state. The gaseous H_2-mixture flows through the shell side of the heat exchanger. Since gases generally have very low thermal conductivity compared to liquids, a series of fins must be installed to increase the contact area between the H_2-mixture and the ammonia, which subsequently raises the system's heat transfer coefficient. The heat transfer can be improved further if the ammonia stream is split over several tubes inside the shell, but this needs to be considered through a cost-benefit analysis, as the system does not have size limitations. Furthermore, materials must be able to withstand ammonia's corrosive nature, especially since flows are highly turbulent.[48]

6.3 Ammonia cracker

For the hydrogen to be utilized by the fuel cell it must be dissolved from the hydrogen from the ammonia. The ammonia decomposition is described by the following endothermic reaction:

$$\mathrm{NH_3} + 46\,\frac{\mathrm{kJ}}{\mathrm{mol\,NH_3}} \longrightarrow \frac{1}{2}\,\mathrm{N_2} + \frac{3}{2}\,\mathrm{H_2} \tag{6.1}$$

As described through equation 6.1, the reaction consumes 46 kJ pr. mole of NH3 that reacts. For the endothermic reaction to occur continuously, heat must be supplied to the reaction at the same rate. The devices designed to dissociate ammonia, and hereby maintain a heat flow equilibrium, are referred to as 'splitters' or 'crackers'.There are several cracker designs available, but they all have in common is the use of a catalyst and a heating solution, often a type of furnace or a combustion device.[49][50]
A catalyst is a substance which can increase the rate of a chemical reaction without degrading or disrupting the chemical equilibrium.[51] There is a wide variety of catalysts used for ammonia decomposition ranging from low-cost metals like iron and nickel, too noble metals like platinum and ruthenium. The catalysts performance can be further improved by attaching porous materials to the metal's surface. A measure that enables higher reaction rates, due to the catalyst surface area being increased. The catalyst usually comes in the shape of sub-millimeter sized pellets, which are stacked inside a metallic tube with a high length-diameter ratio. Gaseous ammonia then passes through the metallic tube and the endothermic reaction occurs. For the ammonia cracker, a *Nickel catalyst with a cerium-dioxide surface* catalyst have been selected. The Ni/CeO_2 catalyst is favored due to its low cost compared to ruthenium-based catalysts. Its performance for ammonia conversion rate is plotted by temperature in figure 6.3 [49] [52] [53]
In figure 6.3 Ni/CeO_2 appears to achieve full conversion of the ammonia from 550°C. Full conversion is not likely, and an assumption of *a 99,8% ammonia conversion rate at 600°C* is made for further calculations.

To provide sufficient heat to keep the operating temperature stable in the cracker, several cracker designs have been developed. The solutions range from converting chemical- or electrical energy to heat, to utilizing waste heat form other system processes.
For the thesis, an *external furnace cracker* design is selected. The schematic of the cracker design is presented in figure 6.4.
The external furnace cracker is favored due to making use of unreacted hydrogen from the fuel cell, which increases the efficiency of the overall system. The ammonia/hydrogen

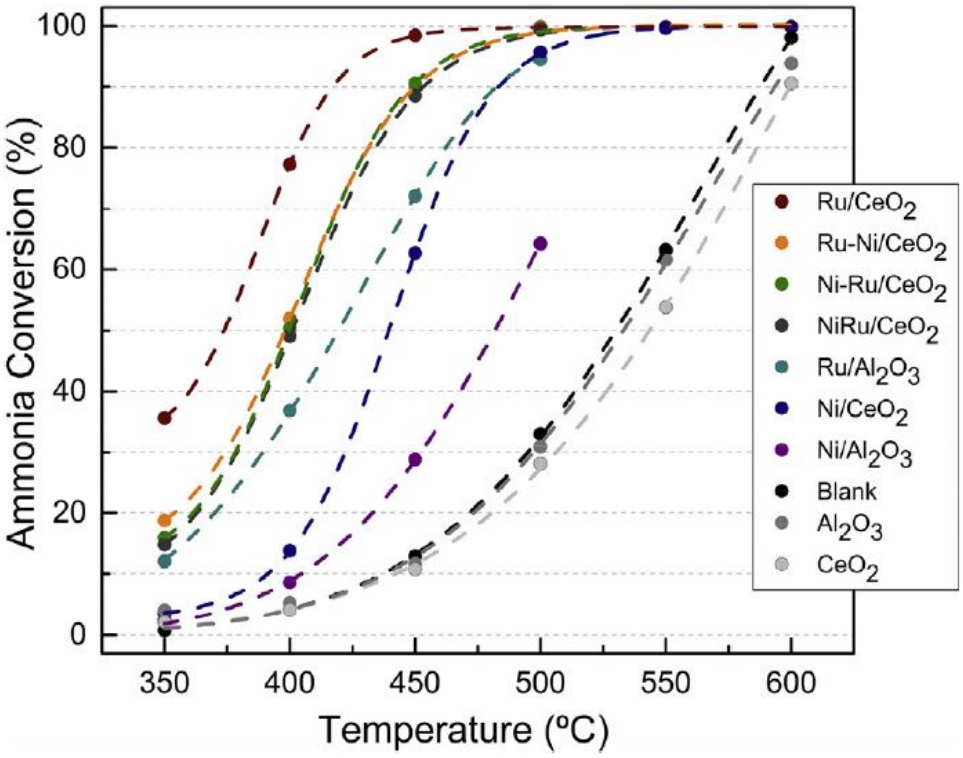

Figure 6.3: Ammonia conversion rates at temperatures 350-600 °C. Ni/CeO_2 plotted in dark blue. Experiment conducted by Lucentini et al. (2019).[53]

blend combusts with the excess O_2/N_2 mixture. The complete combustion reaction is given i equation 6.2, and is calculated in section 7.3 [49].

$$0{,}0083\,NH_3 + 0{,}9916\,H_2 + 0{,}5021\,O_2 + 2{,}7821\,N_2 \longrightarrow 2{,}7863\,N_2 + 1{,}0042\,H_2O \qquad (6.2)$$

The flue gasses consist of N_2 and H_2O, but traces of NOx are bound to be formed. The exhaust is ejected from the cracker, and is used to pre-heat the incoming reactants in the heat exchanger discussed in section 6.6.

6.4 Alkaline fuel cell

Depending on catalyst and temperature, the ammonia cracker has a conversion rate in the range of 99,5-99,99%. This implies that the fuel cell will be exposed to a hydrogen stream with a NH3 contamination up to 5 000 ppm. One of the most characteristic properties of ammonia is its basicity. The high pH of ammonia cause problems for widespread fuel cell technologies such as PEMFC (Proton exchange membrane fuel cell) and SOFC (Solid-oxide fuel cell). Even at very small ammonia concentrations problems arise. For instance, ammonia concentrations as low as 13 ppm are shown to cause damage to a PEM fuel cell's acidic polymer membrane, affecting the fuel cell's performance drastically. Concentrations over 50 ppm is enough to make permanent damage on the cell.[49]
To attain hydrogen from ammonia with contamination levels under 10 ppm, the dissociation must take place at high temperatures under the presence of a noble catalyst material, like ruthenium. Reaching these the needed temperatures require large amounts of heat,

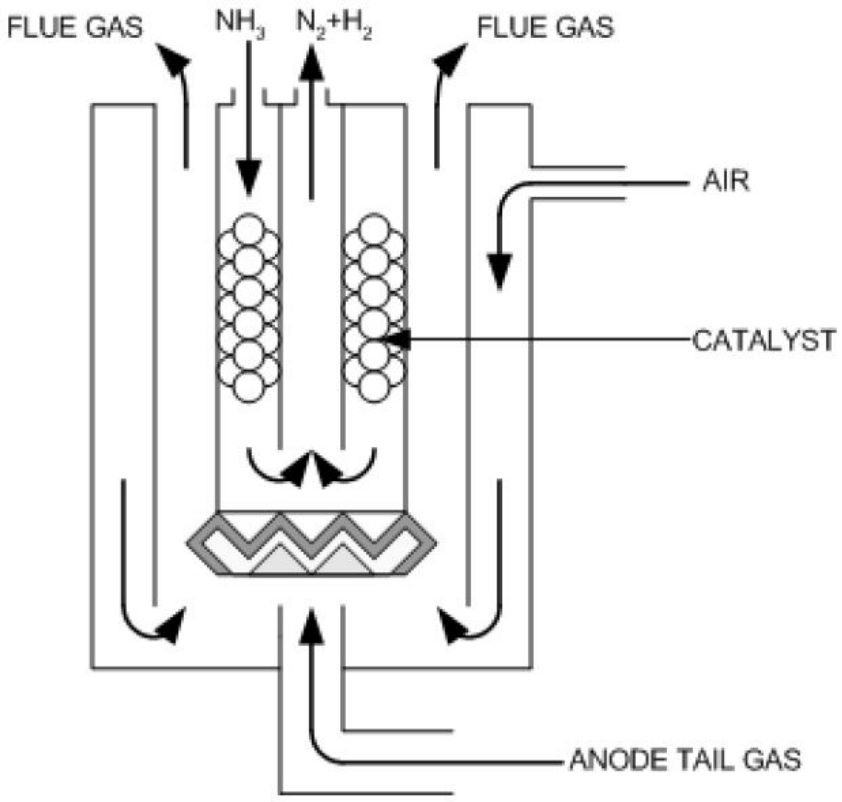

Figure 6.4: Schematic of an external thermal cracker[49]

making PEM and SOFC fuel cells unsuited for the Longyearbyen application.

The alkaline fuel cell (AFC) is well suited to be fed hydrogen dissociated from ammonia. The residual ammonia is well tolerated by the cells electrolyte, membrane and catalyst, enabling the use of cheaper catalysts at lower splitting temperatures, as a higher concentration of ammonia is tolerated by the fuel cell.
Alkaline fuel cells were made famous in the 1960s through "The Bacon cell" being adopted for the Apollo space program. Being apart of the space program gave the impression of fuel cells was expensive and specialized systems, and is partly to blame for its lack of popularity. During the 70s AFCs were tested for various applications. Many of the systems were successful, but issues such as cost, reliability, ruggedness and safety put a stop for the AFCs further popularization. Throughout the 1980s and -90s research on AFCs was scaled down, mainly because of the emergence of other fuel cell types, such as the low-temperature PEMFC. Due to the AFCs ability to feed of hydrogen from dissociated ammonia, the AFC has caught new interest as the need for green energy solutions has emerged. Currently, AFC Energy and GenCell is spearheading the market with their modular systems for off-grid- and back-up power fueled with hydrogen derived from on-site ammonia. The working principle of an AFC is seen in figure 6.5.[54]
The operation of an alkaline fuel cell is based on two chemical reactions, one on the anode and one on the cathode side. The reaction on the anode side is:

$$2\,H_2 + 4\,OH^- \longrightarrow 4\,H_2O + 4\,e\text{-} \qquad E° = -0{,}282\,V \tag{6.3}$$

with E°being the standard electrode potential. Incoming hydrogen reacts with OH^- ions

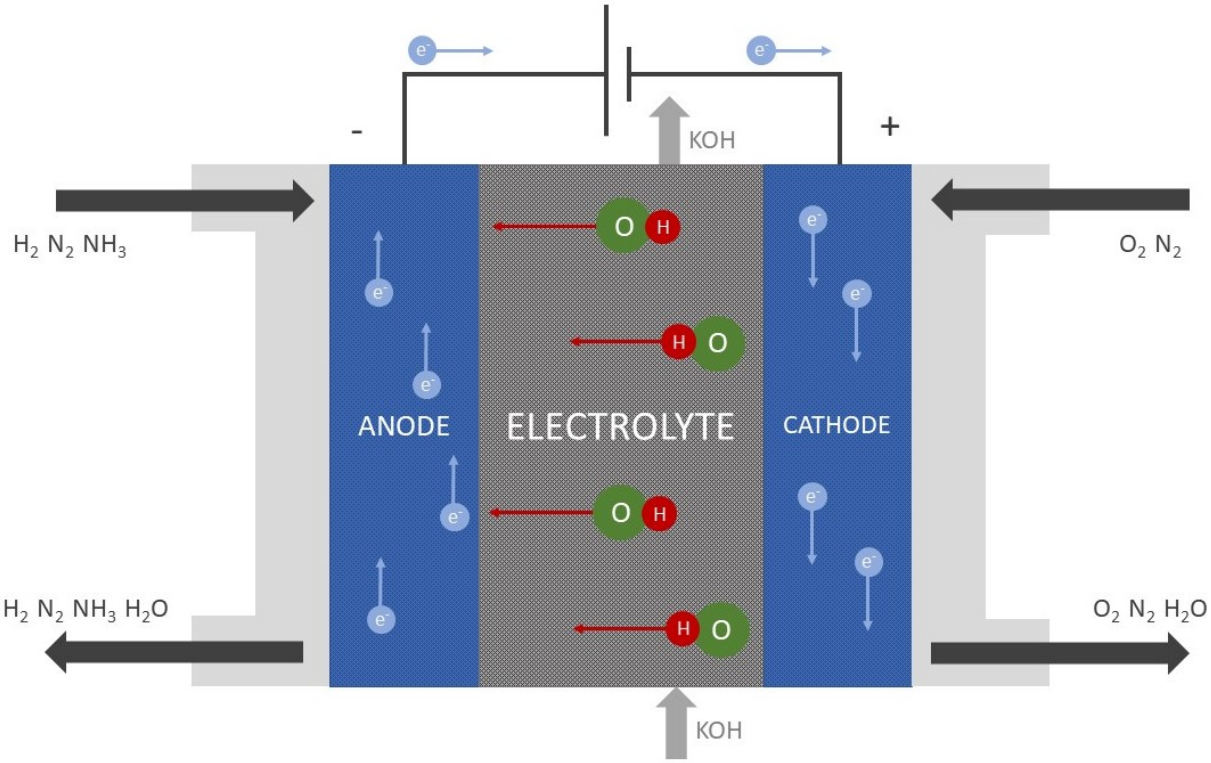

Figure 6.5: Diagram of an alkaline fuel cell fueled with hydrogen derived from ammonia and a circulating electrolyte

to form water and surplus electrons, which pass through the external circuit. When reaching the cathode the electrons react with the incoming oxygen and water, which makes a substantial part of the electrolyte, to form OH^- ions in the following reaction:

$$O_2 + 4\,e^- + 2\,H_2O \longrightarrow 4\,OH- \qquad E^\circ = 0{,}40\,V \tag{6.4}$$

The OH^- ions pass through the electrolyte, where the ions react with the incoming hydrogen to form water and electrons and the cycle is complete.
The selection of material and operating parameters are presented in the table 6.1. The working principles and reasoning behind the selections is elaborated over the coming subsections.

Component/setting	**Material/parameter**
Anode material	Carbon powder binded with PTFE with a nickel-foam catalyst
Cathode material	Carbon powder binded with PTFE with a nickel-foam catalyst electroplated with silver
Electrolyte	Potassium hydroxide (KOH)-water solution, with 35 wt.% KOH.
Electrolyte system design	Circulating electrolyte
Stack design	Bipolar plates
Operating temperature	125°C
Operating pressure	2,2 bar
Fuel utilization coefficient	0,87

Table 6.1: Operational parameters for the alkaline fuel cell

6.4.1 Electrodes

The anode and cathode of an alkaline fuel cell are similar by design, and their general design is elaborated over the next paragraphs. Differences are then discussed.
The pioneering alkaline fuel cells used in the space program had electrodes made of sintered nickel powder. Nickel was chosen due to its conducting and catalytic capabilities. To prevent liquid electrolyte from flooding the electrode, the nickel is formed into a fine-pored structure on the liquid-facing side, while being more porous on the gas side.
As of today, most alkaline fuel cells employ a carbon-based gas diffusion layer (GDL) along with a metal catalyst to enhance reaction rates. To ensure controlled permeation of water from the liquid electrolyte into the GDL, polytetrafluoroethylene (PTFE) is used to bind the carbon black powder. PTFE is a polymer that has great hydrophobic and corrosion-resistant properties, and is widely used in gaskets for the chemical industry. The metal catalyst is often in the form of a mesh, giving the metal a very low density. Its high porosity gives the metal a very high surface area, which enables a high number of reactions regarding to volume. The reaction rate can be raised further by electroplating the metallic mesh with another catalyst. Unlike PEM-fuel cells, the alkaline fuel cell does not rely on noble catalyst metals like platinum in its design. Noble metals are bypassed by raising the fuel cells working temperature. To control the amount of water coming in contact with the electrode, a thin layer of PTFE is applied to the electrodes gas side. Capillary forces enables tiny amounts of water to migrate through the PTFE, and reach the electrolyte. The AFCs composition of anode, electrode and cathode materials is presented in figure 6.6.[55][56][57]

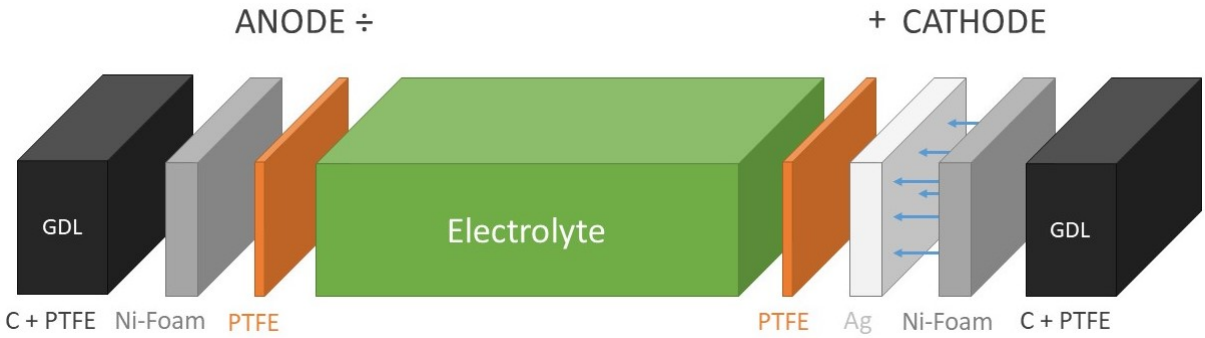

Figure 6.6: Diagram of the alkaline fuel cells electrodes, and their composition.

For the gas diffusion layer on both electrodes, a *carbon powder bound with PTFE* is selected. A wide range of carbon powder and PTFE is being used, and the precise formula must be decided by experts. As an example, Bidault et.al (2009) used a carbon black from Degussa called Printex XE2 with an average particle size of 35 nm blended with a PTFE from Alfa chemicals labeled TE3893-N. The solution had a PTFE/carbon-ratio of 2,5:1.
At the anode, a *nickel foam* is used for catalyst. Nickel is electroplated onto a web-shaped polymer foam. The polymer is then burnt under high temperature, leaving the nickel behind. The result is a web of nickel foam with higher porosity than the mesh from the previous paragraph. Which gives an even higher surface area, with a lower mass, making the foam technique favorable to mesh.
For the cathode, the *nickel foam is electroplated with silver.* The silver increases the catalysts conductivity and is proved to decrease both the Ohmic losses and charge transfer resistance. As origin for most of the voltage loss in the cell, making optimization of the

AFC cathode catalysts is a hot topic of research.

6.4.2 Electrolyte

Water-based solutions of potassium hydroxide (KOH) is used, almost exclusively, as electrolyte for alkaline fuel cells. This is due to KOH having higher ionic conductivity and being less costly than its competitor, sodium hydroxide solutions.
The electrolyte objective is to provide an efficient pathway for hydroxide ions to be transferred from the cathode to the anode. On this basis, the solution's KOH-concentration should be the concentration with the best ionic conductivity. In figure 6.7 the conductivity of a KOH-solution as a function of concentration and operating temperature.[57]

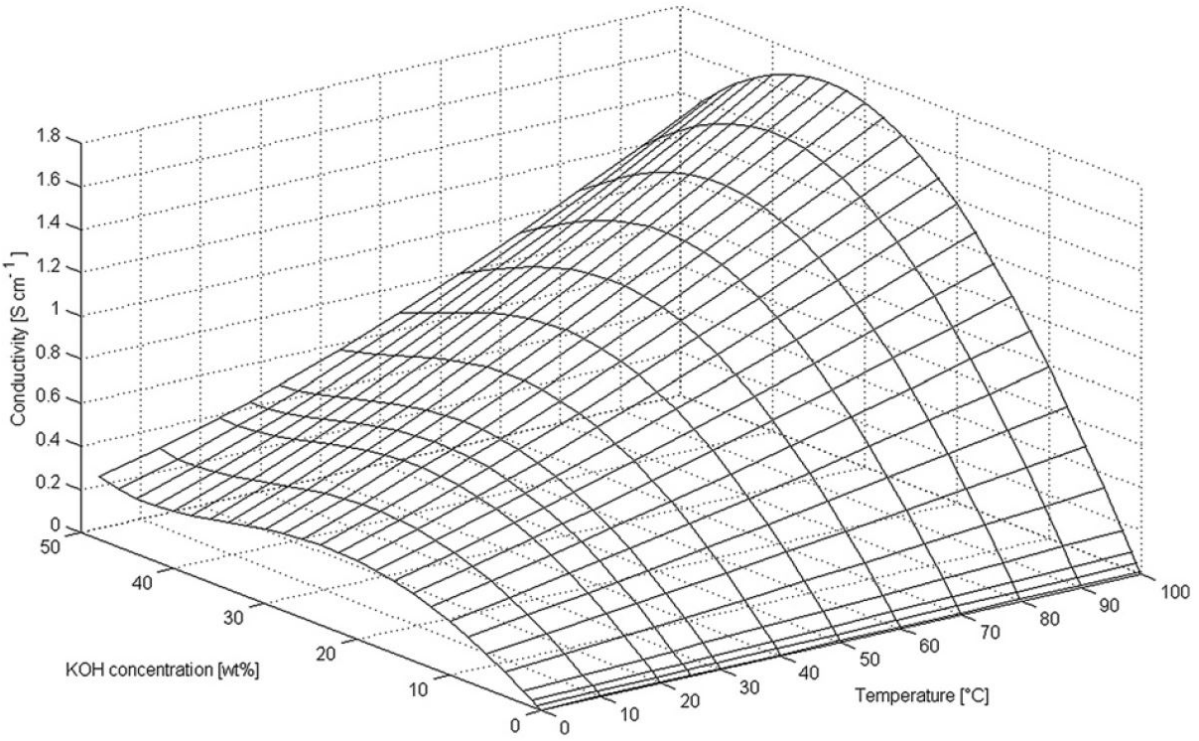

Figure 6.7: Conductivity for aqueous solutions of KOH, plotted as a function of working temperature and KOH-concentrations in the range of 0-100°C and 0-50wt% KOH.[58]

From the plot, it is evident that the electrolyte will have the best conductivity at higher temperatures with a concentration in the range of 30-40 wt%. In general, the plot indicates that conductivity increases with temperature, but peaks at a certain KOH concentration. This is consistent with commercialized AFC systems. As an example, the GenCell is stated to have a KOH-concentration ranging from 28-32 wt%. For the alkaline fuel cell, an *electrolyte KOH concentration of 35 wt%* is chosen.[**?**][34]

6.4.3 Electrolyte system design

The alkaline fuel cell has several solutions for its electrolyte management.
A circulating electrolyte solution is a system where electrolyte gets pumped through the

fuel cell. It requires piping, a holding tank, a cooling system and a pump, but has advantages such as being able to avoid water concentration at the cathode. From equation 6.3 and 6.4, it is clear that twice the amount of water is produced at the anode, than is consumed at the cathode. This water build-up could result in solidification around the cathode, and a circulating electrolyte will contribute to reducing this problem. Additionally, if the electrolyte is heated during start-up, it can cut back drastically on the systems start-up time.
As an alternative design, the static electrolyte solution is based on each cell having the electrolyte held in a matrix material between the electrodes. It is a simplistic design, with the ability to withstand any sudden change in orientation. The static electrolyte has clear durability issues due to the electrolyte cannot be replaced after it is installed, making it suited for pure oxygen applications primarily.
Other variations of electrolyte solutions exist, such as the dissolved fuel and the more recent anion-exchange membrane (AEM). In the AEMFC, the KOH electrolyte is replaced by a solid alkaline electrolyte membrane. The benefit of an AEMFC fuel cell is that it is solid-state, with no liquid electrolyte to leak, resembling the PEMFC. The AEM fuel cell is still under research, with problems concerning degradation and conductivity. Developers are targeting the AEMFC to operate at room temperature.
Historically, one of the AFC's main flaws, is that the electrolyte gets contaminated if exposed to ambient doses of CO_2. To use ambient air, the air must be scrubbed for CO_2 before entering the AFC, more in detail in section 6.7. Still, after scrubbing, a small amount of CO_2 will reach the electrolyte, and react with the KOH to form potassium carbonate, K_2CO_3. Over time this will cause decrease in OH^- concentration and lead to a decrease in electrolyte conductivity.[54]
To extend the AFC's lifetime, it must be possible to change the fuel cell's electrolyte easily. To make maintenance easy, a *circulating electrolyte solution* has been selected for the system. A circulating electrolyte makes it possible to use the electrolyte for cooling, and heat exchanging the hot electrolyte for district heating. More about this in section 6.8.

6.4.4 Stack design

The preferred fuel cell geometry is the anode, cathode and electrolyte being pressed together in the form of flat plates. These three plates make up a single cell, which generally produces a voltage of 0,7V. To build up voltage, single fuel cells are connected in series to form fuel cell stacks. The most prevalent way of building up voltage is by using bipolar plates, shown in the figure below.
The bipolar plate is an electrically conducting plate, which connects the cathode of one cell to the anode of the next. Enabling voltage to build up throughout the stack.
The bipolar plates also supplies the anode and cathode with its products and reactants. Channels are machined on each side of the plate, so that reacting gases can enter the cell and products can exit. An exploded-view is shown below.[59]

The fuel cell system should be equipped with bipolar plates, which is possible due to the circulating electrolyte solution. British fuel cell company AFC Energy specializes in alkaline fuel cells. They have developed MW-scale systems with bipolar plates, which can operate on both circulating and static electrolyte.[60]

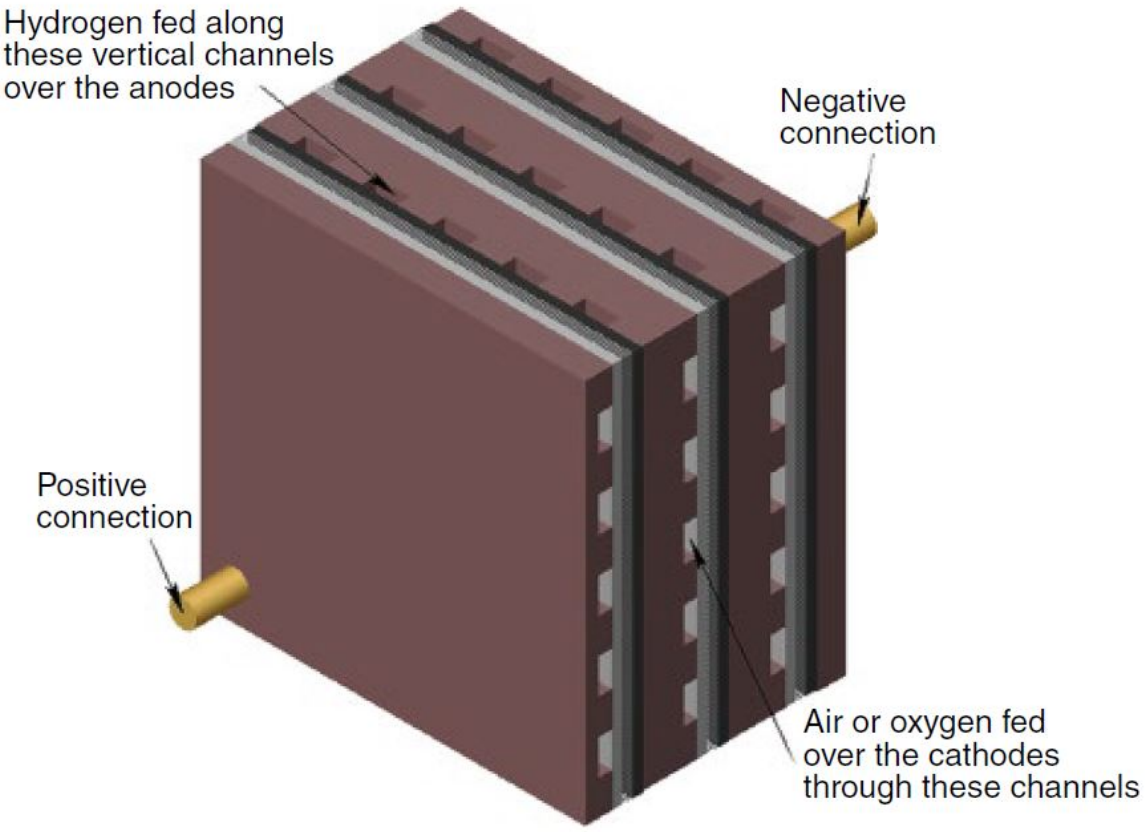

Figure 6.8: Here bipolar plates are used to form a three cell stack. The bipolar plate connects the anode of one cell to the cathode of its neighbour.[59]

6.4.5 Operating temperature

Raising the operating temperature has several effects on the fuel cell.
As elaborated in subsection 6.4.2 along with concentration, temperature affects the conductivity of the electrolyte. A higher temperature increases the conductivity of the electrolyte. Which causes a lowering of the voltage drop due to mass transport in the fuel cell.
Raising the operating temperature of the fuel cell enables an increase in the exchange-current density. Occurring at fuel cell activation, the exchange-current density can be visualized as a point where the chemical reaction at an electrode stabilizes, and the flow of electrons becomes uni-directional. For current densities below the exchange-current density, electrons can flow in both directions. Leading to low current densities through the electrode and a voltage drop in the fuel cell occurs. These unwanted voltage drops at the electrodes are known as 'overpotentials' in electrochemistry.[**?**]
On the negative side, a higher temperature reduces the fuel cells open-circuit voltage. This is due to a reduction in the change of Gibbs free energy of formation, which describes the maximum electrical energy released by the fuel cell.[**?**] (table 2.1, page 30) The change is Gibbs free energy is described by:

$$\Delta\bar{g}_f = \Delta\bar{h}_f - T * \Delta\bar{s} \tag{6.5}$$

where $\Delta\bar{g}_f$ is the change in Gibbs free energy of formation, $\Delta\bar{h}_f$ is the change in enthalpy of formation, T is the reactant temperature and $\Delta\bar{s}_f$ is the change of entropy. It is evident

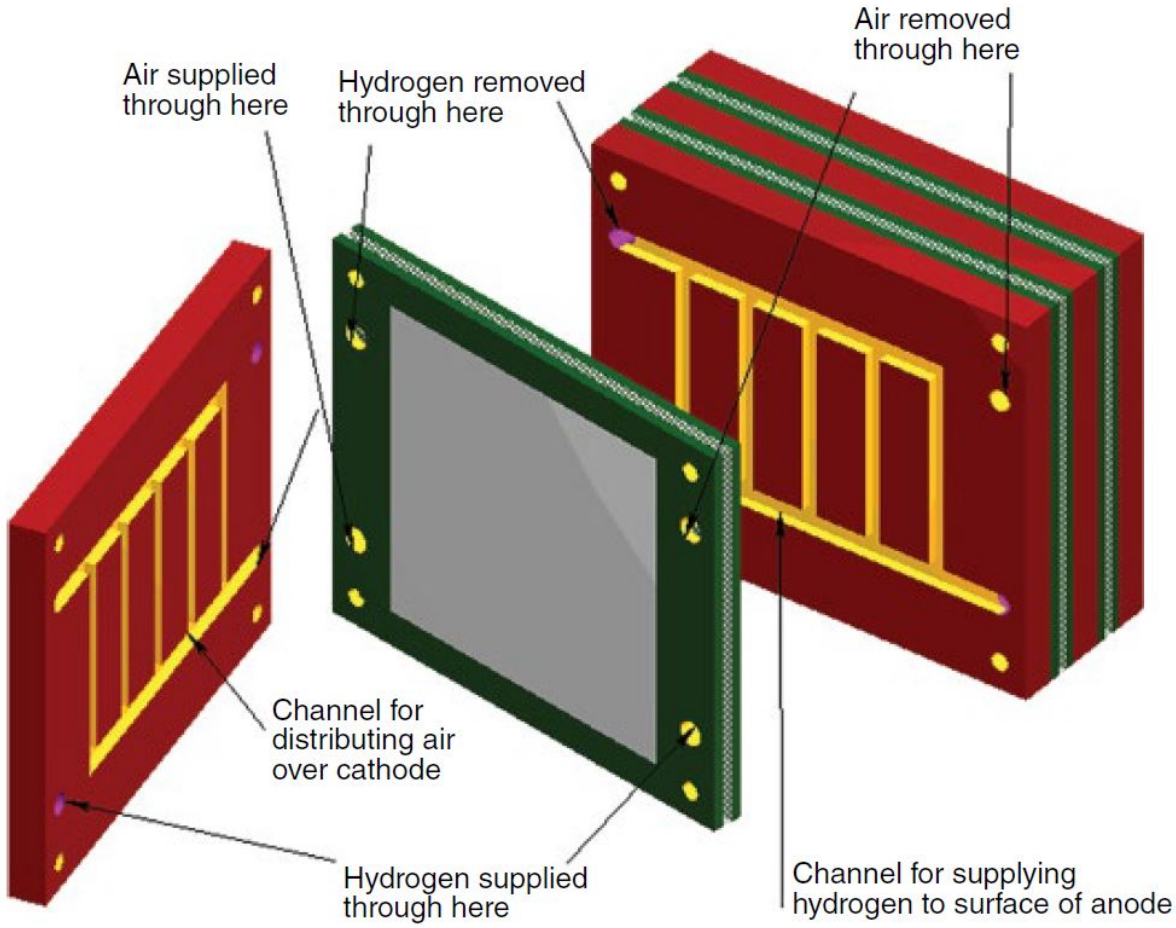

Figure 6.9: An example of how manifolding enables reactant and product mass flow through bipolar plate to the electrodes. [59]

that the term with reactant temperature and change in entropy will grow as temperature increases. This is backed up in literature. The open circuit voltage is then described with:

$$V_r = \frac{-\Delta \bar{g}_f}{2F} \tag{6.6}$$

Where V_r is reversible, open-circuit voltage, $\Delta \bar{g}_f$ is the change in Gibbs free energy of formation and F is the Faraday constant. By equation 6.6 its clear that a reduction, in temperature leads to a reduction in open-circuit voltage. The open-circuit voltage of the AFC is calculated in section 8.4.
It is worth noting that the drop in open-circuit voltage caused by the change Gibbs free energy of formation, is far smaller than the reduction in over-potential at the cathode. Which implies that increasing the operating temperature of a fuel cell, in sum, has more pros than cons.[61]
The *operating temperature of the AFC is set to 125°C.* This temperature is selected due to the product water will leave the fuel cell as steam at 125°C and 2,2 bar. From here, the latent heat of the steam can be utilized to heat air entering the fuel cell, while the remaining liquid/vapor mixture can be utilized for district heating.

6.4.6 Operating pressure

Since the fuel cell is fed a gas mixture consisting of nitrogen and ammonia along with the reacting hydrogen, the presence of the non-reacting molecules leads to some clogging of the anode catalyst. The clogging lowers the reaction rate, allowing some of the hydrogen to pass through the fuel cell without reacting with the anode, which leads to a decreasing fuel cell performance.
It is critical to control the fuel spill, not letting more of the hydrogen pass unreacted through the fuel cell than what is needed to fuel the combustion process in the ammonia cracker. Through pressurizing the reactants entering the fuel cell, a larger amount of hydrogen molecules is present in the fuel cell at all times. Together with controlling the incoming fuel stream, an elevated pressure enables a higher utilization of the fuel than at ambient pressure.[49]
To balance out the mechanical stress on the fuel cell, air must be supplied to the cathode side at an equivalent pressure. The set pressure is then referred to as the fuel cell's operating pressure. The operating pressure is set to 2,2 bar, which is higher than GenCell's off-grid power solution, the A5 operates at 1,5 bar. This is to ensure proper terms for utilization of fuel and air, which could be adjusted by regulating the incoming gas flows.[34]
To limit the possibility of electrolyte flooding the electrodes, the reactant gasses must be of higher pressure than the electrolyte. This operational detail is crucial to extend the fuel cell's lifetime.

6.4.7 Fuel utilization

To supply the ammonia cracker with the heat needed to maintain the reaction temperature, the AFC is fed with surplus hydrogen fuel.
The needed *fuel utilization coefficient is calculated to be 0,838*, meaning that 83,8% of the fed fuel is reacted in the fuel cell, while the remaining 16,2% is combusted in the ammonia cracker. Look to the the mass- and energy balances of chapter 7 and 8 for further information.

6.5 Condensing heat exchanger for H_2O and air

The main objectives for the condensing heat exchanger is to raise the temperature of the air headed for the AFC, and separate water from the AFC's anode exhaust. At 2,2 bar and 125°C, the water in the H_2-mixture is on the brink of condensation. Therefore, it is assumed that the condensing water is the only contributing factor in the heat transfer to the air. The heat available in the condensing water is far superior to the heat needed to raise the temperature of the air from 0 °C to 125°C, which is the temperature of the condensing water. This results in the H_2-mixture leaving the heat exchanger with water in vapor-liquid-mixture. To ensure a complete phase transition, separating the water from the H_2-mixture, the H_2-mixture passes through a second heat exchanger, which circulates water connected to the distribute heating system, as seen in figure 6.10.
For the condensing heat exchanger, a counter-current shell-and-tube design is preferred due to its ability in acting as a condenser. The heat exchanger consists of a split shell, and can be thought of as two sub-systems within the heat exchanger. In the first system, H_2-mixture is used to heat the air passing through the shell. Fins are installed in the shell, to give the air a large surface area for heat transfer. The condensed water and H_2-mixture

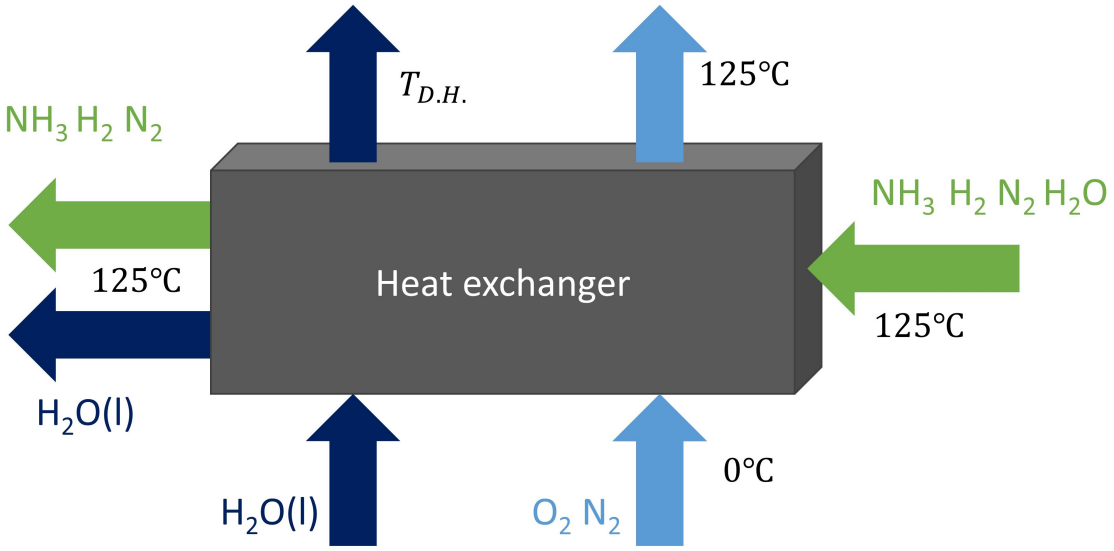

Figure 6.10: Basic schematic for the condensing heat exchanger

flows into the next system, where heat is transferred to water from the district heating, and the remaining water in the H_2-mixture condenses. The liquid water is then separated from the gas through gravity, and a vent leads the H_2-mixture out of the heat exchanger. With temperature sensors installed in and out of the heat exchanger, the water flow from the district heating can be controlled precisely so that only the heat from the condensing water is withdrawn from the H_2-mixture.

6.6 Heat exchanger for flue gas and combustion reactants

For the flue gas and combustion reactants heat exchanger, the main objective is to raise the temperature of the combustion reactants as much as possible before they enter the combustion chamber. The exhaust gas from the ammonia cracker is assumed to be at atmospheric pressure, and hold the same temperature as the working temperature of the decomposition reaction, 600°C. For the combustion reactants, H_2-mixture, and air-mixture, it is assumed they enter the heat exchanger at 2,2 bar and 125°C. The basic schematic for the heat exchanger is seen in figure 6.11.

For the heat exchanger using the ammonia cracker's flue gas to heat the incoming reactants, a counter-current cellular type recuperator design is selected. In a recuperator, the gases are held separate by walls made in a material with high thermal conductivity, often a metal or a ceramic. Heat is then transferred from the hot, exhaust gas to the ceramic wall, which passes it on to the cold gas. Both heat transfers are done by convection. A cellular type structure implies that the gases are led through a three-dimensional pathway on their way through the recuperator. Cellular type structures, coupled with a ceramic material's heat conducting properties, enables high efficient heat transfers in the range of 95-99% efficiency.[62]
It is assumed that the exhaust gas holds 125°C, as it leaves the recuperator, which implies that none of the water in the flue gas is condensed during the heat transfer.

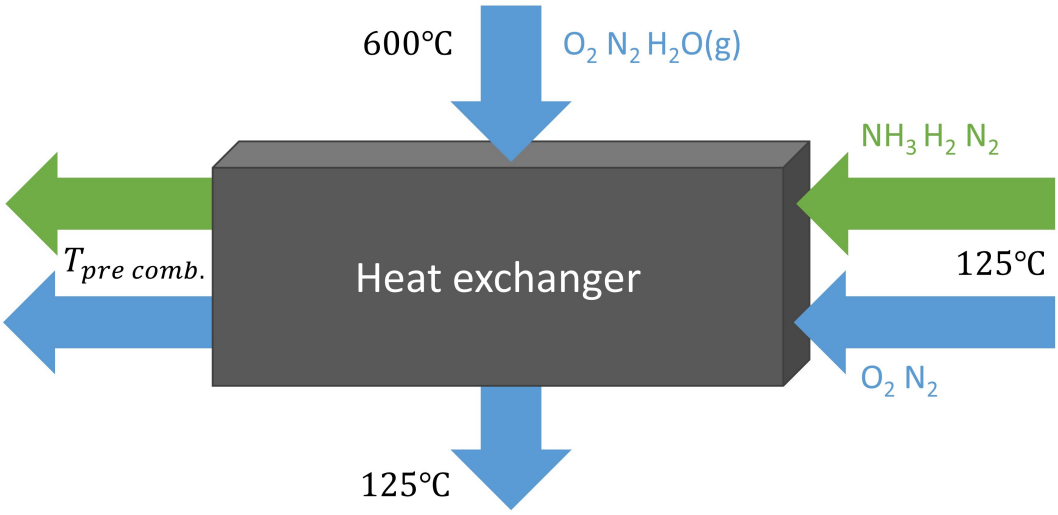

Figure 6.11: Basic schematic for the flue gas and combustion reactants heat exchanger

6.7 CO_2-scrubber

Most alkaline fuel cells use an alkali electrolyte dissolved in water, most commonly potassium hydroxide (KOH). An inconvenient feature of these electrolytes is that the presence of carbon dioxide in either fuel or oxygen streams, will cause the CO_2 to react with electrolyte and form crystals of potassium carbonate in the electrolyte solution. The reaction is stated in equation 6.7.

$$2\,KOH + CO_2 \longrightarrow K_2CO_3 + H_2O \tag{6.7}$$

The formation of crystals harms the AFC as it results in a series of adverse events, such as increasing electrolyte viscosity, decreasing in OH^- concentration in the electrolyte solution and blocking of electrode pores. These events result in a decreasing the conductivity of the electrolyte solution and interferes with the kinetics of the cell reactions, which leads to a severe deterioration in cell performance. The crystals have low solubility, making them hard to dissolve once formed. The maximum concentration of CO_2 allowed in an AFC is debated, Ahuja et al. sets the maximum concentration to be 10 ppm, while Dicks states that to avoid degradation of the AFC, the air must have a CO_2 concentration well below 50 ppm.[54][63]
This calls for the CO_2 being removed from the air stream before entering the AFC. In the fuel cell city car developed by Kordesch, solid absorbent soda lime was used as CO_2-scrubbing system, a system where the soda lime had to be replaced every time it was saturated with CO_2. When utilizing AFC's for power applications, the fuel cell needs to run for extended periods without intervention, and the required replacement frequency disqualify the use of soda lime for the Longyearbyen application.[64][65]
For the Longyearbyen application, a prototype of a continuous CO_2-scrubber developed by Krumdieck et al. is selected. Krumdieck et al. states AFCs to be one of the system's intended applications, and its schematic diagram is seen in figure 6.12.
In the prototype, the incoming air is injected at the base of a column called the absorber, which was packed with 15mm stainless steel Pall rings and filled with solutions of various monoethanolamine concentrations (MEA). The air is scrubbed for CO_2 by rising through the column, having to make its way around the submerged Pall rings which are designed

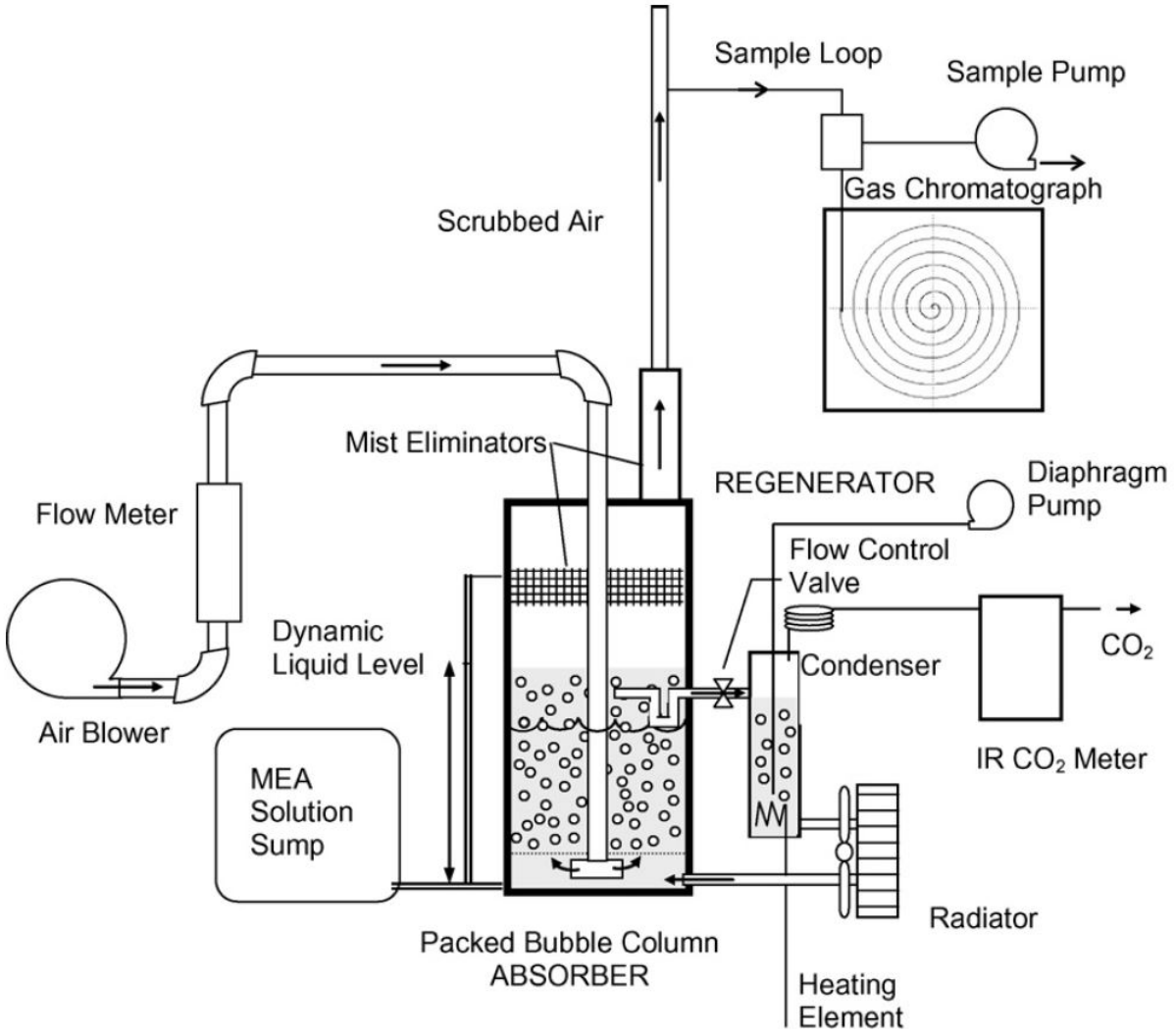

Figure 6.12: Schematic diagram of the continuous CO_2 scrubber prototype system used in experiments conducted by Krumdieck et al.[66]

to have a large surface area for the air bubbles to cling onto. The optimal composition for the MEA-solution proved to be 50wt% MEA, 35% glycol and 15% water, and is assumed to be applied in the Longyearbyen system.
The injected air results in the MEA-solution flowing up through the column, and as the regenerated MEA-solution enters from the bottom, saturated MEA-solution concentrates in the top of the column. The saturated MEA-solution exits the absorber through gravitational pull and enters at the top of a column known as the regenerator. In the regenerator, the CO_2 is released by raising the temperature of the MEA-solution to 120°C, and exits the system with together with a flush gas injected at the bottom of the column. For the Longyearbyen application, exhaust gas from the cathode is used as both flue gas and heating for the regenerator, as it holds 125°C. The regenerated MEA-solution then exits the regenerator, and in the Longyearbyen application, it is stored in an outdoor reservoir where it cools to ambient temperature.
The dimensions of the prototype scrubber by Krumdieck et al. are stated in table 6.2.

Parameter	**Value**
Absorber diameter	0,26 m
Height/diameter ratio	3
Air flow rate	20 m^3/h
CO_2 absorption efficiency	0,98

Table 6.2: Operational parameter values for absorber prototype developed by Krumdieck et al.[66]

The prototype was tested over one month of continuous scrubbing and is stated to have reached levels from less than 40 ppm to 60ppm, while other experiments with packed bubble columns conducted by Krumdieck and Wallace have shown that levels >10 ppm is possible. Therefore it is assumed that given 25 years of technical innovation, the scrubbing system for the Longyearbyen application can reach 10 ppm steadily, given a sufficient amount of solution and regeneration time.[64]

6.8 Electrolyte system

As stated in previous sections, the AFC's electrolyte is a circulating KOH-solution, which provides a conductive path for hydroxide-ions migrating through it. Additionally, the circulating electrolyte provides a very effective way of cooling the fuel cell, as the electrochemical reactions at the electrodes release heat which is transferred to the electrolyte.[57]
The electrolyte system used in the Longyearbyen application is modified from the fuel cell city car developed by Kordesch. In the system by Kordesch, heat is transferred to or from the air headed for the AFC, depending on stage of operation. For the Longyearbyen application, the heat provided by the AFC is transferred to the district heating by a heat exchanger. The electrolyte system schematic is seen in figure 6.13.
The electrolyte enters the AFC at near ambient temperature which is assumed to be 0°C, and leaves at the AFC's working temperature of 125°C. Heat collected by the electrolyte is then transferred to the district heating through a plate type heat exchanger, a design which is well suited for liquid to liquid heat transfer. The electrolyte, and its remaining heat, is led back to the electrolyte reservoir, which is situated outdoors where it spends enough time to cool down to ambient temperature. [67]

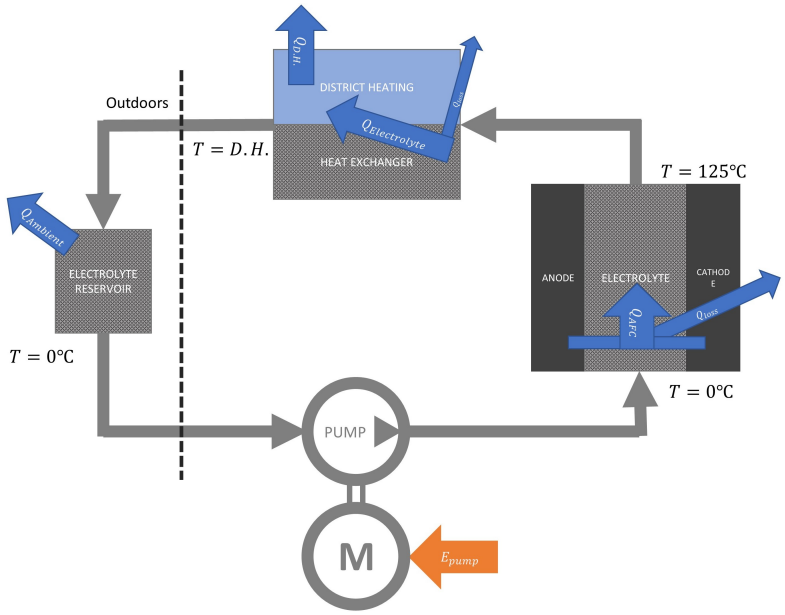

Figure 6.13: Electrolyte system schematic showing the mass- and energy flows

6.9 Power conditioner

The fuel cell emits a variable DC voltage, which needs to be conditioned to match the need of the specific application. As an example, data from a 250 kW PEM fuel cell system used in a bus is displayed in figure 6.14. During operation, the stack voltage varied from 400 V to 750 V, often displaying different voltage values at the same current.[68]
The fuel cell city car by Kordesch was co-powered by an 8 kWh lead-acid battery which offered quick response to sudden load changes. The DC power of the AFC and the battery was then inverted to AC power through an inverter, and fed to the electric motor.
For the energy produced by the AFC to be usable for the Longyearbyen settlement, it needs to be of good power quality. Meaning that the voltage, frequency and waveform must be within a prescribed range. As stated in section 1.2.2, the high-voltage electrical distribution system consists of an alternating current grid that operates on 11 and 22 kV, and 50 Hz.[69]
When the load from Longyearbyen changes, the AFC-system needs to adjust its chemical input to generate an electric power output accommodating the power need as quickly as possible. The time spent fulfilling the power need is called the systems response time, and the manner of accommodating it is called the systems transient or dynamic response. The doctor thesis of Helge Weydahl, investigates the dynamic behavior of AFCs fueled on pure H_2 and O_2, and indicates that the change transfer reaction at the cathode is the limiting response. Response times were dependent on initial and final cell voltages and varied on a time scale from 10 ms to 10 s.[70]
Since the AFC is fed with H_2 decomposed from ammonia, the dynamic response of the system is heavily dependent on the thermal decomposition of the ammonia cracker. Both Kordesch and Chellappa et al. states that the dynamic behavior and transient response of an ammonia cracker needs to be investigated. The only data found on the dynamic behavior of an ammonia cracker is the measured temperature distribution during start-up, seen in figure 6.15. The plot shows that an automotive size ammonia cracker reaches stable operating temperatures after 30 minutes of operation. Depending on the magni-

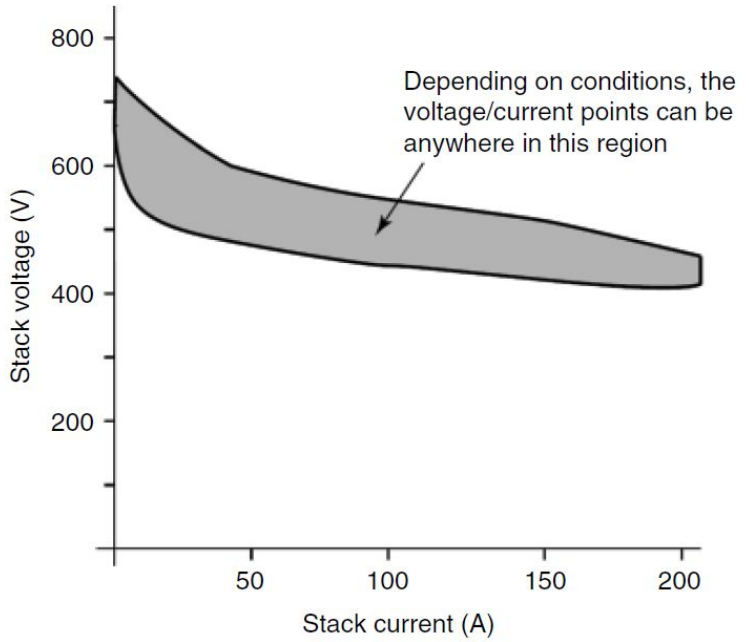

Figure 6.14: Data showing variations in voltage and current for a 250 kW fuel cell system.[68]

tude of the load change, a response time in the scale of several minutes is regarded as plausible.[71][72][73]
Therefore it is decided that a fuel storage tank is installed, to supply the AFC with fuel during the ammonia cracker's time of response. The basic schematic of the power conditioning system is seen in figure 6.16.
To avoid power flowing into the AFC, a diode is installed between the AFC and the boost converter. The boost converter ramps up the DC-voltage, for the battery bank to be supplied with high-quality DC power as prescribed. The battery bank and the boost converter is connected through a DC-bus, and another diode is connected between the boost converter and the DC-bus, to ensure the current being unidirectional where needed. The DC-bus is also connected to the inverter, where the DC power is converted to AC power, through a technique called pulse width modulation. Pulse width modulation is performed by switching the voltage on and off very rapidly, but in intervals that get longer and shorter and in this manner the average voltage mimics the sinusoidal curve of an alternating voltage. The AC side of the inverter is connected to the AC-bus which is the system's electric boundary, as it is connected to the power grid.[74]
Due to the complexity of the AFC's energy conversion, control strategies need to be implemented and fine-tuned for aspects such as compressor-, pump- and fan motor control, the AFC and ammonia crackers operating pressure and temperature, combustion ratios and humidity of the air entering the system.

6.10 Pumps, compressors and fans

Pumps

The pumps are labeled from 1 to 3, where pump 1 moves liquid ammonia into the system, pump 2 circulates the MEA-solution in the CO_2-scrubbing system and pump 3 circulates

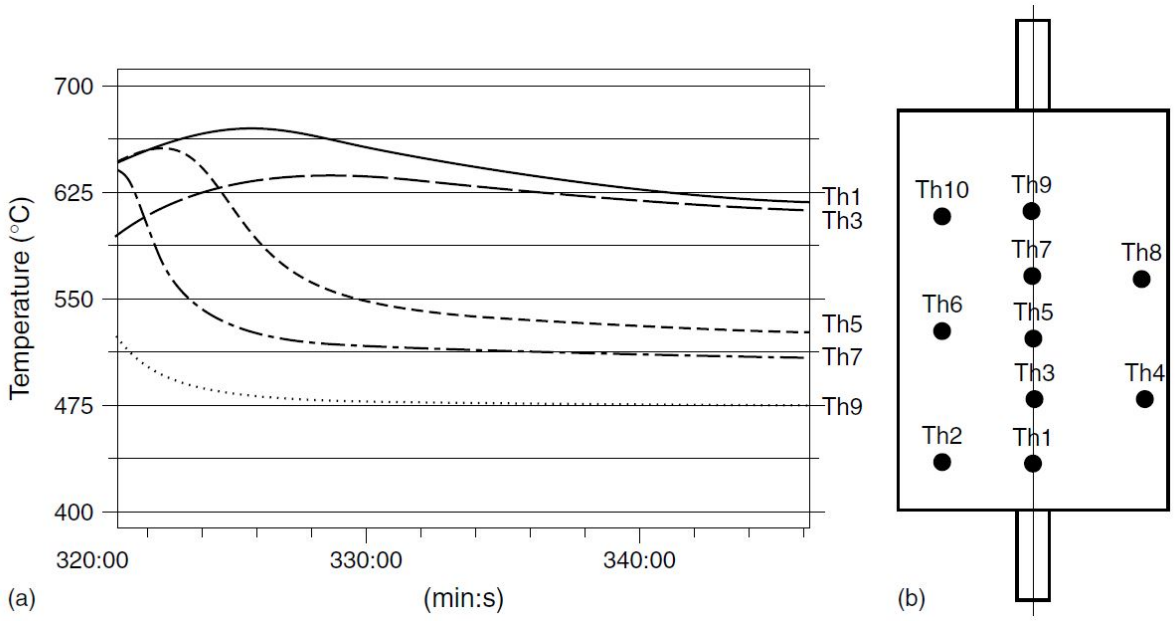

Figure 6.15: To the left is the measured temperature distribution during start-up inside a plate type ammonia cracker, and to the right is the thermal sensors positioning inside the cracker.[73]

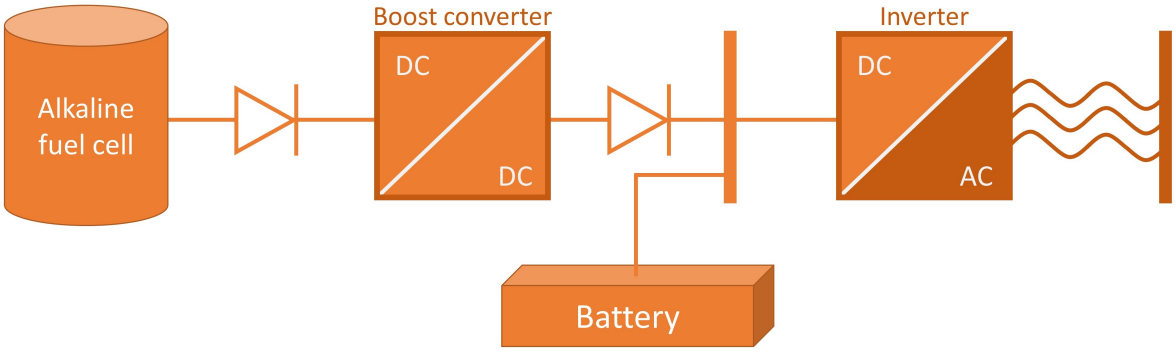

Figure 6.16: Schematic of power conditioning system for the AFC.

the electrolyte KOH-solution through the AFC. All pumps operate under similar working conditions, low pressure increase and low volume flows. On this basis, it is determined that all pumps are variable axial piston pumps, as seen on the schematic of figure 6.17. The benefit of the axial piston pump is that the swash plate can be tilted which adjusts the stroke of the pistons. This enables easy adjustment of volume flow, which relates to power control. The material selection must be adapted for each pump, for it to withstand corrosion from the various working mediums.[75]

Compressors

The compressors labeled 1 and 2 are set to raise the pressure of the H_2-mixture stream in and out of the AFC to 2,2 bar. Under standard operating conditions, the pressure raise supplied by the compressors are the pressure drop of the ammonia cracker and the AFC, which is likely to be many times smaller than from atmospheric pressure to 2,2 bar. So under normal working conditions the compressors applies a low pressure increase to a

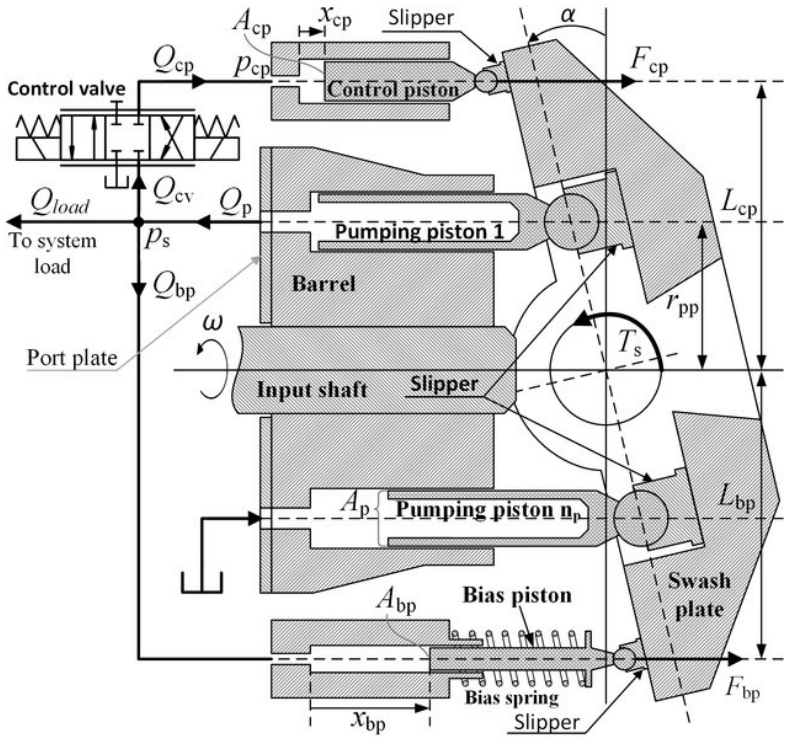

Figure 6.17: Schematic of a variable axial piston pump[76]

large gas flow.
For applications with low pressure raise and high volume flow, centrifugal compressors are selected, and their composition is illustrated in figure 6.18. Centrifugal compressors have a high throughput with a moderate compression ratio. The gas is drawn in at the center of the impeller, and forced outward at high speed to the surrounding solute, in this way the kinetic energy is converted into a pressure increase.[77]

Compressor 3 and 4 raises the pressure of the air going out and in of the AFC respectively. On the way in, the compressor needs to raise the pressure from near ambient pressure to 2,2 bar, while on the way out pressure is raised equal to pressure drop in the fuel cell. Both compressor moves large volume streams of air, and compressor number 4 additionally moves the water produced in the AFC.
For the air-mixture compression, centrifugal compressors are selected, as they have the operate under pretty much the same working conditions as compressor 1 and 2.

The compressor labeled as number 5 compresses H_2-mixture for short time storage. For a scenario where the storage is almost full, the compressor needs to raise gas pressure from 2,2 to 100 bar. The compressor then works with a small volume flow and a high pressure increase.
For the fuel gas storage, a diaphragm compressor is selected, and its composition is seen in figure 6.18. The diaphragm compressor is commonly preferred for high-pressure hydrogen applications because of it being extremely low leaking, which is essential when working with highly explosive gases as hydrogen. The H_2-mixture is compressed by using a flexible membrane, the diaphragm, which is moved back and forth by a piston and a crankshaft mechanism. During compression, the gas is only the membrane and the compressor walls

is in contact with the gas, reducing the risk of spontaneous combustion due to friction immensely.[78]

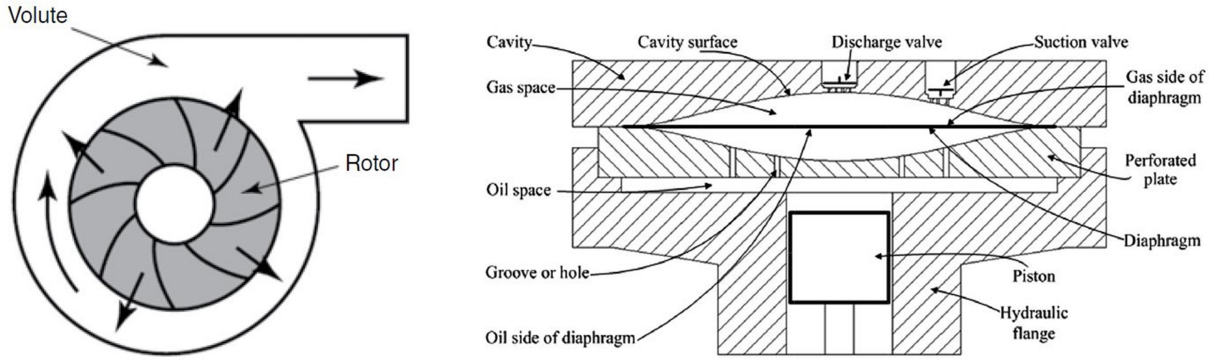

Figure 6.18: Compressor types used in the system. To the left is the centrifugal compressor, and to the right is the diaphragm compressor.[77][78]

Fans

There is only one fan in the system, and it is moving air into the absorber of the CO_2-scrubber. The selected design is a centrifugal fan with vanes that are bent backward. Air flows into the fans axial center and is pressed outwards by the centrifugal forces. Through this operating principle, the centrifugal fan can move large air flows at efficiencies up to 85%. [79]

7. Mass balances

As a basis for the mass balance system calculations, the results from an energy modeling study done by Ringkjøb et al. are put forward. In a scenario where Longyearbyen is supplied by hydrogen from mainland Norway, the study concludes with the energy needed from hydrogen to be *89 GWh and 60 GWh in 2030 and 2050 respectively.* These values averages over a large number of simulations, and are regarded as the best estimate to date.[19] The system is assumed to be operating strictly during winter, and the number of operating days is set to 183.

7.1 Ammonia storage

With the supplied hydrogen being stated as energy, it is assumed that the mass of the supplied hydrogen can be calculated by using the lower heating value. The mass of hydrogen is calculated through the use of equation 7.1.

$$m_{\mathrm{H_2}} = \frac{E_{\mathrm{H_2}}}{LHV_{\mathrm{H_2}}} \tag{7.1}$$

Where $m_{\mathrm{H_2}}$ is the mass of the hydrogen, $E_{\mathrm{H_2}}$ is the energy of the imported hydrogen and $LHV_{\mathrm{H_2}}$ is hydrogen's lower heating value, which is $120 MJ/kg$. When hydrogen is bound to ammonia, hydrogen constitute of 17,75 wt.%, and the amount of needed for import ammonia is described by 7.2.

$$m_{\mathrm{NH_3}} = \frac{m_{\mathrm{H_2}}}{0,1775} \tag{7.2}$$

The calculated masses of hydrogen and ammonia, the volume of the ammonia at liquid state, and the needed storage volume is presented in table 7.1. The maximum filling ratio for the storage is set to 95%.[80]

	2030	**2050**
$\dot{m}_{\mathrm{H_2}}$	2670 $\frac{tonnes}{year}$	1800 $\frac{tonnes}{year}$
$\dot{m}_{\mathrm{NH_3}}$	15037,3 $\frac{tonnes}{year}$	10137,5 $\frac{tonnes}{year}$
$\dot{V}_{\mathrm{NH_3}}$	22055,3 $\frac{m^3}{year}$	14868,7 $\frac{m^3}{year}$
$V_{\text{needed for storage}}$	23216,1 m^3	15651,3 m^3

Table 7.1: Masses of the imported hydrogen and ammonia in 2030 and 2050, along with the volume of the ammonia at liquid state and the needed storage volumes.

As an example, if a 25000 m^3 cylindrical tank is selected for storing the ammonia, this would result in a tank which is roughly 40 meters in diameter and 20 meters tall.

7.2 Vaporizing heat exchanger

The vaporizing heat exchanger utilize heat from the decomposed ammonia stream to gasify and pre-heat the liquid ammonia, before entering the ammonia cracker. The mass flows running through the heat exchanger is visualized in figure 7.1.

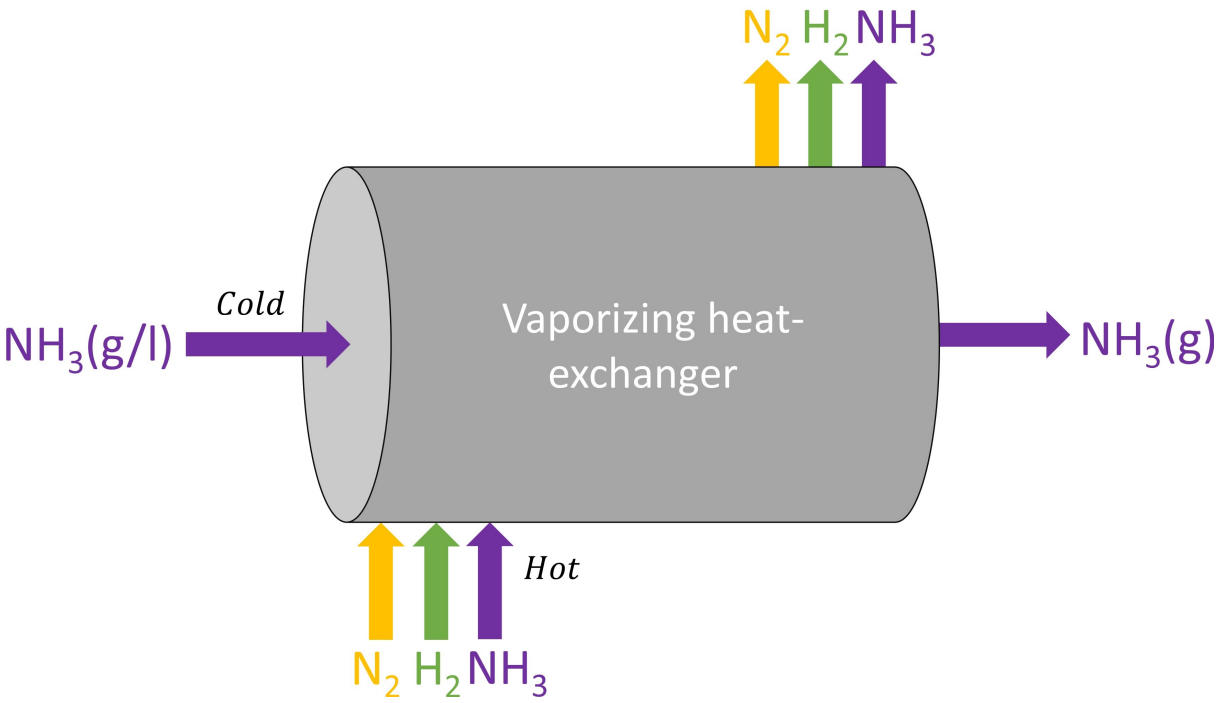

Figure 7.1: Mass flow diagram for vaporizing heat exchanger

Assuming no mass is lost or converted through the heat exchanger, mass flows are listed in table 7.7.

Side	**Component**	**2030** ($\frac{tonnes}{year}$)	**2050** ($\frac{tonnes}{year}$)
Cold	NH_3	15037,3	10137,5
Hot	N_2	12345,2	8322,6
	H_2	2664,7	1796,4
	NH_3	30,1	20,3

Table 7.2: Mass flow through the vaporizing heat exchanger

7.3 Ammonia cracker

For the ammonia cracker to run smoothly, it relies on balancing of two chemical reactions, an endothermic reaction and a combustion reaction.

7.3.1 Endothermic reaction

The ammonia decomposition reaction was described in equation 6.1, and is re-stated in equation 7.3.

$$NH_3 + 46\,\frac{\text{kJ}}{\text{mol}\,NH_3} \longrightarrow \frac{1}{2}\,N_2 + \frac{3}{2}\,H_2 \tag{7.3}$$

The reaction states that for one mole of NH_3 that reacts, a half a mole of N_2 and one and a half mole of H_2 is produced. Based on the catalyst data, it is assumed that the ammonia cracker has a conversion rate of 99,8%. The mass balance is visualized through figure7.3.

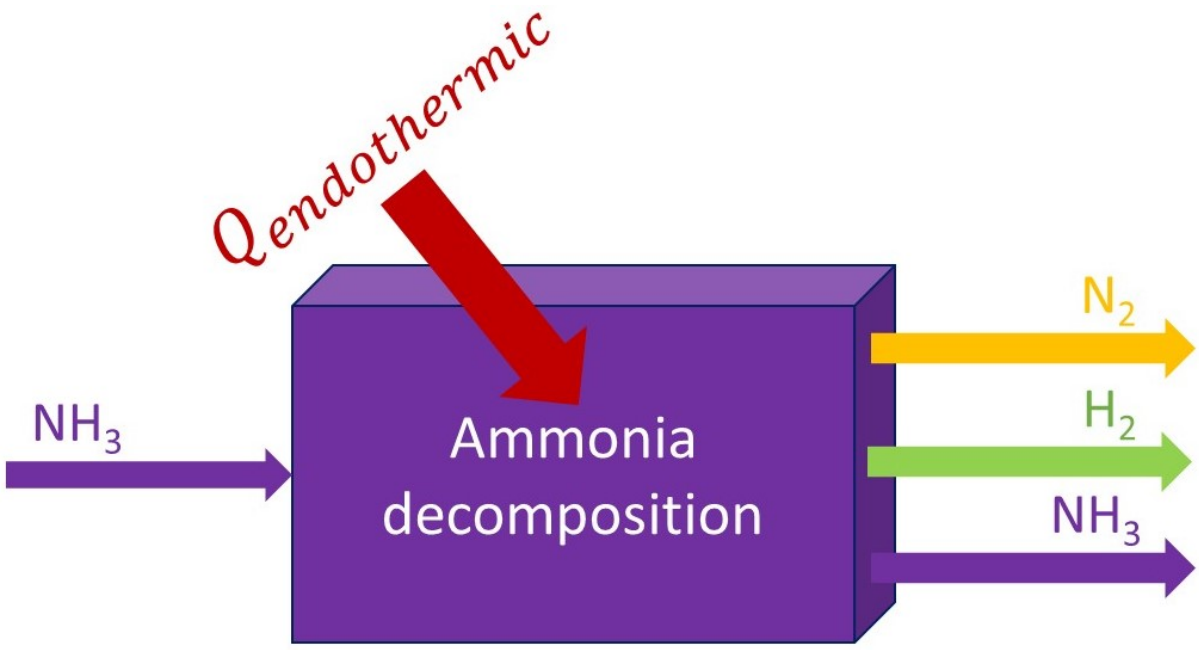

Figure 7.2: Schematic for the mass balance through the ammonia cracker for the ammonia decomposition process.

The calculated mass flows of the endothermic reaction is presented in table 7.3.

	Substance	**2030** $(\frac{tonnes}{year})$	**2050** $(\frac{tonnes}{year})$
In	NH_{3in}	15037,3	10137,5
Out	N_2	12345,2	8322,6
	H_2	2664,7	1796,4
	NH_{3out}	30,1	20,3

Table 7.3: Mass balance for the endothermic reaction in the ammonia cracker.

7.3.2 Combustion reaction

A chemical reaction where a fuel is rapidly oxidized and energy is released is called combustion. The exhaust gases from the fuel cell are used as fuel, and combusted to provide heat for the ammonia cracker. A visualization of the mass balance for the combustion reaction is given in figure 7.3.

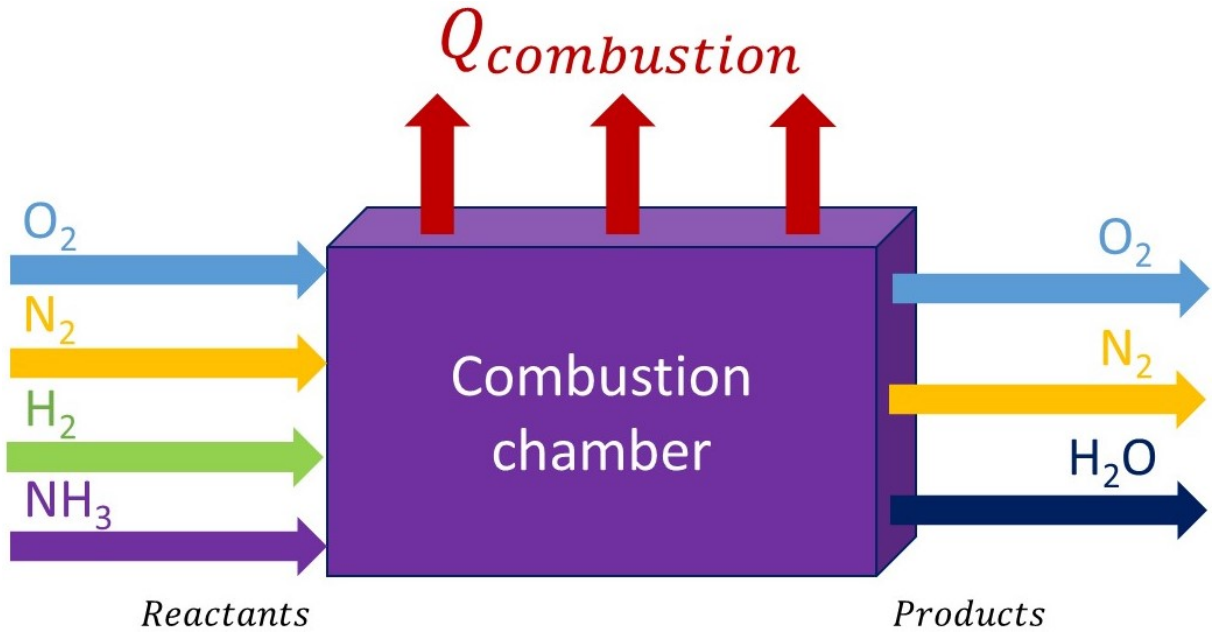

Figure 7.3: Mass balance through the ammonia cracker for exhaust gas combustion.

The combustion reaction is simplified by assuming that the combusting reactants undergo a complete combustion, resulting in N_2 and H_2O as products. Its also assumed that the rest of the substances present does not interfere with the reaction, described by the flow charts of figure 7.4. Since the air used for combustion is the exhaust air of the fuel cell, it contains half the oxygen compared to ambient air. This makes the air's N_2/O_2-ratio 7,52, and the basis for the balancing of the combustion reaction is given in equation 7.4.

$$0{,}0084\,NH_3 + 0{,}9916\,H_2 + a \cdot O_2 + a \cdot 7{,}52 \cdot N_2 \longrightarrow b \cdot N_2 + c \cdot H_2O \tag{7.4}$$

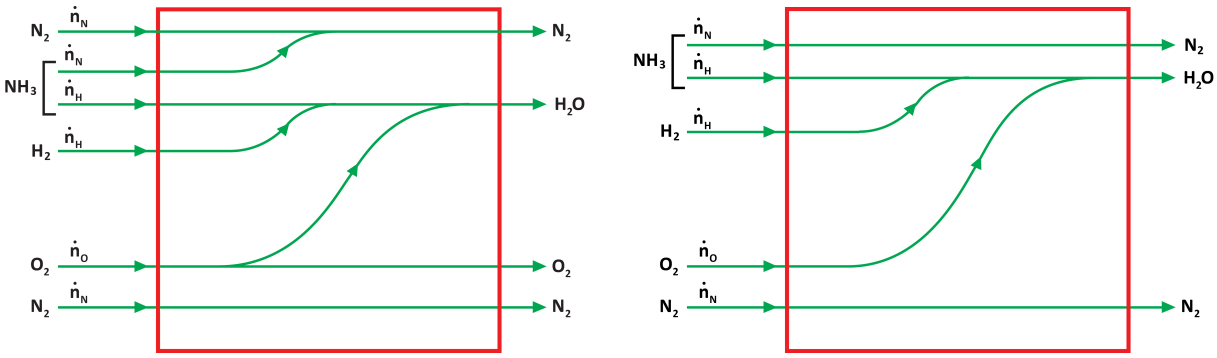

(a) All reactants and products

(b) Simplified complete combustion reaction

Figure 7.4: Total combustion reaction and simplified complete reaction flow chart for the combustion reaction

The combustion reaction is balanced by attaining equilibrium of each chemical element in the equation. There are three elements to balance, hydrogen, oxygen and nitrogen.

H-balance

$$\begin{aligned} 3 * 0,0084 + 2 * 0,9916 &= c * 2 \\ 2,0084 &= c * 2 \\ c &= 1,0041 \end{aligned} \tag{7.5}$$

O-Balance

$$\begin{aligned} a * 2 &= c * 1 \\ a &= \frac{1 * 1,0042}{2} \\ a &= 0,5020 \end{aligned} \tag{7.6}$$

N-Balance

$$\begin{aligned} 0,0084 + a * 7,52 * 2 &= b * 1 * 2 \\ \frac{0,0084 + 0,5021 * 7,52 * 2}{1 * 2} &= b \\ b &= 3,7758 \end{aligned} \tag{7.7}$$

The values calculated from equation 7.5, 7.6 and 7.7 are plugged into 7.4, and the balanced combustion reaction is presented in 7.8.

$$0{,}0082\,NH_3 + 0{,}9918\,H_2 + 0{,}5020 \cdot O_2 + 3{,}7758 \cdot N_2 \longrightarrow 3{,}7799 \cdot N_2 + 1{,}0041 \cdot H_2O \tag{7.8}$$

The balanced combustion reaction of equation 7.8 is used to calculate the molar flow of the reactants and the products. The amount of air-mixture, O_2 and N_2, is called the theoretical or stoichiometric air, and represents the minimum amount of air needed for a complete combustion to occur. To increase the chances of a complete combustion in an actual combustion process, it is common practice to use more air than theoretically needed. The added air is known as excess air, and for the ammonia cracker an *excess air ratio of 1,1* is selected. This implies that 10% more air than theoretically needed, is let into the combustion chamber. As a result, some uncombusted O_2 exits the combustion chamber, along with excess N_2 and the other products. The total mass balance of the combustion reaction is presented in table 7.4. [81]

	Substance	**2030** ($\frac{tonnes}{year}$)	**2050** ($\frac{tonnes}{year}$)
In	O_{2in}	3815,2	2572,1
	N_2	25124,8	16938,1
	H_2	431,6	291,0
	NH_3	30,1	20,3
Out	O_{2out}	346,8	233,8
	N_2	25124,8	16938,1
	H_2O	3905,4	2632,8

Table 7.4: Mass balance for the endothermic reaction in the ammonia cracker.

Notice that the inputted O_2 and N_2 is many magnitudes smaller than the amount leaving the fuel cell. This is due to the amount of air-mixture not needed by the combustion

reaction leaves the system through a flow divider. The magnitude of the flow leaving could be adjusted through regulating the pressure of the exiting flow. By guiding part of the air-mixture out of the system, the total system efficiency is increased due to energy savings in heat exchanging and combustion. Instead, the excess air-mixture will contribute to the district heating.

7.3.3 Summary

The ammonia cracker is a system combined with two chemical reactions, an endotherm reaction which decomposes ammonia and a combustion reaction which provides heat for the endotherm reaction.
In 2030, 15 037 tonnes of NH_3 decompose at a conversion rate of 99,8% to 2664,7 tonnes of H_2. To maintain the catalyst working temperature, 431,6 tonnes H_2 is combusted along with 30,1 tonnes of NH_3.

7.4 Alkaline fuel cell

The mass balance of the fuel cell is based on the total reaction of the fuel cell, presented in equation 7.9. The chemical reaction states that for every mole of H_2 which reacts with half a mole of O_2, a mole of gaseous H_2O is produced.

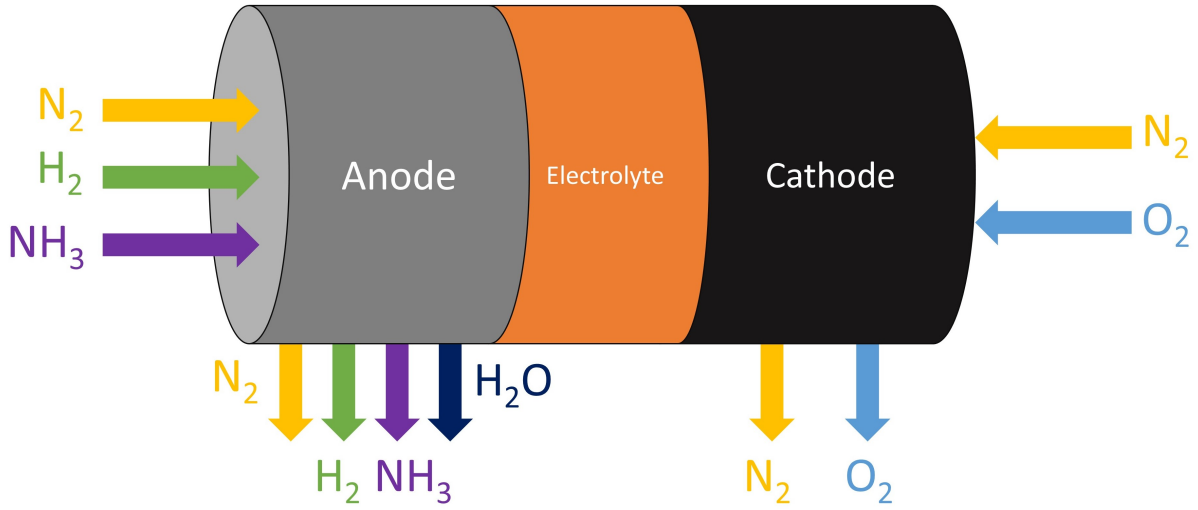

Figure 7.5: Caption

$$H_2 + \frac{1}{2} O_2 \longrightarrow H_2O \tag{7.9}$$

In practical applications, some of the input H_2 passes unreacted through the fuel cell, even when the fuel cell is fed solely. The fuel utilization coefficient expresses the ratio of the reacted fuel versus the total amount of fuel passing through the fuel cell, and is expressed in equation. For the AFC, the H_2 is part of a fuel mixture, which lowers the anode's reaction rate. The fuel utilization coefficient is set to 0,842, as the H_2 which is unreacted in the fuel cells are combusted to cover the heating demands of the ammonia

cracker. 7.10.[82]

$$\mu_f = \frac{\text{Mass of fuel reacted in fuel cell}}{\text{Mass of fuel input to fuel cell}} \tag{7.10}$$

The amount of H_2 which reacts in the fuel cell, is calculated through equation 7.11, and is used to calculate the amount of O_2 consumed and H_2O produced by the reaction through equation 7.9.

$$\mathrm{H_{2Reacted}} = \mu_f \cdot \mathrm{H_{2Input}} \tag{7.11}$$

With air being used instead of pure oxygen, N_2-molecules present in the air tends to block the O_2-molecules access to the pores in the cathode. This phenomenon was referred to as clogging in section 6.4.6. To ensure the cathode, and the ammonia cracker, being supplied with sufficient O_2, the pressure of the incoming air is set to 2,2 bar, and an excess air ratio of 2 is selected for the AFC. Traces of argon and other substances in the air are neglected.
The mass balance for the AFC is split for the anode- and cathode side of the fuel cell, and is presented in table 7.5.

Anode	**Component**	**2030** ($\frac{tonnes}{year}$)	**2050** ($\frac{tonnes}{year}$)
In	H_2	2664,7	1796,4
	N_2	12345,2	8322,6
	NH_3	30,1	20,3
Out	H_2	431,6	291,0
	N_2	12345,2	8322,6
	NH_3	30,1	20,3
	H_{20}(g)	19955,1	13452,9

Cathode	**Component**	**2030** ($\frac{tonnes}{year}$)	**2050** ($\frac{tonnes}{year}$)
In	O_2	35444,2	23895,0
	N_2	116708,1	78679,6
Out	O_2	17722,1	11947,5
	N_2	116708,1	78679,6

Table 7.5: Mass balance for the alkaline fuel cell.

7.5 Condensing heat exchanger for H_2O and air

The mass flows through the heat exchanger, which pre-heats the air entering the fuel cell, is visualized in figure 7.7.
It is assumed that all the water vapor of the H_2-mixture is condensed in the heat exchanger, assuming water is separated from the gas mixture and exiting the heat exchanger in liquid form. The amount of water district heating water passing through the heat exchanger depends on the set working temperature of the district heating, and is therfore not stated. Furthermore, it is assumed that no mass is lost or converted in the heat exchanger, mass flows are given in table 7.6.

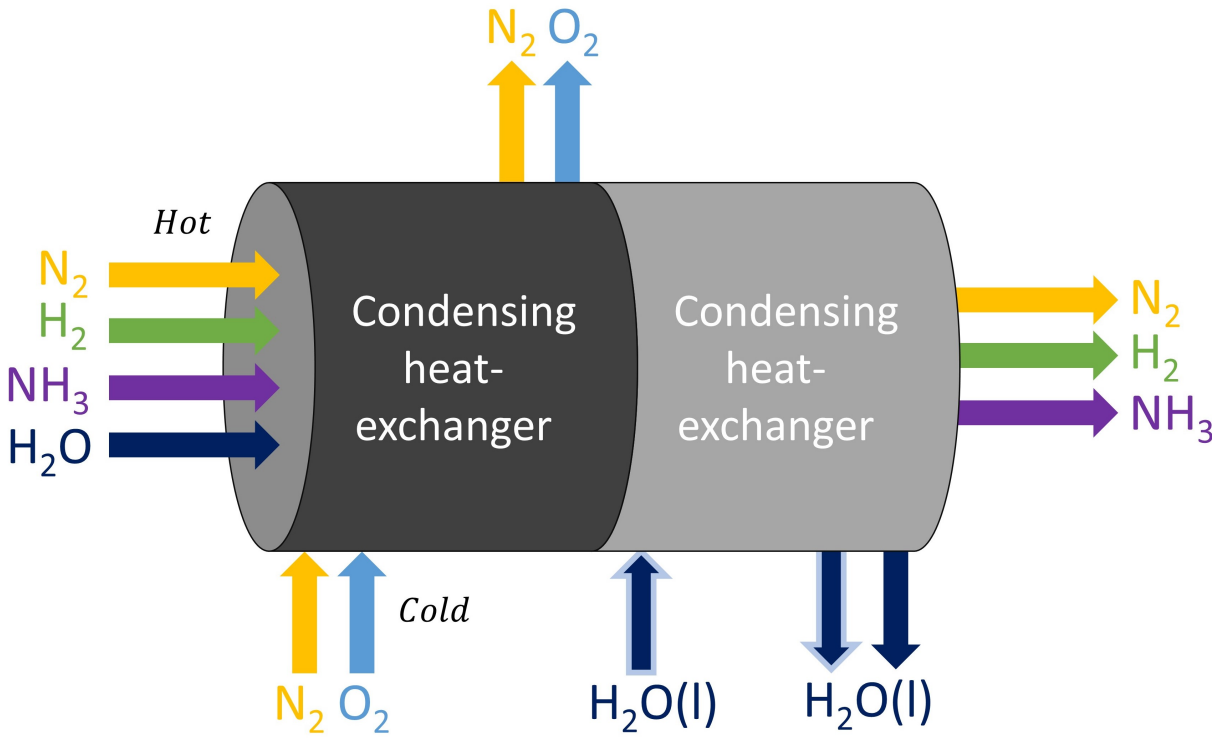

Figure 7.6: Mass flow diagram for condensing heat exchanger

Side	Component	2030 ($\frac{tonnes}{year}$)	2050 ($\frac{tonnes}{year}$)
Cold 1	N_2	116708,1	78679,6
	O_2	35444,2	23895,0
	CO_2	94,0	63,4
Cold 2	H_2O	-	-
Hot	N_2	12345,2	8322,6
	H_2	431,6	291,0
	NH_3	30,1	20,3
	H_2O	19955,1	13452,9

Table 7.6: Mass flow through the condensing heat exchanger

7.6 Heat exchanger for exhaust gas and combustion reactants

The mass flows through the heat exchanger, which pre-heats the reactants before entering the combustion chamber in the ammonia cracker, is visualized in figure 7.7.

As seen on figure 7.7, surplus air leaves the system through a flow splitter before entering the heat exchanger. This is a measure to avoid heating up more air than necessary, which would lead to efficiency loss for both the heat exchanger and the system as a whole. Assuming no mass is lost or converted through the heat exchanger, all mass flows are given in table 7.7.

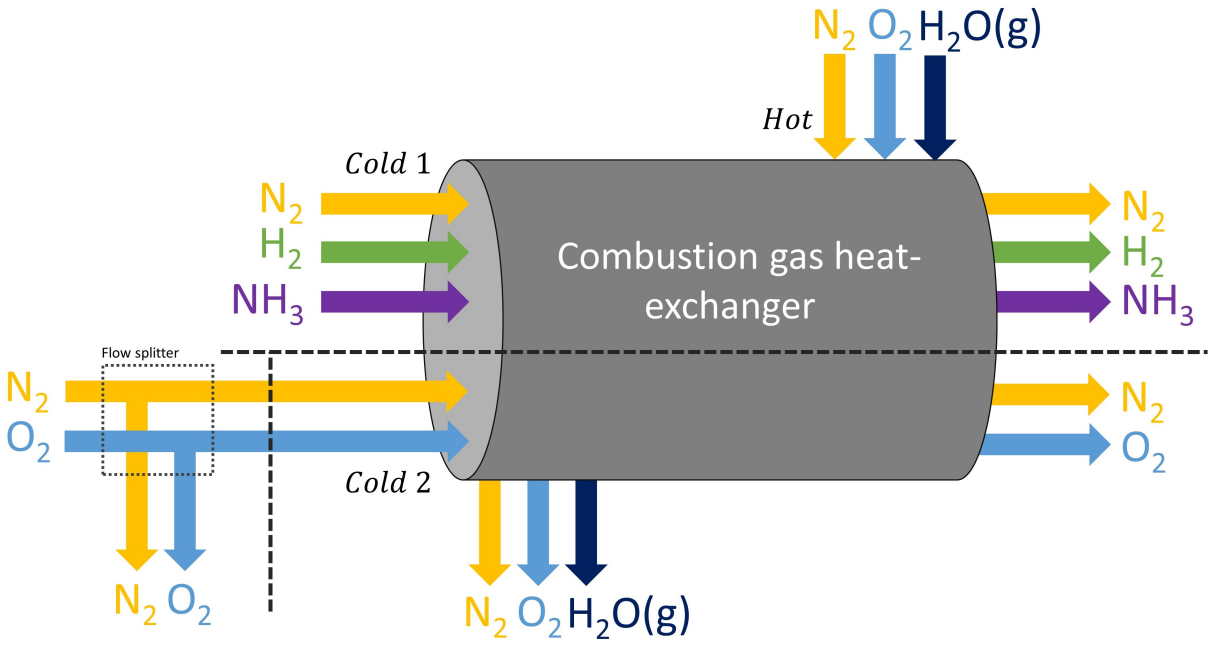

Figure 7.7: Mass flow diagram for exhaust gas and combustion reactant heat exchanger. Also showing the surplus air leaving the system.

Side	Component	2030 ($\frac{tonnes}{year}$)	2050 ($\frac{tonnes}{year}$)
Exiting valve	N_2	91583,2	61741,5
	O_2	13906,9	9375,4
Cold 1	H_2	431,7	291,0
	N_2	12345,2	8322,6
	NH_3	30,1	20,3
Cold 2	N_2	25124,9	16938,1
	O_2	3815,2	2572,1
Hot	N_2	25149,6	16954,8
	O_2	346,8	233,8
	H_2O (g)	3905,4	2632,8

Table 7.7: Mass flow through the exhaust gas heat exchanger

7.7 CO_2-scrubber

As stated in 6.7, the design of the CO_2-scrubber is an upscaled version of the continuous scrubber prototype by Krumdieck et al. The mass and energy flow is seen in figure 7.8. It is assumed that a scale-up of linear proportions is possible, making the Longyearbyen installation 1448 times greater than the prototype based on incoming air-flow.

The CO_2-scrubber is split into three mass-flow systems, ambient airflow through the absorber, MEA-solution circulation the through absorber, regenerator and reservoir, and the ammonia crackers surplus air, consisting of O_2 and N_2, passing through the regenerator. Over the following subsections, the mass balance for all systems is accounted for, and the volume of the absorber, regenerator and reservoir is estimated.

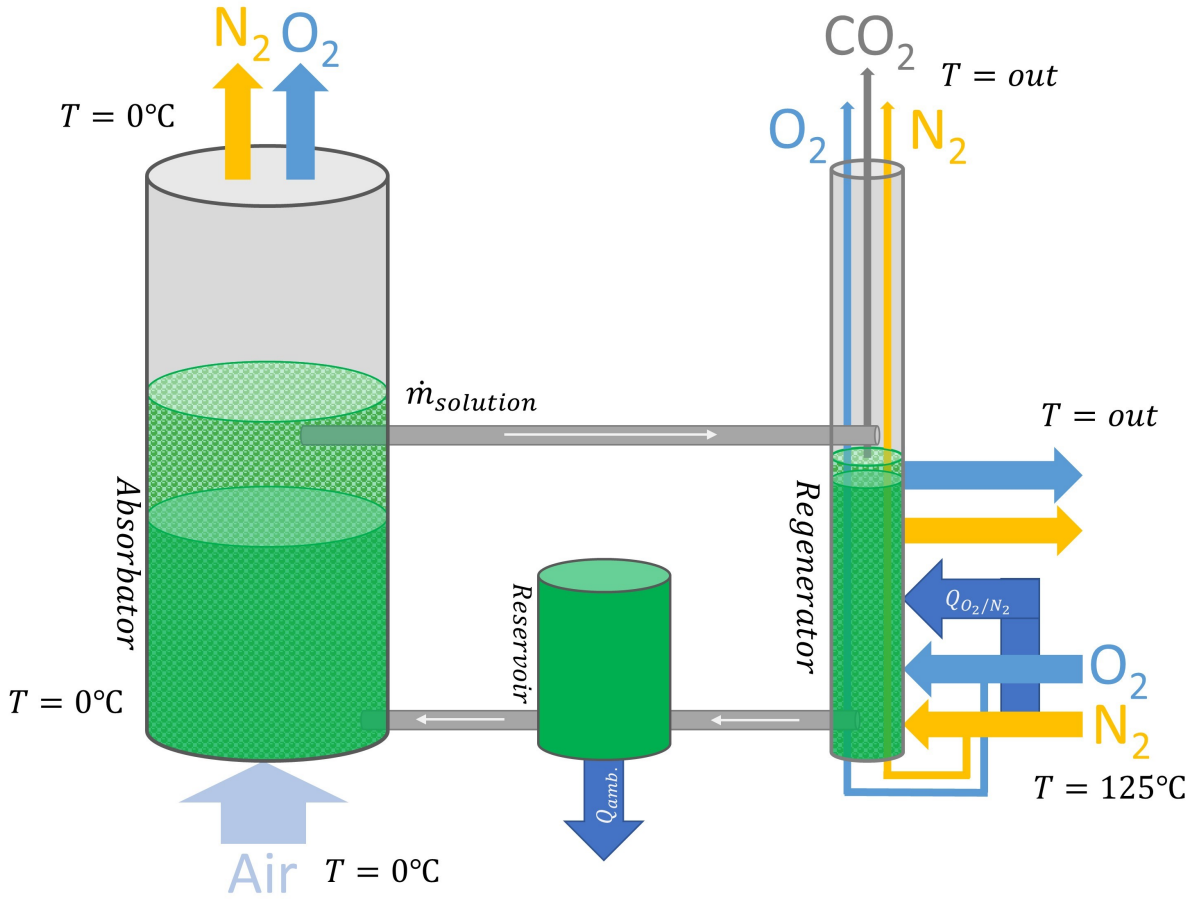

Figure 7.8: Mass and energy flow through the CO_2-scrubbing system

Absorber air flow

The volumetric concentration of CO_2 in the air, is assumed to be 413 ppm. The absorber is assumed to have an absorption efficiency of 0,98, corresponding with the prototype of Krumdieck et al. With these assumptions, the air exiting the absorber has a CO_2 concentration of 8,26 ppm, which is satisfying to the set demand of 10 ppm. From this point, the CO_2 in the air is disregarded, and the air stream is assumed to consist of O_2 and N_2 solely. The mass balance for the absorber is presented in table 7.8.

Absorber	**Component**	**2030** $(\frac{tonnes}{year})$	**2050** $(\frac{tonnes}{year})$
In	O_2	35444,2	23895,0
	N_2	116708,1	78679,6
	CO_2	94,0	64,4
Out	O_2	35444,2	23895,0
	N_2	116708,1	78679,6
	CO_2	1,88	1,27
	CO_2 absorbed	92,1	62,1

Table 7.8: Mass balance for the absorber

Solution

The solution is split over three components, the absorber, the regenerator and the reservoir, and the needs to be calculated separately for each component. The selected MEA-solution has a composition of 50wt% MEA, 35% glycol and 15% water.

Absorber
Given the up-scale ratio of 1448, and the prototype parameters from table 6.2, the absorber dimensions and the mass of the solution needed given in table 7.9. The air flow for 2030 is set as dimensioning criteria for the absorber's diameter and height.

Parameter	Value
Air flow rate (2030)	8,04 m^3/s
Absorber diameter	3 m
Absorber height	9
Solution volume	23,06 m^3
Solution height	3,26 m
Solution weight	24,11 tonnes

Table 7.9: Operational parameter values and mass flow for the absorber

The absorber needs to be filled with *24,11 tonnes of MEA-solution* to absorb the desired amount of CO_2 from the incoming air.

Regenerator
For continuous scrubbing, the rate of CO_2 removed from the regenerator must be the same as the rate of CO_2 scrubbed from the air stream. This makes the solution flow through the regenerator the primary system control parameter, to achieve desired scrubbing performance. By describing the CO_2 mole balance, Krumdieck et al. stated the needed solution flow rate for the prototype, $\dot{V}_{solution}$, as given in equation 7.12.[66]

$$\dot{V}_{solution} = 2 * \frac{\eta_A}{\eta_R} * \frac{\dot{n}_{CO_2}}{\alpha * f_{\text{MEA}}} * \frac{M_{\text{solution}}}{\rho_{\text{solution}}} \tag{7.12}$$

Where η_A and η_R are the efficiencies of the absorber and regenerator, which is 0,98 for the absorber and 0,6 for the regenerator. The mole rate of CO_2 entering the absorber is represented by $\dot{n}_{CO_2}$. α is the molar CO_2-loading of the solution, the ratio of moles of CO_2 per mole of MEA. Due to lacking data for the selected solution composition, data provided by Kim et al. for a 30wt% MEA-solution, operating at 40°C, is assumed to be sufficient. The CO_2-loading of the solution, α, is assumed to be 0,469. f_{MEA} is the mole fraction of MEA in the solution, which is 0,555, M_{solution} and ρ_{solution} is the solution molecular weight and density, respectively.[83]
The volume flow of the solution is calculated to be *0,32 m^3/h* in 2030 and *0,22 m^3/h* in 2050. Kim et al. states that the time needed for the solution to reach the desired regeneration state is 200 min.
Table 7.10 states the calculated mass of solution along with the dimensions of the regenerator, based on the solution's circulation time.
Reservoir
It is assumed that if given sufficient throughput time, the solution will cool so the solution leaving the reservoir is at ambient temperature. This means that the rate of heat leaving

Parameter	Value
Regenerator diameter	0,7 m
Regenerator height	
Solution flow rate	0,32 m^3/h
Solution height	2,78 m
Solution weight	1,12 tonnes

Table 7.10: Operational parameter values and mass flow for the regenerator

the reservoir equals the rate of the heat entering from the regenerator. To ensure sufficient throughput time, it is decided that during operation the reservoir will hold a mass of MEA equal to the mass present in the absorber and regenerator. This results in a throughput time of 75 hours, with *the reservoir holding 25,2 tonnes of MEA-solution.*
To maximize the heat flow rate through the reservoir walls, it is essential to maximize the reservoirs surface area. In figure 7.9, the surface area, solution height, and reservoir height of a cylindrical shaped reservoir is plotted for diameters from 1 to 8 meters. The reservoir is assumed to have a maximum fill level of 95%, which leads to a reservoir volume of 50,8 m^3.

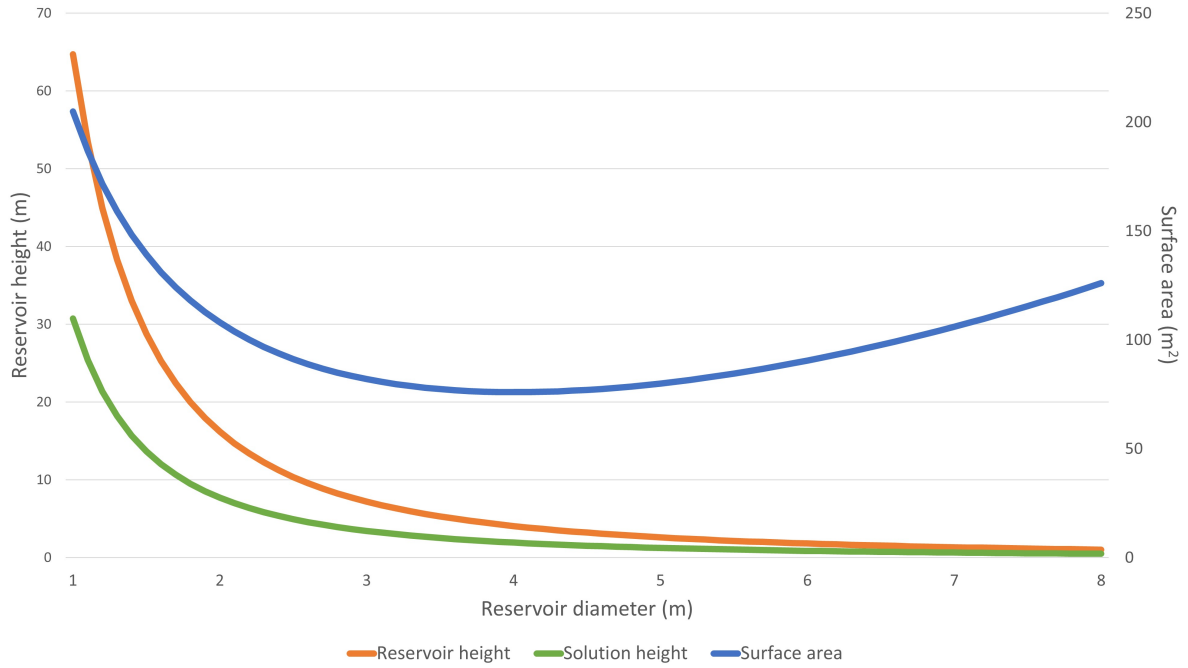

Figure 7.9: Height and surface area plotted as functions of diameter for a cylindrical reservoir

From figure 7.9, it is evident that the diameter range from 3 to 5 meters gives the least surface output. A lower diameter calls for a higher surface area, but to reach surface area of 100 m^2 or greater, the solution height needs is 7 meters or higher, which causes the reservoir to hold a higher pressure than the rest of the system.
For diameters over 5 meters, the surface area rises and reach 100 m^2 at a diameter of 7 meters. The reservoir height is calculated to be 1,3 meters, where the solution height during operation will be 0,63 meters. This is the set parameters for the CO_2-scrubbing reservoir, and is summarized in table 7.11,

Parameter	Value
Reservoir diameter	7 m
Reservoir height	1,3 m
Solution height during operation	0,63 m
Solution mass during operation	25,2 tonnes
Solution mass during storage	50,5 tonnes

Table 7.11: Operational parameter values and mass flow for the regenerator

The CO_2-scrubber's total *mass of MEA-solution* is calculated to be *50,5 tonnes*.

Regenerator O_2/N_2-flow

In experiments conducted by Curnow et al., the maximum regeneration rate was observed at a gas flow rate of 6 liters per minute through a 500 ml MEA-solution. On this basis, a gas flow-solution volume ratio of 12 is used to calculate the needed flush gas flow rate. The surplus air from the ammonia cracker is split before entering the regenerator, one flow acting as flush gas for the solution, while the other provides heat to the MEA-solution. citecurnow2005regeneration
The regenerator holds 1,07 m^3 of MEA-solution in 2030, which gives a required gas flow rate of 12,9 m^3/min. The complete mass balance for the regenerator is given in table 7.12. It is assumed that the regenerator can completely separate the CO_2 from the MEA-solution.

Regenerator	Component	2030 ($\frac{tonnes}{year}$)	2050 ($\frac{tonnes}{year}$)
In	O_2	527,7	355,8
	N_2	3475,4	2343,0
Out	O_2	527,7	355,8
	N_2	3475,4	2343,0
	CO_2	92,1	62,1
Heating	**Component**	**2030** ($\frac{tonnes}{year}$)	**2050** ($\frac{tonnes}{year}$)
In	O_2	35444,2	23895,0
	N_2	116708,1	78679,6
Out	O_2	35444,2	23895,0
	N_2	116708,1	78679,6

Table 7.12: Mass balance for the regenerator

7.8 Electrolyte system

The electrolyte acts as a cooling agent for the AFC. Thus the needed mass flow of electrolyte is assumed to be given the amount of heat absorbed by the electrolyte, as stated in equation 7.13

$$\dot{Q}_{\text{Electrolyte}} = \dot{m}_{\text{Electrolyte}} * C_{p_{\text{Electrolyte}}} * (T_{\text{AFC}} - T_{\text{Ambient}}) \tag{7.13}$$

Where $\dot{Q}_{\text{Electrolyte}}$ is the heat absorbed by the electrolyte, $\dot{m}_{\text{Electrolyte}}$ is the mass flow of the electrolyte, $C_{p_{\text{Electrolyte}}}$ is the specific heat of the electrolyte, and T_{out} and T_{in} is the electrolyte temperature respectivley exiting and entering the AFC.
By re-arranging, the mass needed to keep the electrolyte at operating tempearture is given by equation 7.14.

$$\dot{m}_{\text{Electrolyte}} = \frac{\dot{Q}_{\text{Electrolyte}}}{C_{p_{\text{Electrolyte}}} * (T_{\text{AFC}} - T_{\text{Ambient}})} \tag{7.14}$$

The mass flow is calculated to *12,61 kg/s in 2030* and *9,25 kg/s in 2050.* To calculate the pump's volumetric flow rate, the density of the electrolyte must be estimated. Gilliam et. al., provided the empiric equation for the density of KOH-water solution seen in equation 7.15.[84]

$$\rho_{\text{Electrolyte}} = A * e^{0{,}0086 * \text{wt\%}} \tag{7.15}$$

Where A is an empiric constant for a set temperature and $wt\%$ is the weight percentage ratio of KOH in the electrolyte solution. The electrolyte has a KOH concentration of 35wt%. It is expected that the pump operates at 0°C, and the constant A is given to be 1001,9 by Gilliam et. al.
The volumetric flow rate is then calculated through equation 7.16.

$$\dot{V}_{\text{Electrolyte}} = \frac{\dot{m}_{\text{Electrolyte}}}{\rho_{\text{Electrolyte}}} \tag{7.16}$$

The electrolyte volumetric flow rate through the pump is calculated to be *12,6 l/s in 2030* and *8,5 l/s in 2050.*

8. Energy balances

8.1 Ammonia storage

As stated in section 6.1, the boil-off rate for an ammonia storage is 0,1% pr. day. To avoid pressure building up in storage, the gaseous ammonia must be guided out of the storage vessel and cooled back to liquid state. The least amount of heat which must be extracted from the ammonia during cooling, is the latent heat of condensation. Which is calculated by the equation 8.1.

$$\dot{Q}_{\mathrm{NH_3}} = m_{\mathrm{NH_3}boil-off} * L_{\mathrm{NH_3}} \tag{8.1}$$

Where $\dot{Q}_{\mathrm{NH_3}}$ is the heat transfer rate needed to condensate the ammonia, $m_{\mathrm{NH_3}boil-off}$ is the mass of the gaseous ammonia and $L_{\mathrm{NH_3}}$ is the latent heat of condensation, which is 1370 kJ/kg. The minimum daily heat needed to condensate the ammonia is calculated to be 5,7 MWh/day in 2030 and 3,9 MWh/day in 2050.
On an average, the system's daily consumption of ammonia is calculated to be 5,5 times greater than the maximum daily boil-off. This implies that the storage only will need cooling when the system is not in operation.

8.2 Heat exchanger for vaporization of NH_3

For all heat exchanger calculations, it is assumed that the specific heat of the fluids involved can be treated as constants, even though it generally changes with temperature. Due to this assumption, the heat exchanger's rate of heat transfer can be calculated by equation 8.2.

$$\dot{Q} = \dot{m} * C_p * \Delta T \tag{8.2}$$

Where $\dot{Q}$ is the rate of heat transfer, $\dot{m}$ is the mass flow rate, C_p is the specific heat and ΔT is the change in temperature through the heat exchanger. To compensate for this ideal assumption, the efficiency of the heat transfer between the fluids is assumed to be 90% for all heat exchangers.[85]
The energy balance for the vaporizing heat exchanger is stated in equation 8.3, and illustrated through figure 8.1.

$$\dot{Q}_{\text{gas mixture}} = \dot{Q}_{\mathrm{NH_3}} + \dot{Q}_{\text{losses}} \tag{8.3}$$

Where $\dot{Q}_{\text{gas mixture}}$ is the heat transferred from the gas mixture, $\dot{Q}_{\mathrm{NH_3}}$ is the heat transferred to the ammonia and $\dot{Q}_{\text{losses}}$ is the heat transferred to other parts of the heat exchanger.
The heat of the gas mixture is expressed through equation 8.4.[86]

$$\dot{Q}_{\text{gas mixture}} = \dot{m}_{\text{gas mixture}} * C_{p_{combined}} * (T_{\text{gas mixture}_{in}} - T_{\text{gas mixture}_{out}}) \tag{8.4}$$

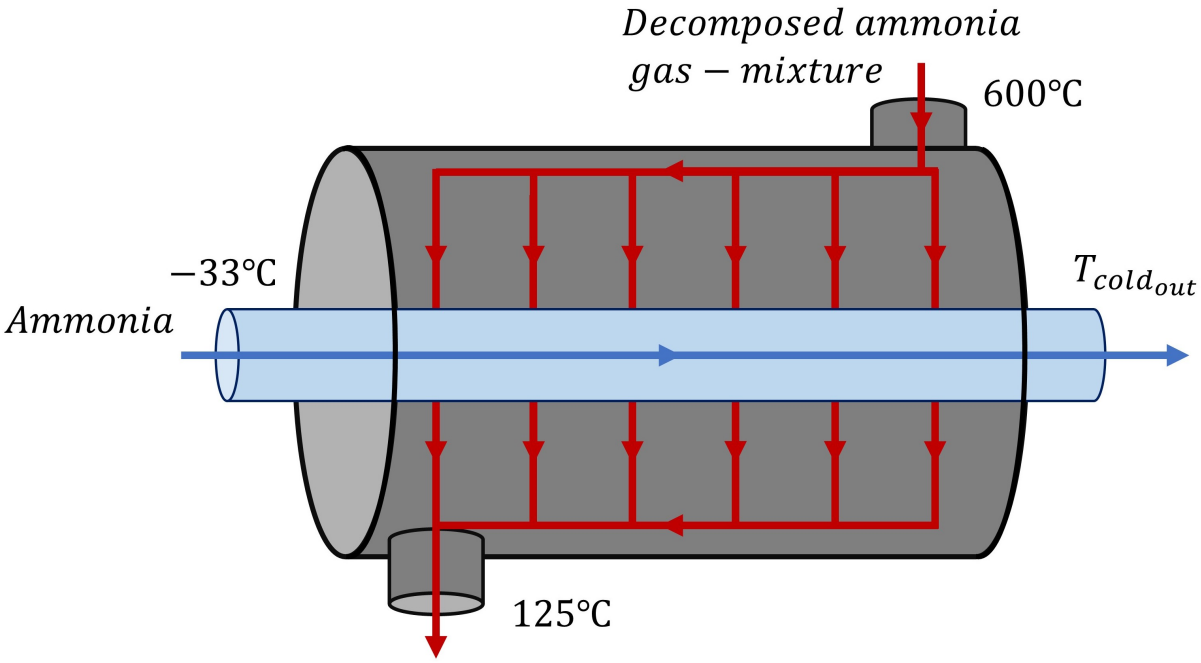

Figure 8.1: Schematic of heat transfer in the vaporizing heat exchanger

Where $\dot{m}_{\text{gas mixture}}$ is total mass flow of the components in the gas mixture, $C_{p_{combined}}$ is the combined specific heat for the components in the gas mixture and $T_{\text{gas mixture}_{in}}$ and $T_{\text{gas mixture}_{out}}$ is the temperature in and out of the heat exchanger. Which is assumed to be 600°C and 125°C respectively.
It is assumed that the convection from the gas mixture to the ammonia has an efficiency of 0,9. As stated in equation 8.5.

$$\dot{Q}_{\text{NH}_3} = \eta * \dot{Q}_{\text{gas mixture}} \tag{8.5}$$

Where η is the efficiency of the heat transfer.
As the ammonia enters the heat exchanger in liquid state, the heat first causes a phase transition, bringing the ammonia over in gaseous state. It is assumed, that ambient heat transfer causes half of the liquid ammonia to vaporize prior of entering the heat exchanger. The heat then causes an increase in temperature, as stated in equation 8.6.

$$\dot{Q}_{\text{NH}_3} = (1-n) * \dot{m}_{\text{NH}_3} * L_{\text{NH}_3} + \dot{m}_{\text{NH}_3} * C_{p_{\text{NH}_3}}(T_{\text{NH}_{3out}} - T_{\text{NH}_{3in}}) \tag{8.6}$$

Where $\dot{m}_{\text{NH}_3}$ is the mass of the ammonia, n is the amount of ammonia which is vaporized prior to the heat exchanger. L_{NH_3} is the latent heat of vaporization of ammonia, $C_{p_{\text{NH}_3}}$ is the specific heat of ammonia, and $T_{\text{NH}_{3out}}$ and $T_{\text{NH}_{3in}}$ is the ammonia's temperature in and out of the heat exchanger. By inserting equation 8.5 into equation 8.6 and re-arranging, the ammonia's temperature out of the heat exchanger is calculated through the formulation of equation 8.7.

$$T_{\text{NH}_{3out}} = T_{\text{NH}_{3in}} + \frac{\eta * \dot{Q}_{\text{gas mixture}} - (1-n) * \dot{m}_{\text{NH}_3} * L_{\text{NH}_3}}{\dot{m}_{\text{NH}_3} * C_{p_{\text{NH}_3}}} \tag{8.7}$$

From equation 8.7 it is calculated that *the temperature of the ammonia exiting the heat exchanger is 317°C.*

Through inserting the ammonia exiting temperature into equation 8.6 the heat transfered to the ammonia is calculated. The result for 2030 and 2050 are presented in table 8.1.

	Energy	**2030** ($\frac{GWh}{year}$)	**2050** ($\frac{GWh}{year}$)
In	$\dot{Q}_{\text{gasmixture}}$	6,73	4,54
Out	$\dot{Q}_{\text{NH}_3}$	6,06	4,09
	$\dot{Q}_{\text{losses}}$	0,673	0,454 height

Table 8.1: Summary of energy balance for exhaust gas and reactant heat exchanger

8.3 Ammonia cracker

For the ammonia cracker to supply the AFC with hydrogen which is within the set demands for ammonia contamination, the temperature surrounding the catalyst must remain stable at 600°C. To maintain the set temperature under operation, the cracker must balance the energy which the chemical reactions unleashes. Additionally, the combustion reaction must provide enough heat to increase the temperature of the incoming ammonia to the operational temperature. The heat balance is expressed in equation 8.8.

$$\dot{Q}_{\text{endothermic reaction}} + \dot{Q}_{temperatureincrease} \leq \dot{Q}_{\text{combustion reaction}} \tag{8.8}$$

Due to the number of products and reactants, the calculation of the combustion reaction is considered complex. To promote readability, the calculations for the heat terms in equation 8.8 are given their own subsections.

8.3.1 Temperature rise

When entering the cracker, the incoming ammonia is calculated to have a temperature of 317,3°C. The heat needed for the ammonia to reach the operating temperature is calculated through equation 8.9.

$$\dot{Q}_{\text{temperature increase}} = \dot{m}_{\text{NH}_3 * C_{p_{\text{NH}_3}} * (T_{\text{operational temperature}} - T_{in})} \tag{8.9}$$

To reach the operational temperature, he incoming ammonia must be supplied with *2,58 GWh/year* in 2030, and *1,74 GWh/year* in 2050.

8.3.2 Endothermic reaction

The endothermic reaction consumes 46,1 kJ for every mole of NH_3 which is decomposed. The total heat consumption by the endothermic reaction is calculated by multiplying the molar heat consume with the mole flow of ammonia which is converted to hydrogen and nitrogen, as seen in 8.10.

$$\dot{Q}_{\text{endothermic reaction}} = 46,1 \frac{kJ}{\text{mol NH}_3} * \dot{n}_{\text{converted NH}_3} \tag{8.10}$$

The heat consume of the endothermic reaction is calculated to be *11,28 GWH/year* in 2030, and *7,60 GWh/year* in 2050.

8.3.3 Combustion reaction

Calculations from section 8.6 states that the reactants enter the combustion chamber at 470°C. It is assumed that the reaction products exit the combustion chamber, and the ammonia cracker, holding a temperature of 600°C, the same as the catalytic temperature. In real life combustion, reactants undergo many steps to reach their final product state. The Hess' law states that a chemical reaction total change in enthalpy is the same whether the reaction is made in one or multiple steps. Which implies that the change of enthalpy in a reaction can be calculated by the difference in enthalpy between the reactants and products. Hess' law is stated in equation 8.11.[87]

$$\Delta H_{Reaction} = \sum_{R} \Delta H_{Reactants} - \sum_{P} \Delta H_{Products} \tag{8.11}$$

To write an energy balance relation for a chemically reacting system, the enthalpy needs to be expressed in a suitable form. The enthalpy expression needs to cover both the sensible enthalpy in reference to the standard state, and the enthalpy linked to the chemical bonds of a substance. For describing the latter, the enthalpy of formation represents the enthalpy of a substance at a specified state due to its chemical composition. The enthalpy term should refer to standard state, meaning when at standard state the expression should reduce to the enthalpy of formation at standard state solely. On this basis, the enthalpy of a component, on a unit-mole basis, is expressed through equation 8.12.[88] [89]

$$Enthalpy = \bar{h}_f{}^\circ + (\bar{h} - \bar{h}^\circ) \tag{8.12}$$

Where $\bar{h}_f{}^\circ$ is the standard enthalpy of formation at standard state, $\bar{h}$ is the enthalpy at the substance temperature and $\bar{h}^\circ$ is the enthalpy at standard state. All enthalpies are on a molar basis, symbolized with the lower case and the overbar.
Through utilizing the first law of thermodynamics, and neglecting kinetic- and potential energy, the energy balance of a chemically reacting steady-flow system is expressed in equation 8.13:

$$\dot{Q}_{in} + \dot{W}_{in} + \sum_{R} \dot{n}_R * (\bar{h}_f{}^\circ + \bar{h} - \bar{h}^\circ)_R = \dot{Q}_{out} + \dot{W}_{out} + \sum_{P} \dot{n}_P * (\bar{h}_f{}^\circ + \bar{h} - \bar{h}^\circ)_P \tag{8.13}$$

Where $\dot{Q}$ represents the heat transfer rate, $\dot{W}$ is the work rate. Referring to the flow chart of figure 7.4, several terms in the energy balance can be excluded. The reduced energy balance is seen in equation 8.14

$$\sum_{R} \dot{n}_R * (\bar{h}_f{}^\circ + \bar{h} - \bar{h}^\circ)_R = \dot{Q}_{out} + \sum_{P} \dot{n}_P * (\bar{h}_f{}^\circ + \bar{h} - \bar{h}^\circ)_P \tag{8.14}$$

By re-arranging equation 8.14 and applying descriptive sub-scripts, equation 8.15 was used to calculate the heat produced by the combustion reaction over a year.

$$\dot{Q}_{\text{Combustion}} = \sum_{R} \dot{n}_R * (\bar{h}_f{}^\circ + \bar{h}_{470\,\deg C} - \bar{h}^\circ)_R - \sum_{P} \dot{n}_P * (\bar{h}_f{}^\circ + \bar{h}_{600\,\deg C} - \bar{h}^\circ)_P \tag{8.15}$$

The component mass flows entering the combustion chamber were calculated in section 7.3. The component molar flows and enthalpies of relevant states are presented in table 8.2.

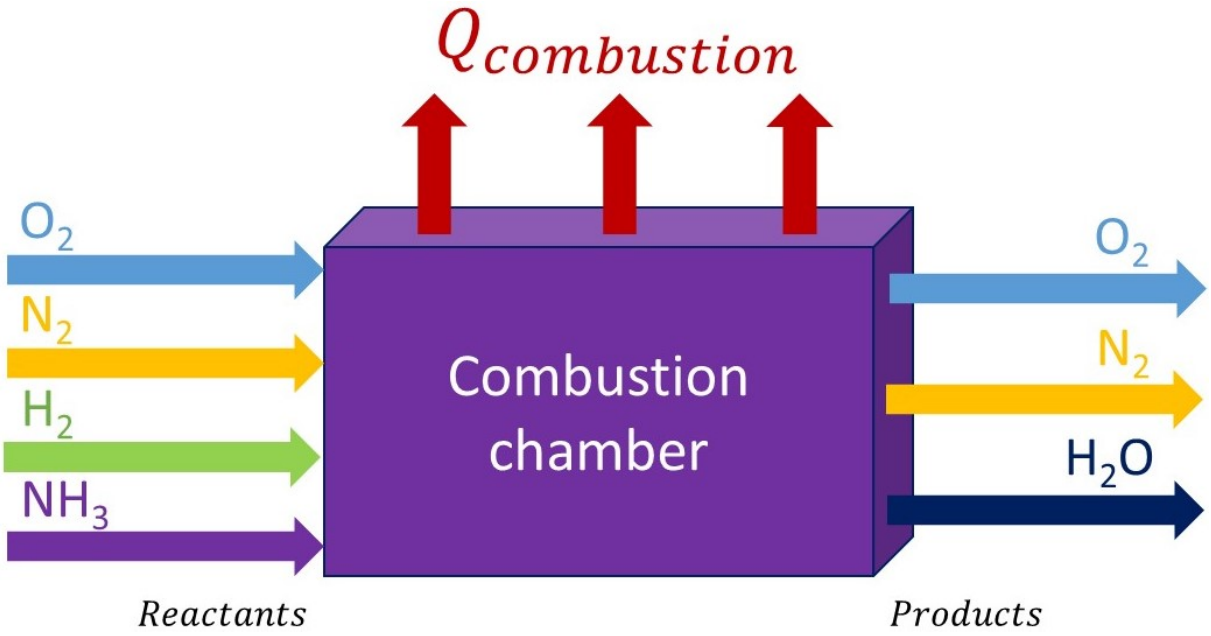

Figure 8.2: Molar flow through the combustion chamber

Reactant	$\dot{n}_{2030}$ $(\frac{\text{kmol}}{\text{year}})$	$\dot{n}_{2050}$ $(\frac{\text{kmol}}{\text{year}})$	$\bar{h}_f°$ $(\frac{\text{MJ}}{\text{kmol}})$	$\bar{h}_{440°C}$ $(\frac{\text{MJ}}{\text{kmol}})$	$\bar{h}°$ $(\frac{\text{MJ}}{\text{kmol}})$
NH_3	1765,9	1190,5	-46,19	27,887	9,825
H_2	421016,3	283831,2	0	20,807	8,468
O_2	105743,1	71287,5	0	21,514	8,682
$O_{2\text{not reacting}}$	10574,3	7128,8	21,514	4	8,682
N_2	874807,2	589757,6	0	20,912	8,669

Product	$\dot{n}_{2030}$ $(\frac{\text{kmol}}{\text{year}})$	$\dot{n}_{2050}$ $(\frac{\text{kmol}}{\text{year}})$	$\bar{h}_f°$ $(\frac{\text{MJ}}{\text{kmol}})$	$\bar{h}_{600°C}$ $(\frac{\text{MJ}}{\text{kmol}})$	$\bar{h}°$ $(\frac{\text{MJ}}{\text{kmol}})$
H_2O (g)	211486,3	142575	-241,82	30,635	9,904
$N_{2\text{from reaction}}$	883,0	595,2	0	25,928	8,669
N_2	874807,2	589757,6	0	25,928	8,669
$O_{2\text{not reacting}}$	10574,3	7128,8	0	26,889	8,682

Table 8.2: Molar flows and enthalpies used in equation 8.15. [90][91]

Through plugging the values from table 8.2 into equation 8.15, the heat generated by the combustion reaction is calculated to *13,90 GWh/year in 2030 and 9,37 GWh/year in 2050.*

8.3.4 Summary

The energy balance for the ammonia cracker is presented in table 8.3. It is evident that the demand from equation 8.8 is met, with the energy balance having a surplus of 0,03 GWh/year in 2030, and 0,02 GWh/year in 2050.

Heat	2030 ($\frac{GWh}{year}$)	2050 ($\frac{GWh}{year}$)
Endothermic reaction	-2,58	-1,74
Temperature rise	-11,28	-7,60
Combustion reaction	13,90	9,37
Energy balance	0,03	0,02

Table 8.3: Energy balance for the ammonia cracker.

8.4 Alkaline fuel cell

The AFC's energy input is the chemical energy of the H_2 dissociated from the ammonia. Energy leaves the fuel cell in four forms, as unreacted H_2, as electricity, as sensible heat through the circulating electrolyte, and as latent heat through the vaporization of water. The energy balance for the AFC is given in equation 8.16, and visualized through figure 8.3. It is assumed that the H_2O is produced, and exits the fuel cell in gaseous state.[92]

$$E_{\mathrm{H_2Input}} = E_{\mathrm{H_2Excess}} + E_{El.} + Q_{Electrolyte} + Q_{\mathrm{H_2O_{Latent\ heat}}} \tag{8.16}$$

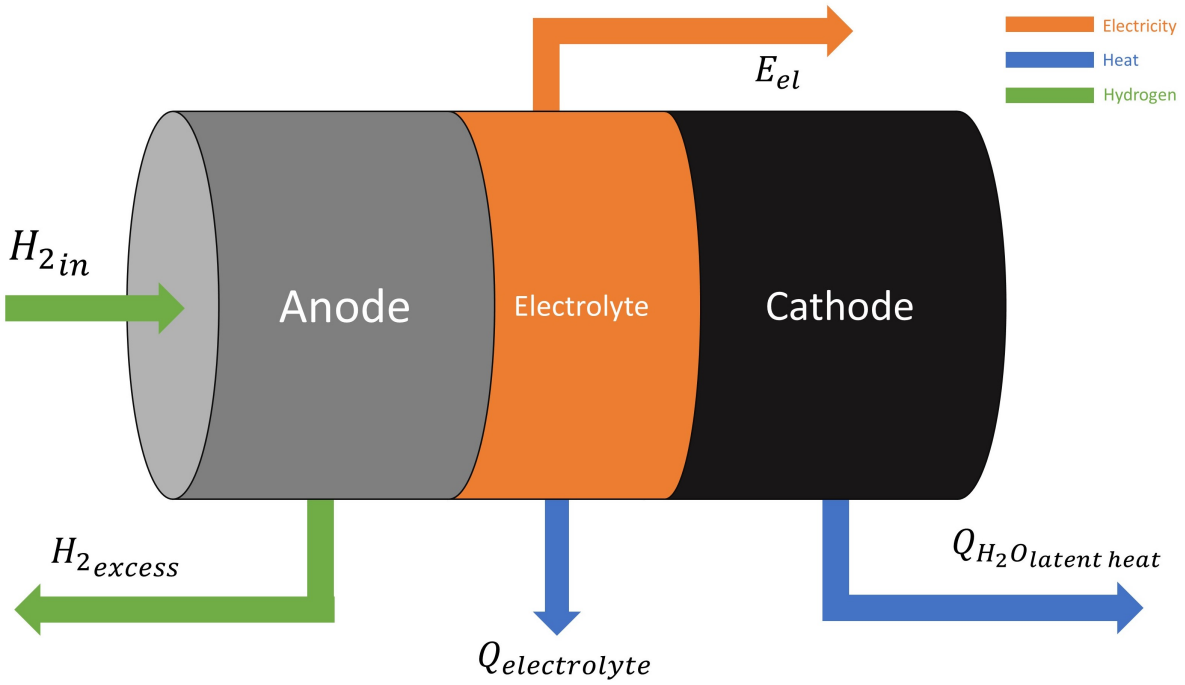

Figure 8.3: Schematic representation of the energy balance for the alkaline fuel cell

The terms in the energy balance is presented over the next subsections, and eventually summarized in table form.

8.4.1 Incoming H_2

The chemical energy in the H_2 entering the fuel cell is calculated by multiplying the mass flow with the lower heating value of H_2, as expressed in equation 8.17. The heating value of hydrogen is stated to be 120 MJ/kg.

$$E_{\mathrm{H_2Input}} = \dot{m}_{\mathrm{H_2}} * LHV \tag{8.17}$$

The chemical energy fed to the fuel cell is calculated to be *88,8 GWh/year in 2030, and 59,9 GWh/year in 2050.*

8.4.2 Unreacted H_2

The H_2 which passes through the fuel cell without reacting, is used to provide heat for the ammonia cracker. This is regarded as chemical energy leaving the AFC. By using the fuel utilization coefficient, the energy of the H_2 leaving the system can be calculated through equation 8.18.

$$E_{\mathrm{H_2Excess}} = (1 - \mu_f) * \dot{m}_{\mathrm{H_2}} * LHV \tag{8.18}$$

The energy of the H_2 exiting the fuel cell is calculated to be *14,4 GWh/year in 2030 and 9,7 GWh/year in 2050.*

8.4.3 Electricity

To estimate the electric energy output of the AFC, an estimation for its efficiency needs to be calculated. The fuel cell's efficiency is expressed through its fuel utilization, and the ratio between its operational voltage and the fuel cells reversible voltage, meaning the voltage which would be generated at no current flow, and perfect conversion from chemical to electric energy. The efficiency is calculated through equation 8.19.

$$\eta_{\mathrm{AFC}} = \mu_f * \frac{V_c}{V_r^\circ} \tag{8.19}$$

Where μ_f is the fuel utilization coefficient, V_c is the operational voltage and V_r° is the reversible voltage of at standard conditions, 25°C and 1 atm, which is stated to be 1,229 V.[93]
To estimate the AFC's operational voltage, a series of calculations have to be made. First, the fuel cell's reversible voltage at operating temperature must be calculated. Then the open-circuit voltage is found, through adding the voltage drop due to the influence of the operational pressure and gas concentrations of the working compounds. Finally, operational voltage is calculated through estimating various voltage drops which occur under operation, and subtracting the voltage drops from the open-circuit voltage.
The AFC's electric energy output is then calculated by multiplying the efficiency with the chemical energy of the incoming hydrogen. As seen in equation 8.20.

$$E_{\mathrm{El.}} = \eta_{\mathrm{AFC}} * E_{\mathrm{H_2Input}} \tag{8.20}$$

Reversible voltage

In an ideal world, the reaction of equation 7.9 would occur without energy loss, and all of the chemical energy bonded in the hydrogen is converted to electric energy, as stated in equation 8.21. This implies that no heat would be exchanged between the AFC and its surroundings, making the system thermodynamically reversible.[94]

$$E_{Chemical} = E_{Electricity} \tag{8.21}$$

For a hydrogen fuel cell, two electrons are released for every hydrogen molecule reacted. In other words, for every mole of hydrogen reacted, two moles of electric charge is passed

around the external circuit. By multiplying with the voltage put up by the fuel cell, the electric work done by the fuel cell is described by equation 8.22.

$$E_{Electricity} = -2 * F * V \tag{8.22}$$

Where the number 2 represents the moles of charge pr. H_2 molecule, F is the Faraday constant or the charge of one mole of electrons and V is the voltage put up by the fuel cell.

The term chemical energy can be defined in many ways, but for fuel cells, the Gibbs free energy is vital. The Gibbs free energy can be viewed as a thermodynamic potential, which is used for calculating the maximum reversible work a thermodynamic system can produce, at constant temperature and pressure. The Gibbs free energy of a system is stated in equation 8.23. [95]

$$G = H - T * S \tag{8.23}$$

Where G is the Gibbs free energy, H is enthalpy, T is temperature and S is entropy.
For a fuel cell, it is the change in Gibbs free energy of formation between the products and the reactants that generates the electrical energy released by the cell. As expressed in molar form in equation 8.24.

$$E_{Chemical} = \Delta\bar{g}_{f_{AFC}} = \bar{g}_{f_{\text{Products}}} - \bar{g}_{f_{\text{Reactants}}} \tag{8.24}$$

The lower casing and overbar represents the Gibbs energy being in molar form. By plugging in the reactants and products of equation 7.9, equation 8.25 is given.

$$\Delta\bar{g}_{f_{AFC}} = \bar{g}_{f_{\text{H}_2\text{O}}} - \bar{g}_{f_{\text{H}_2}} - \frac{1}{2}\bar{g}_{f_{\text{O}_2}} \tag{8.25}$$

Through using equation 8.23, the change in molar Gibbs free energy of formation for a system is stated in equation 8.27.[93]

$$\Delta\bar{g}_f = \Delta\bar{h}_f - T * \Delta\bar{s} \tag{8.26}$$

$$\Delta\bar{g}_{f_{AFC}} = \Delta\bar{h}_{f_{AFC}} - T * \Delta\bar{s}_{f_{AFC}} \tag{8.27}$$

The molar enthalpy of formation, $\Delta\bar{h}_f$ for the AFC is expressed through equation 8.28, and the molar entropy is given in equation 8.29.

$$\Delta\bar{h}_{f_{AFC}} = \bar{h}_{f_{\text{H}_2\text{O}}} - \bar{h}_{f_{\text{H}_2}} - \frac{1}{2}\bar{h}_{f_{\text{O}_2}} \tag{8.28}$$

$$\Delta\bar{s}_{AFC} = \bar{s}_{\text{H}_2\text{O}} - \bar{s}_{\text{H}_2} - \frac{1}{2}\bar{s}_{\text{O}_2} \tag{8.29}$$

The values of $\bar{h}_f$ and $\bar{s}$ are temperature dependent, and are calculated by using equation 8.30 and 8.31.

$$\bar{h}_T = \bar{h}_{298{,}15°K} + \int_{298{,}15°K}^{T} \bar{c}_p * dT \tag{8.30}$$

$$\bar{s}_T = \bar{s}_{298{,}15°K} + \int_{298{,}15°K}^{T} \frac{1}{T}\bar{c}_p * dT \tag{8.31}$$

The subscripts in the equations above is the standard temperature, $298,15K$, and $\bar{c}_p$ is the molar heat capacity at constant pressure. The values for both molar enthalpy of formation and molar entropy at standard conditions, are obtained from thermodynamic tables. The molar heat capacity is temperature-dependent, and needs to be calculated for each substance in the reaction. This is done by using the empirical equations of 8.32, 8.33 and 8.34, at the operational temperature of 125°C (398°K).[61]

$$\bar{c}_{p_{\mathrm{H_2O}}} = 143,05 - 58,084 * T^{\frac{1}{4}} + 8,2751 * T^{\frac{1}{2}} - 0,036989 * T \tag{8.32}$$

$$\bar{c}_{p_{\mathrm{H_2}}} = 56,505 - 22222,6 * T^{\frac{-3}{4}} + 116500 * T^{-1} - 560700 * T^{\frac{-3}{2}} \tag{8.33}$$

$$\bar{c}_{p_{\mathrm{O_2}}} = 37,432 - 2,0102 * 10^{-5} * T^{\frac{3}{2}} + 187570 * T^{\frac{-3}{2}} - 2368800 * T^{-2} \tag{8.34}$$

Through using the approach outlined above, *the molar Gibbs energy of formation for the AFC, operating at 125 °C, was calculated to be* $-221,13$ *MJ/kmol.*
Equation 8.22 and 8.24 is inserted in 8.21 to form equation 8.35.

$$\Delta\bar{g}_{f\,AFC} = -2 * F * V_r \tag{8.35}$$

Where V_r is the AFC's reversible voltage, which is found by re-arranging to the form of equation 8.36.

$$V_r = \frac{-\Delta\bar{g}_f}{2 * F} \tag{8.36}$$

The *reversible voltage of the AFC*, at a working temperature of 125°C, is calculated to be *1,146 V.*

Open-circuit voltage

In the last subsection, the AFC's reversible voltage was calculated based on its operating temperature. But the theoretical cell potential is not only dependant on the operating temperature, but also the product and reactant pressure and concentration. As the previous calculations were based on the fuel cell reacting on pure hydrogen and oxygen, and the AFC is fed air and hydrogen in a mixture with nitrogen and unreacted ammonia, the reversible, open-circuit voltage needs to be corrected for concentration and reactant pressure. [96]
Each of the components involved in the reaction has an associated activity. The thermodynamic activity can be seen as a measure of 'effective concentration', and is dependent on the temperature, pressure and composition of the system. Assumed that reactants and products behave as ideal gasses, the activity of the components are described through equation 8.37.

$$a_{Component} = \frac{P_{component}}{P^\circ} \tag{8.37}$$

Where $a_{Component}$ is the components activity, $P_{Component}$ is the components partial pressure and P° is the standard pressure.
Dalton's law states that the total pressure of a mixture of gases in a volume is equal to the sum of all the pressures of the individual gases in the mixture. Assuming the gas

mixtures act as an ideally, the components mole fraction can be used to calculate its partial pressure. As described through equation 8.38.[97]

$$P_{Component} = X_{Component} * P_{Total} \tag{8.38}$$

Where $X_{Component}$ is the mole fraction of the component, and P_{Total} is the total pressure of the gas. The composition of the incoming and exiting gas mixtures are given in table 8.4.

Anode in		Cathode in		Anode out	
Component	**X** (mol%)	**Component**	**X** (mol%)	**Component**	**X** (mol%)
H_2	*0,749*	*O_2*	*0,210*	H_2	0,118
N_2	0,249	N_2	0,790	N_2	0,249
NH_3	0,001			NH_3	0,001
				H_2O (g)	*0,631*

Table 8.4: Molar compesition of the AFC's air-, fuel- and exhaust mixture. Reactants and products marked in italic.

The Nernst equation is important in electrochemistry, as it enables the determination of cell potentials at non-standard conditions. It relates the temperature and activities of the reacting components to the reduction of cell potential. The Nernst equation for an open-circuit, hydrogen fed fuel cell, is given in equation 8.39.[98]

$$V_{\text{O.C.}} = V_r^\circ + \frac{R * T}{2 * F} * ln(\frac{a_{\text{H}_2} * a_{\text{O}_2}^{\frac{1}{2}}}{a_{\text{H}_2\text{O}}}) \tag{8.39}$$

Where V_r° is the reversible voltage at standard conditions, R is the gas constant, T is the temperature, F is the Faraday constant and a represents the activity of the various components.
As the temperature contribution to the voltage loss is considered to be linear in equation 8.39, it is chosen to use the reversible voltage calculated through equation 8.36. Which is considered to give a more just evaluation, due to the highly un-linear specific heats that have been used in its calculation. The altered equation is seen in equation 8.40.

$$V_{\text{O.C.}} = V_r + \frac{R * T}{2 * F} * ln(\frac{a_{\text{H}_2} * a_{\text{O}_2}^{\frac{1}{2}}}{a_{\text{H}_2\text{O}}}) \tag{8.40}$$

The voltage drop due to the activity of the chemical components is calculated to be *-0,0037 V*, which gives the AFC an open-circuit voltage of *1,142 V*.

Operational voltage

Under operation, the fuel cell voltage drops below the reversible voltage due to four major thermodynamic irreversibilities listed in table 8.5. The AFC's operational voltage is given through equation 8.41, and the basis for each voltage drop is elaborated over the next pages.[99]

$$V_{\text{Operational}} = V_{O.C.} - \Delta V_{\text{Activation losses}} - \Delta V_{\text{Ohmic losses}} - \Delta V_{\text{Concentration losses}} \tag{8.41}$$

Type of voltage loss	Technical cause
Internal currents and fuel crossover	Hydrogen and electrons passing through the electrolyte
Activation losses	Slowness of the reactions taking place on the surface of the electrodes
Ohmic losses	Resistive losses in electrode and electrolyte
Concentration losses	Change in reactant concentration on the surface of the electrodes under fuel consumption.

Table 8.5: Thermodynamic irreversibilities and their origin

Internal current and fuel crossover
In an ideal situation, the electrolyte should only transfer OH^--ions through the cell. However, in real-life fuel cells, a certain amount of hydrogen and electrons will diffuse through the electrolyte, even at open-circuit situations. Both the fuel loss and internal current are of a very small order, but the current crossover has a significant influence on the open-circuit voltage, especially for low-temperature fuel cells. The internal current crossover can be regarded as constant for all fuel cell current densities, and must, therefore be added to the current density put up by the fuel cell for all voltage loss calculations. The internal current crossover is represented by i_n, and is selected to be *2 mA/cm^2* by example value for low-temperature fuel cells, provided by Dicks et. al. The voltage loss due to the internal current crossover is calculated to be *0,102 V*, lowering the AFC's open-circuit voltage to *1,039 V*.[100][101]
The voltage loss due to fuel crossover is regarded to be of an order so small that it is considered negligible.

Activation losses
In table 8.5 the activation losses is listed to be caused by the slowness of the reactions taking place on the surface of the electrodes. The activation losses can be considered a combination of two phenomenons, the exchange-current on the electrode surface at low current densities and the rate of the electrochemical reaction at the electrode during operation. For a fuel cell, the activation losses is described by rephrasing the Tafel Equation, to equation 8.42. [102]

$$\Delta V_{\text{Activation losses}} = A * ln(\frac{i + i_n}{i_o}) \tag{8.42}$$

Where i is the fuel cells emitted current density, i_o is the exchange-current density and A is a constant describing the rate of the reactions at the electrodes. The number of intermediate steps a reaction needs to go through to reach its final state is decisive for the electrodes reaction rate. For a hydrogen fuel cell, the constant A is given by equation 8.43.

$$A = \frac{R * T}{2 * \alpha * F} \tag{8.43}$$

Where R is the gas constant, T is the fuel cell operational temperature, F is the Faraday constant, α is the change-transfer coefficient. The change transfer coefficient represents the fraction of the electrical energy applied which is harnessed when changing the rate of

the electrochemical reaction. For the AFCs cathode, a *change transfer coefficient of 0,5* is selected, which is within the range of common values given by Dicks et. al.[103]
When a fuel cell operates at zero current density, intuitively, no reactions are accruing. In reality, the reaction is at equilibrium, and the voltage causes the electrons to continuously flow back and forth from the electrode. The current density of this electron flow is regarded as the *exchange-current density*, which is given the symbol i_o. For the AFC's cathode, an *exchange-current density of 0,1 mA/cm²* have been chosen, which is based on example value given by Dicks et. al.
The activation loss across the fuel cell is not uniform, in fact, there is a considerable difference in activation loss at each electrode. The oxygen reduction reaction at the cathode is many times slower than the hydrogen oxidation reaction at the anode, due to the multiple reaction steps needed for the cathode reaction. The complexity of the reaction also affects the exchange-current, which is generally 10^5 times lower at the cathode than at the anode. Therefore the activation losses at the anode is considered negligible compared with the cathode.

Ohmic losses
Ohmic losses is a collective term for the voltage loss linked to the electrodes electrical resistance, and the resistance the ions are exposed to in the electrolyte. The voltage loss is linear to the current density and is described through rephrasing Ohm's law as seen in equation 8.44.

$$\Delta V_{\text{Ohmic losses}} = (i + i_n) * r \tag{8.44}$$

Where r is the AFC's area specific resistance, having $k\Omega*cm^2$ as denomination, and is selected to be $30*10^{-6}$ $k\Omega*cm^2$. Which is an example value for low temperature fuel cells provided by Dicks et. al.[104][101]

Concentration losses
Due to the continuous consumption of the reacting components, part of the electrodes will experience gas mixtures with lower concentrations of the reactants. As described through equations 8.37 to 8.40, the concentration of the reacting components affect the components partial pressure and subsequently the voltage generated by the fuel cell. The Nernst equation can be used to estimate the voltage drop caused by the decrease in concentration, and its final form is given in equation 8.45.

$$\Delta V_{\text{Concentration losses}} = -B * ln(1 - \frac{i + i_n}{i_l}) \tag{8.45}$$

Where B is a parameter which describes the fuel cell's composition and operating state, given in complete form in equation 8.46. i_l is the fuel cell's limiting value for current density. At a current density of i_l, the fuel is consumed at a rate equal to its maximum fuel supply rate. For the AFC, the *limiting current density is assumed to be 900 mA/cm²*, which is in correlation with example values provided by Dicks et. al.. [105]

$$B = \frac{R * T}{2 * F} \tag{8.46}$$

Electric power output from Fuel cell

By inserting equation 8.42, 8.44 and 8.45 into equation 8.41, the AFC's operational voltage can be described as a function of its current density. The function is expressed in equation 8.47.

$$V_c = V_{o.c.} - (i + i_n) * r - A * ln(\frac{i + i_n}{i_o}) - B * ln(1 + \frac{i + i_n}{i_l}) \tag{8.47}$$

The values inserted to equation 8.47 have been elaborated for in the previous subsections, and are summarized in table 8.6.

Phenomenon	Notation	Value	
Open circuit voltage	$V_{o.c.}$	1,1422	V
Internal current crossover	i_n	2	mA/cm^2
Area specific resistance	r	$60*10^6$	$k\Omega * cm^2$
Constant describing reaction rates	A	0,0342	V
Exchange-current denisty	i_o	0,1	mA/cm^2
Constant describing operating state	B	0,06	V
Limit current density	i_l	900	mA/cm^2

Table 8.6: Summary of parameter values used in equation 8.47

The AFC's operating voltage is plotted in figure 8.4, along with the AFC's power density, which is expressed through equation 8.48.

$$\frac{P}{A} = V_{\text{o.c.}} * i \tag{8.48}$$

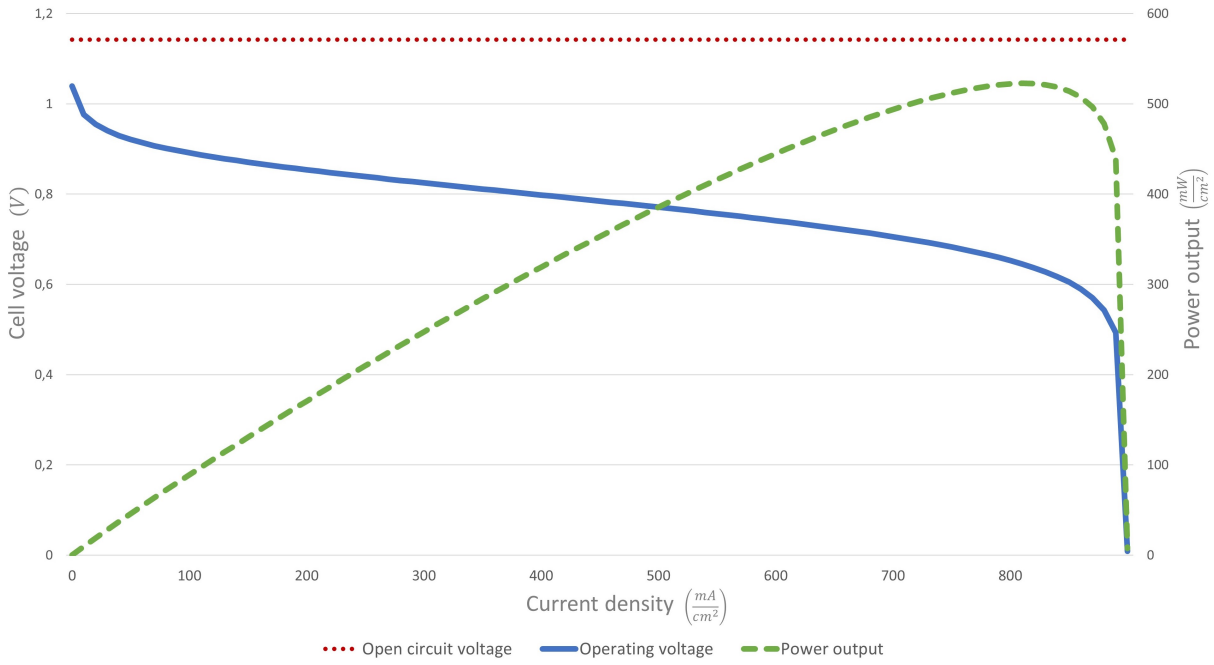

Figure 8.4: AFC operating voltage and power density plotted as a function of current density

Through apex calculations in excel, the AFC's *peak power density output* is calculated to be *522,7 mW/cm²*. The peak power density occurs at an *operating voltage of 0,645 V*, and a *current density of 810 mA/cm²*. It is assumed that the AFC can be controlled to operate steadily at peak power conditions. Through inserting the operating voltage at peak power density into equation 8.19, along with the fuel utilization coefficient of 0,842 and the standard fuel cell voltage at standard conditions, which is listed to 1,229 V, *the efficiency of the AFC is calculated to be 0,4421.* The efficiency is then inserted to equation 8.20 together with the chemical energy of the hydrogen in 2030 and 2050. The *electric energy* produced by the AFC is calculated to be *39,1 GWh/year in 2030* and *26,1 GWh/year in 2050.*[93]

8.4.4 Latent heat in H_2O

The heat of the formed water, which is in gaseous state is assumed to be equal to the heat of vaporization for the mass of the produced water, as stated in equation 8.49.

$$Q_{\text{Latent heat}} = \dot{m}_{\text{H}_2\text{O}} * L_{\text{H}_2\text{O}} \tag{8.49}$$

Where $\dot{m}_{\text{H}_2\text{O}}$ is the mass of the water exiting the AFC and $L_{\text{H}_2\text{O}}$ is the latent heat of water, which is 2264,7 kJ/kg.
The heat related to the vaporization of the produced water is calculated to be *12,6 GWh/year in 2030* and *8,5 GWh/year in 2050.*

8.4.5 Heat in electrolyte

As all other terms are calculated, the heat absorbed in the electrolyte is calculated through re-arranging equation 8.16, and is formulated in equation 8.50.

$$Q_{Electrolyte} = E_{\text{H}_2\text{Input}} - E_{\text{H}_2\text{Excess}} - E_{El.} - Q_{\text{H}_2\text{O}_{\text{Latent heat}}} \tag{8.50}$$

The heat absorbed in the electrolyte is calculated to be *22,8 GWh/year in 2030 and 15,4 GWh/year in 2050.*

8.4.6 Summary

The energy balance is presented in table 8.7. All values are rounded to one decimal.

	Energy	**2030** ($\frac{GWh}{year}$)	**2050** ($\frac{GWh}{year}$)
In	$E_{\text{H}_2\text{Input}}$	88,8	59,9
Out	$E_{\text{H}_2\text{Excess}}$	14,4	9,7
	$E_{El.}$	39,3	26,5
	$Q_{\text{H}_2\text{O}_{\text{Latent heat}}}$	12,6	8,5
	$Q_{Electrolyte}$	22,8	15,4

Table 8.7: Energy balance for the AFC

8.5 Condensing heat exchanger

The energy balance for the condensing heat exchanger is stated in equation 8.51, and illustrated through figure 8.5.

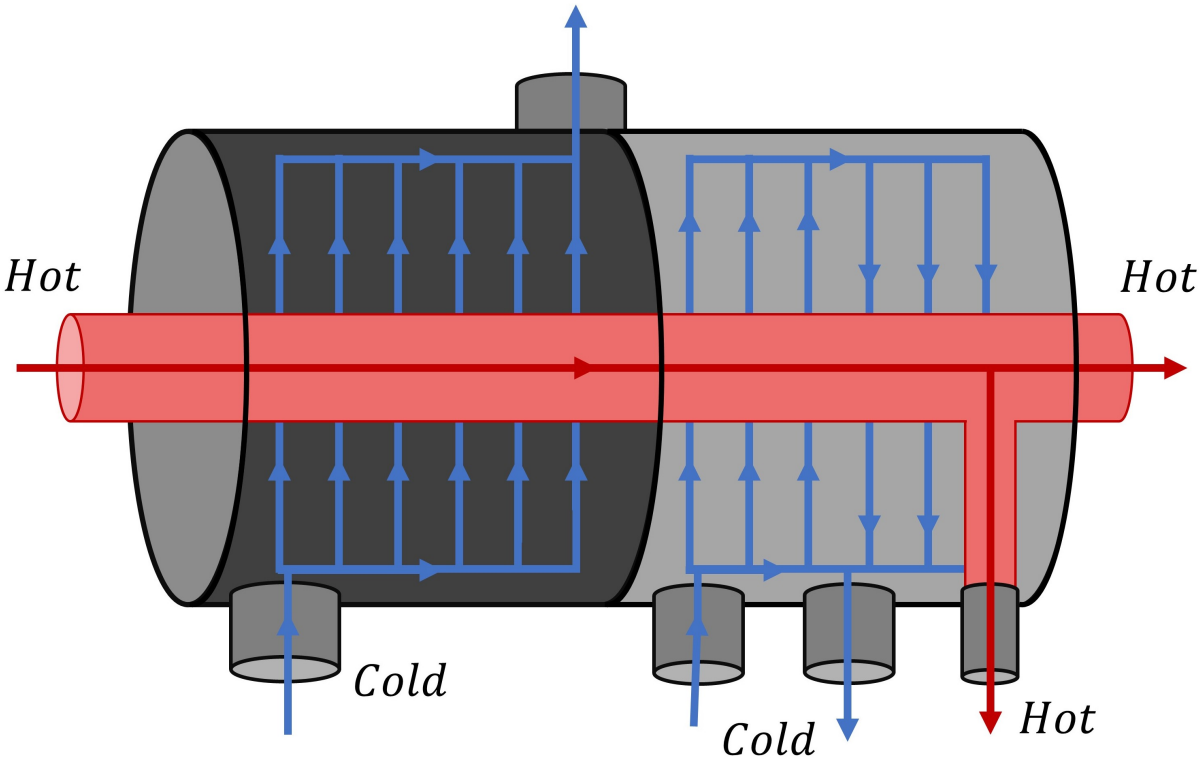

Figure 8.5: Schematic for the heat transfer in the condensing heat exchanger and district heating heat exchanger

$$\dot{Q}_{\text{Con. } H_2O} = \dot{Q}_{\text{air}} + \dot{Q}_{\text{district heating}} + \dot{Q}_{\text{losses}} \tag{8.51}$$

Where $\dot{Q}_{\text{Con. } H_2O}$ is the heat transferred from the condensing water, $\dot{Q}_{\text{air}}$ is the heat transferred to the air, $\dot{Q}_{\text{district heating}}$ is the heat provided for district heating and $\dot{Q}_{\text{losses}}$ represents the heat which failed to be transferred to the low temperature fluids.
The heat emitted by the condensing water is expressed through equation 8.52.

$$\dot{Q}_{\text{Con. } H_2O} = \dot{m}_{H_2O} * L_{H_2O_{@125°C}} \tag{8.52}$$

Where $\dot{m}_{H_2O}$ is the mass flow of the water and the $L_{H_2O_{@125°C}}$ is water's latent heat of vaporization at 125°C. *The heat of the condensing water* is calculated to be *12,1 GWh/year in 2030* and *8,2 GWh/year in 2050.*
The heat needed to increase the temperature from ambient temperature, 0 °C, to the fuel cells working temperature is expressed through equation 8.53.

$$\dot{Q}_{\text{air}} = \dot{m}_{\text{air}} * C_{p_{\text{air}}} * (T_{\text{Cold}_{\text{out}}} - T_{\text{Cold}_{\text{in}}}) \tag{8.53}$$

Where $\dot{m}_{\text{air}}$ is the mass flow of the air, $C_{p_{\text{air}}}$ is the air's specific heat capacity and $T_{\text{Cold}_{\text{out}}}$ and $T_{\text{Cold}_{\text{in}}}$ is the temperature of the air going out and in of the heat exchanger. *The heat needed for the air to reach exiting temperature* is calculated to *5,4 GWh/year in 2030* and

3,6 GWh/year in 2050.
The remaining heat of the condensing water is expressed through equation 8.55.

$$\dot{Q}_{\text{excess}} = \dot{Q}_{\text{Con. } H_2O} * \eta - \dot{Q}_{\text{air}} \tag{8.54}$$

Where Q_{excess} is the remaining heat bound to the water vapor and η is the heat exchanger efficiency of 0,9. It is assumed that all the remaining water vapor is condensed, and the heat available for the district heating system is stated in equation 8.55.

$$\dot{Q}_{\text{district heating}} = \dot{Q}_{\text{excess}} * \eta \tag{8.55}$$

The heat available for the district heating system is presented in table 8.8, along with the heat losses.

	Energy	**2030** $(\frac{GWh}{year})$	**2050** $(\frac{GWh}{year})$
In	$\dot{Q}_{\text{Con. } H_2O}$	12,1	8,2
Out	$\dot{Q}_{\text{air}}$	5,4	3,6
	$\dot{Q}_{\text{district heating}}$	5,0	3,4
	$\dot{Q}_{\text{losses}}$	1,8	1,2

Table 8.8: Summary of energy balance for exhaust gas and reactant heat exchanger

8.6 Heat exchanger for exhaust gas and combustion reactants

The energy balance for the exhaust gas heat exchanger is given in equation 8.56, and illustrated through figure 8.6.

$$\dot{Q}_{\text{exhaust}} = \dot{Q}_{\text{H}_2\text{-mixture}} + \dot{Q}_{\text{air-mixture}} + \dot{Q}_{\text{losses}} \tag{8.56}$$

Where $\dot{Q}_{\text{exhaust}}$ is the heat transferred from the exhaust gas mixture, $\dot{Q}_{\text{H}_2\text{-mixture}}$ is the heat transferred to the H_2-mixture, $Q_{\text{air-mixture}}$ is the heat transferred to the air mixture and $\dot{Q}_{\text{losses}}$ represents the heat loss, which is not transferred to the low temperature fluids. The heat transferred from the exhaust gas is expressed through equation 8.57.

$$\dot{Q}_{\text{exhaust}} = \dot{m}_{\text{exhaust}} * C_{p_{\text{exhaust}}} * (T_{\text{Hot}_{\text{in}}} - T_{\text{Hot}_{\text{out}}}) \tag{8.57}$$

Where $\dot{m}_{\text{exhaust}}$ is the mass flow rate of the exhaust gas, $C_{p_{\text{exhaust}}}$ is the combined specific heat for the exhaust gas, and $T_{\text{Hot}_{\text{in}}}$ and $T_{\text{Hot}_{\text{out}}}$ is the temperature of the exhaust respectively in and out of the heat exchanger. *The heat transferred by the exhaust gas* is calculated to be *4,74 GWh in 2030* and *3,20 GWh in 2050.*
To determine the heat absorbed of each of the cold-side fluid mixtures, their exit temperature needs to be calculated. The heat transferred to the H_2-mixture is expressed through equation 8.58

$$\dot{Q}_{\text{H}_2\text{-mixture}} = \dot{m}_{\text{H}_2\text{-mixture}} * C_{p_{H_2-mixture}} * (T_{\text{Cold}_{\text{out}}} - T_{\text{Cold}_{\text{in}}}) \tag{8.58}$$

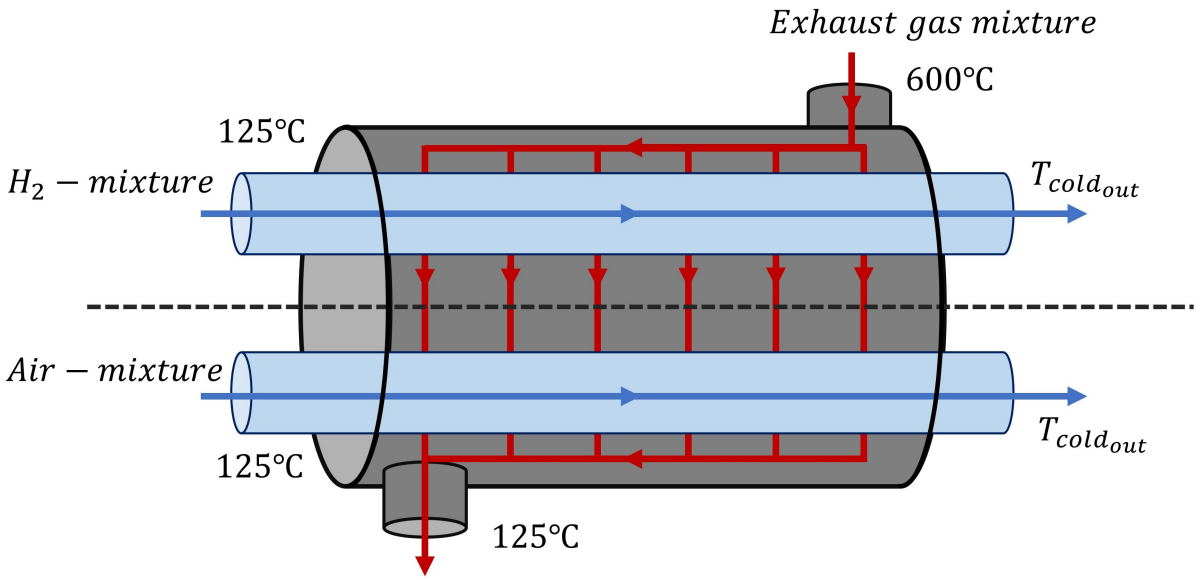

Figure 8.6: Schematic of heat transfer in the exhaust gas and comustion reactant heat exchanger

Where $\dot{m}_{\text{H}_2\text{-mixture}}$ is the mass flow rate of the H_2-gas mixture, $C_{p_{H_2-mixture}}$ is the combined specific heat for the H_2-gas mixture, and $T_{\text{Cold}_{\text{out}}}$ and $T_{\text{Cold}_{\text{in}}}$ is the temperature of the H_2-gas mixture respectively out and in of the heat exchanger.
The heat transferred to the H_2-mixture is expressed through equation 8.59

$$\dot{Q}_{\text{air-mixture}} = \dot{m}_{\text{air-mixture}} * C_{p_{air-mixture}} * (T_{\text{Cold}_{\text{out}}} - T_{\text{Cold}_{\text{in}}}) \tag{8.59}$$

Where $\dot{m}_{\text{air-mixture}}$ is the mass flow rate of the air-mixture, $C_{p_{air-mixture}}$ is the combined specific heat for the air mixture, and $T_{\text{Cold}_{\text{out}}}$ and $T_{\text{Cold}_{\text{in}}}$ is the temperature of the air mixture respectively out and in of the heat exchanger.
The cold-side heat flows are added up, and set equal to the heat of the exhaust gas multiplied with the efficiency of the heat transfer. As stated in equation 8.60.

$$\dot{Q}_{\text{exhaust}} * \eta = \dot{Q}_{\text{H}_2\text{-mixture}} + \dot{Q}_{\text{air-mixture}} \tag{8.60}$$

Where η is the efficiency of the heat transfer, which is assumed to be 0,9. Equations 8.57 and 8.58 are inserted into equation 8.60, and re-arranged to isolate the cold-side exiting temperature. As seen in equation 8.61.

$$T_{\text{Cold}_{\text{out}}} = T_{\text{Cold}_{\text{in}}} + \frac{\dot{Q}_{\text{exhaust}} * \eta}{m_{\text{H}_2\text{-mixture}} * C_{p_{H_2-mixture}} + \dot{m}_{\text{air-mixture}} * C_{p_{air-mixture}}} \tag{8.61}$$

From equation 8.61 it is calculated that *the H_2-gas mixture and air-mixture exits the heat exchanger with a temperature of 438°C.*
Through inserting the calculated exiting temperature into equation 8.57 and 8.58, the heat transferred to each fluid is calculated. The result of the calculations are presented in table 8.9, along with the heat losses.

	Energy	2030 ($\frac{GWh}{year}$)	2050 ($\frac{GWh}{year}$)
In	$\dot{Q}_{\text{exhaust}}$	4,74	3,20
Out	$\dot{Q}_{\text{H2-mixture}}$	1,67	1,12
	$\dot{Q}_{\text{air-mixture}}$	2,59	1,75
	$\dot{Q}_{\text{losses}}$	0,474	0,320

Table 8.9: Summary of heat balance for exhaust gas and reactant heat exchanger

8.7 CO_2-scrubber

Energy balance for the CO_2-scrubber is split into a heat balance and the electric energy required by the pump to circulate the MEA-solution through the CO_2-scrubber.

Heat

It is assumed that both the air-mixture used as flush-gas and the air-mixture used for heating contribute to raising the temperature of the MEA-solution, and that the heat from the air mixture is transferred directly to the MEA-solution, without using a heat transfer medium. The heat needed to increase the temperature of the MEA-solution from the absorber temperature, T_{Absorber}, of 0°C to the operating temperature of the regenerator, $T_{\text{Regenerator}}$, of 120°C, is stated in equation 8.62.

$$\dot{Q}_{\text{Regenerator}} = \dot{m}_{\text{solution}}\dot{m}_{\text{solution}} * C_{p_{\text{solution}}} * (T_{\text{Regenerator}} - T_{\text{Absorber}}) \tag{8.62}$$

Where $\dot{Q}_{\text{Regenerator}}$ is the heat needed to increase the solution temperature in the generator, $\dot{m}_{\text{solution}}$ is the mass flow of the solution and $C_{p_{\text{solution}}}$ is the specific heat capacity of the solution. The heat needed is calculated to be 0,11 GWh/year in 2030 and 0,07 GWh/year in 2050.
It is assumed that the efficiency of the heat transfer $\eta_{heattransfer}$ is 0,9, and the heat received by the MEA-solution in the regenerator from the heat in the air-mixture is stated in equation 8.63.

$$\dot{Q}_{\text{Regenerator}} = \dot{Q}_{\text{N}_2/\text{O}_2} * \eta_{heattransfer} \tag{8.63}$$

The heat supplied from the air-mixture is calculated to be *0,117 GWh/year in 2030* and *0,079 GWh/year in 2050*
As stated in 7.7, it is assumed that the reservoir can transfer heat to the surroundings at a rate equal to the rate in which heat is fed to MEA-solution. The heat balance for the CO_2-scrubber is presented in table 8.10.

	Energy	2030 ($\frac{GWh}{year}$)	2050 ($\frac{GWh}{year}$)
In	$\dot{Q}_{\text{N}_2/\text{O}_2}$	0,118	0,079
Out	$\dot{Q}_{\text{Reservoir}}$	0,106	0,071
	$\dot{Q}_{\text{losses}}$	0,012	0,008

Table 8.10: Summary of heat balance for CO_2-scrubber

As proof for the feasibility of using the air-mixture to provide heat for the CO_2-scrubber, its exiting temperature from the regenerator is calculated.

The heat transferred from the air-mixture is represented by $\dot{Q}_{N_2/O_2}$, and is derived in equation 8.64.

$$\dot{Q}_{N_2/O_2} = \dot{m}_{N_2/O_2} * C_{p_{N_2/O_2}} * (T_{in} - T_{out}) \tag{8.64}$$

Where $\dot{m}_{N_2/O_2}$ is the mass flow of the air-mixture, $C_{p_{N_2/O_2}}$ is the specific heat capacity of the air mixture and T_{in} and T_{out} is the temperature in and out of the regenerator. By inserting equation 8.63 into equation 8.64, the temperature of the air-mixture exiting the regenerator is stated in equation 8.65.

$$T_{out} = T_{in} - \frac{\dot{Q}_{Regenerator}}{\eta_{heattransfer} * \dot{m}_{N_2/O_2} * C_{p_{N_2/O_2}}} \tag{8.65}$$

The temperature of the air mixture exiting the regenerator is calculated to 121,1°C, which proves that using the air-mixture for heating the MEA-solution is viable, as it is higher than the MEA-solution temperature of 120°C.

Electricity

The power needed to elevate the MEA-solution to the absorber's operating pressure and flow is stated through equation 8.66

$$P_{Pump} = p_{solution} * \dot{V}_{solution} \tag{8.66}$$

Where P_{Pump} is the mechanical power the pump provides to the MEA-solution, $p_{solution}$ it the AFC's operating pressure of 2,2 bar and $\dot{V}_{solution}$ is the volumetric flow rate of the solution, which is calculated to 0,09 l/s in 2030 and 0,06 l/s in 2050.
As the height difference between the pressure and suction side of the pump is small, the height of the solution in the reservoir will have a significant contribution to the pressure perceived by the pump, which is expressed in equation 8.67.

$$p_{pump} = rho_{solution} * g * (h_{absorber} - h_{reservoir}) \tag{8.67}$$

Where $rho_{solution}$ is the density of the solution, which is calculated to 1045,5 kg/m^3, g is the gravitational constant and $h_{absorber}$ and $h_{reservoir}$ is the height to the solution surface in the absorber and reservoir respectively.
The electric power needed is calculated by dividing the mechanical power provided by the pump with its efficiency and the efficiency of the electric motor that drives it, as expressed in equation 8.68. The pump efficiency, η_{Pump} is assumed to be 0,85, and the efficiency of the motor is assumed to be 0,95.

$$P_{El.} = \frac{P_{Pump}}{\eta_{Pump} * \eta_{Motor}} \tag{8.68}$$

The electric power needed to drive the pump is calculated to be *3,0 W in 2030* and *2,0 W in 2050*. In a year, the electric energy consumed by the pump is *13,1 kWh in 2030* and *8,8 kWh in 2050*.

8.8 Electrolyte system

The energy flow in the electrolyte system is visualized through the schematic in figure 8.7. In addition to electricity and product water, the electrochemical reactions at the

electrodes release heat. The heat is then transferred to the circulating electrolyte. It is assumed that the electrolyte can be stored outdoors since the 35% KOH-solution freezes at -50°C. The reservoir temperature is the same as the ambient temperature, 0°C, and it is assumed that the electrolyte will enter the AFC at 0°C. The electrolyte will act as a coolant for the AFC, and balance its temperature operating temperature at 125°C. This gives that the electrolyte solution exiting the AFC holds 125°C. On its way back to the reservoir, the electrolyte passes through a heat exchanger connected to the district heating system. The amount of heat transferred is dependent on the operating temperature of the district heating, and is calculated in section 8.11. The electrolyte exits the heat exchanger at the temperature of the district heating and is fed back to the reservoir, where the remaining heat is transferred to the surroundings of the reservoir. It is assumed that the electrolyte is given time to cool until reaching the ambient temperature, before re-entering the AFC.[106]
The energy balance for the electrolyte system is split into a heat balance, and the electric energy required by the pump to circulate the electrolyte.

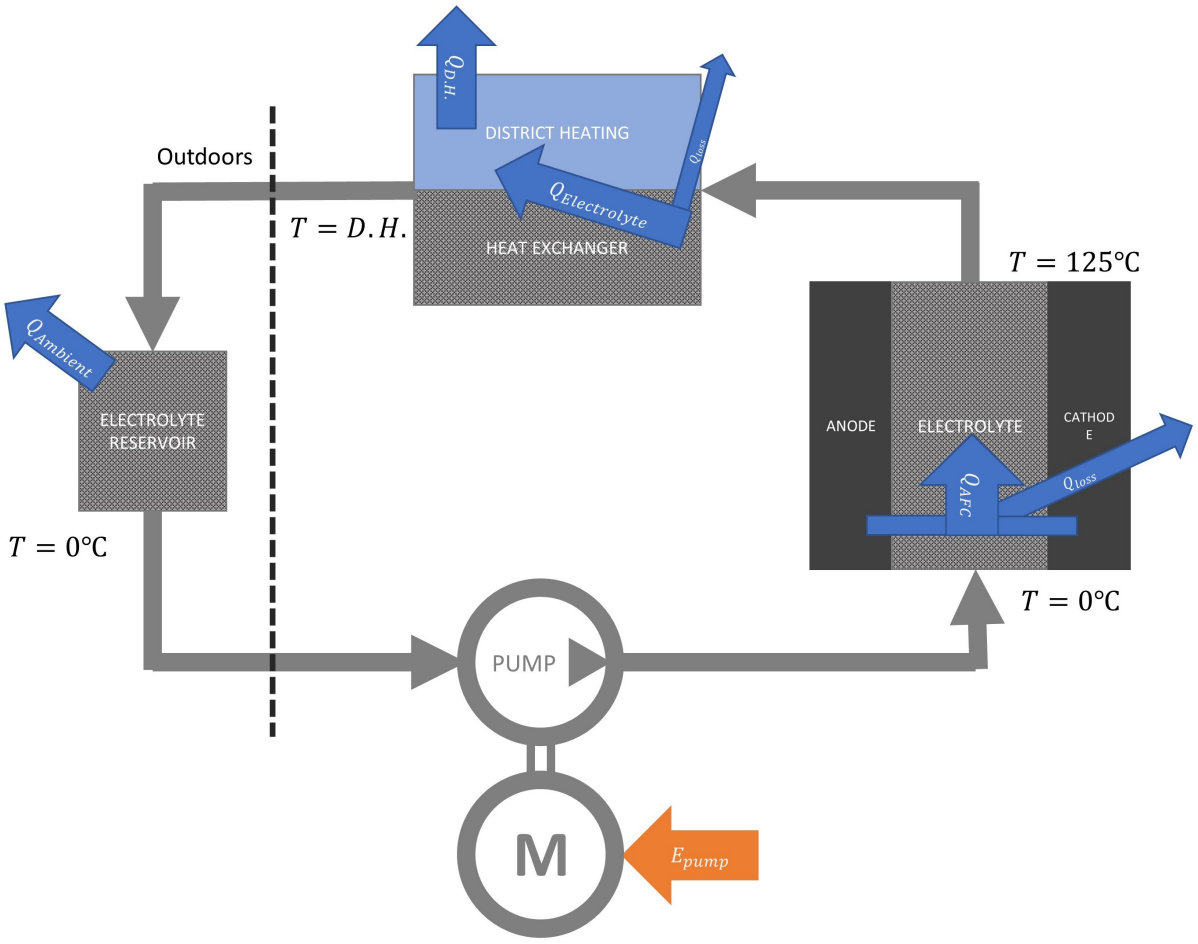

Figure 8.7: Schematic of the heat balance for the Electrolyte system

Heat

The heat balance for the electrolyte system is given through equation 8.69.

$$\dot{Q}_{\text{AFC}} = \dot{Q}_{\text{District heating}} + \dot{Q}_{\text{Ambient}} + Q_{\text{Loss (AFC)}} + Q_{\text{Loss (HE)}} \tag{8.69}$$

Where $\dot{Q}_{\text{AFC}}$ is the heat emitted by the electrodes of the AFC, $\dot{Q}_{\text{District heating}}$ is the heat transferred to the district heating, $\dot{Q}_{\text{Ambient}}$ is the heat transferred to the surroundings of the reservoir and $\dot{Q}_{\text{Loss (AFC)}}$ and $\dot{Q}_{\text{Loss (HE)}}$ represents the heat lost to the surroundings in the AFC and heat exchanger. It is assumed that the heat transfer to the electrolyte has an efficiency of 95%. The heat transferred to the electrolyte is described by equation 8.70.

$$\dot{Q}_{\text{Electrolyte}} = \dot{Q}_{\text{AFC}} * \eta_{\text{AFC}} \tag{8.70}$$

Where $\dot{Q}_{\text{Electrolyte}}$ is the heat transferred to the electrolyte, and η_{AFC} is the efficiency of the heat transfer.
As stated, the heat transferred to the district heating is dependent on its operating temperature. The portion of heat fed to the district heating for each scenario is covered in section 8.11, and the heat which forms the basis for the district heating, the heat transferred to the electrolyte, is summarized in table 8.11. The procedure for calculating the heat transferred to the district heating, and the heat which is lost in the heat transfer and to the surroundings are accounted for over the next paragraphs.

	Energy	**2030** $(\frac{GWh}{year})$	**2050** $(\frac{GWh}{year})$
In	$\dot{Q}_{\text{AFC}}$	22,8	15,4
Out	$\dot{Q}_{\text{Electrolyte}}$	21,7	14,6
	$\dot{Q}_{\text{Loss (AFC)}}$	1,14	0,77

Table 8.11: Summary of the energy basis for the district heating

The heat transferred by the heat exchanger towards water in the district heating given by equation 8.71.

$$\dot{Q}_{\text{HE}} = \dot{m}_{\text{Electrolyte}} * C_{p_{\text{Electrolyte}}} * (T_{\text{AFC}} - T_{\text{District heating}}) \tag{8.71}$$

Where $\dot{Q}_{\text{HE}}$ is the heat transferred by the heat exchanger, $\dot{m}_{\text{Electrolyte}}$ is the mass flow of the electrolyte, $C_{p_{\text{Electrolyte}}}$ is the specific heat capacity of the 35%wt. KOH/water electrolyte solution and T_{AFC} and $T_{\text{District heating}}$ is the temperature of the AFC- and district heating operating temperature respectively.
The heat which is successfully transferred to the water of the district heating is expressed through equation 8.72.

$$\dot{Q}_{\text{DH}} = \eta_{\text{HE}} * \dot{Q}_{\text{HE}} \tag{8.72}$$

Where η_{HE} is the heat exchanger efficiency of 0,9. The losses in the process are then described by equation 8.73.

$$\dot{Q}_{\text{Loss (HE)}} = \dot{Q}_{\text{HE}} - \dot{Q}_{\text{DH}} \tag{8.73}$$

Where $\dot{Q}_{\text{Loss (HE)}}$ is heat which is lost by the heat exchanger. The heat remaining in the electrolyte led to the reservoir, where it is transferred to its surroundings. The heat transferred in this process has the notation $\dot{Q}_{\text{Ambient}}$, and is given in equation 8.74.

$$\dot{Q}_{\text{Ambient}} = \dot{Q}_{\text{Electrolyte}} - \dot{Q}_{\text{HE}} \tag{8.74}$$

Electricity

The mechanical power needed to elevate the electrolyte to the AFC's operating pressure and flow, is stated through equation 8.75.

$$P_{\text{Pump}} = p_{\text{Syst.}} * \dot{V}_{\text{Electrolyte}} \tag{8.75}$$

Where P_{Pump} is the mechanical power the pump provides to the electrolyte, $p_{\text{Syst.}}$ it the AFC's operating pressure of 2,2 bar and $\dot{V}_{\text{Electrolyte}}$ is the volumetric flow rate of the Electrolyte which is calculated to 12,6 l/s in 2030 and 8,5 l/s in 2050.[107]
To estimate the electric power needed, the pump's mechanical power is divided by the efficiencies of the pump and electric motor, as stated in equation 8.76.

$$P_{\text{El.}} = \frac{P_{\text{Pump}}}{\eta_{Pump} * \eta_{Motor}} \tag{8.76}$$

Where $P_{\text{El.}}$ is the electric power drawn by the pump and η_{Pump} is the pump efficiency, assumed to be 0,85 and η_{Motor} is the electric motor efficiency. The electric motor is an induction motor, which could have an assumed efficiency of 0,95.[108]
Through calculations in excel, *the electric power needed by the pump* is estimated to be *3,43 kW in 2030* and *2,31 kW in 2050.* This amounts to a yearly energy consumption of *0,0150 GWh/year in 2030* and *0,0101 GWh/year in 2050.*

8.9 Power conditioner

The power conditioning system consists of two systems, an electric and a chemical, which contributes in making the AFC rigid as a power supply, and able to provide the requested power when it is needed.
The electric system consists of a boost converter, a power inverter, a battery and two diodes, as seen in figure 8.8. The power produced by the fuel cell is unstable in terms of voltage and current output, as it is dependent on a series of variables as presented in section 8.4.3. The boost converter increases and stabilizes the direct current emitted by the AFC. The stable direct current can be stored in the battery, and forms a basis for the power inverter to convert the direct current to 50 Hz alternating current through pulse width modulation.[74]
The chemical system consists of a fuel storage tank, a compressor and a servo valve which can be precisely controlled to deliver the fuel flow needed to keep a constant operating pressure for the fuel cell. As it is fueled by surplus fuel from the AFC, the thermal process of the ammonia cracker has a long response time due to an increase in ammonia flow will cause a decrease in temperature in the reaction chamber. To enable a smooth ramping in the H_2 production for the ammonia cracker, H_2-mixture is fed from the storage to the AFC through the servo valve.
The electric energy produced by the system as alternating current, E_{AC}, is described by equation 8.77.

$$E_{\text{AC}} = E_{\text{AFC}} * \eta_{\text{DC/DC}} * \eta_{\text{DC/AC}} \tag{8.77}$$

Where E_{AFC} is the energy produced by the AFC, which is 39,1 GWh/year in 2030 and 26,4 GWh/year in 2050. The efficiency of the boost converter, $\eta_{\text{DC/DC}}$, is listed to be 0,95 by Jovcic in 2009 for megawatt size applications. The efficiency of the inverter is

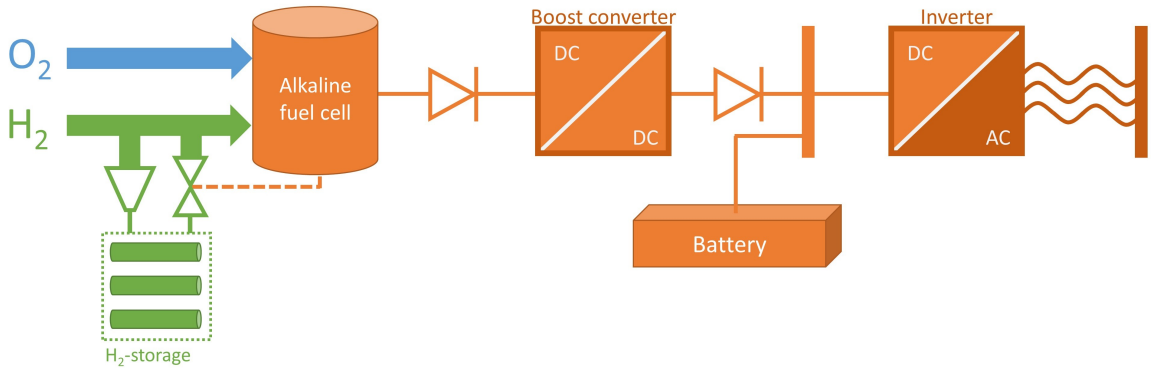

Figure 8.8: Schematic for the power conditioning system

represented by $\eta_{DC/AC}$, and ABB states that their megawatt size solar transformer has an efficiency of 0,97, including transforming to correct AC voltage.[109] [110]
The alternating electric energy output is calculated to be *36,0 GWh/year in 2030* and *24,3 GWh/year in 2050*. The energy which is not transformed to alternating electric energy is transformed to heat, and is calculated to be 3,1 GWh/year in 2030 and 2,1 GWh/year in 2050.

Fuel storage system

The set volume for the storage tank is 10 m^3, and the gas pressure is set 100 bar. The AFC is fed a fuel mixture, where H_2 amounts to 73,6 vol% of the gas volume. The volume of H_2 in the gas is expressed through equation 8.78.

$$V_{H_2} = V_{\text{tank}} * X_{H_2} \tag{8.78}$$

Where V_{H_2} is the volume of the H_2 occupies in the storage tank, V_{tank} is the volume of the storage tank and X_{H_2} is the volume fraction of H_2 in the fuel mix.
The mass of the stored H_2, m_{H_2}, is then described by through the density for H_2 at 100 bar, $\rho_{H_2@100\text{ bar}}$, which is 7,8 kg/$m^3$. The mass of the H_2 in the tank is described by equation 8.79.[21]

$$m_{H_2} = V_{H_2} * \rho_{H_2@100\text{ bar}} \tag{8.79}$$

The chemical energy of the H_2 stored in the tank is described with equation 8.80.

$$E_{\text{Chemical}} = m_{H2} * LHV_{H_2} \tag{8.80}$$

Where E_{Chemical} is the chemical energy of the H_2, and LHV_{H_2} is the lower heating value of the H_2, which is 120 MJ/kg.
The alternating electric energy, E_{Electric}, produced by the stored H_2 is calculated by multiplying the chemical energy with the efficiencies of the AFC, boost converter and inverter, as seen in equation 8.81.

$$E_{\text{Electric}} = E_{\text{Chemical}} * \eta_{\text{AFC}} * \eta_{DC/DC} * \eta_{DC/AC} \tag{8.81}$$

Where η_{AFC} is the efficiency of the fuel cell, which is calculated to be 0,44 in section 8.4.3.
The alternating electric energy stored in the storage tank equals 776 kWh. If the system experience an increased power need by 2 MW, and the storage tank is full, the storage

system gives the ammonia cracker over 23 minutes to reach steady-state.
For further adjustments, the electric energy density of the H_2 mixture in the storage tank, e_{Electric}, can be used to easily dimension the storage tank, and is stated in equation 8.82.

$$e_{\text{Electric}} = \frac{E_{\text{Electric}}}{V_{\text{tank}}} \tag{8.82}$$

The alternating electric energy density of the H_2-mixture at 100 bar storage pressure, is calculated to be 77,6 kWh/m^3.

Compressor energy
A compressor is used to increase the pressure of the H_2-mixture from the operating pressure of 2,2 bar to 100 bar. As the occurrence of large power increases in the grid is seldom, it is assumed that the time used to fill the storage tank is 24 hours and that the compression process is polytropic. The polytropic index, n, for H_2 is stated to be in the range of 1,28 to 1,35 by Luo et al., and is assumed to be 1,3 for the fuel mixture.[111]
The specific work, $w_{\text{poly.}}$, needed for the H_2-mixture to undergo a polytropic compression is stated in equation 8.83.[112]

$$w_{\text{poly.}} = \frac{n}{n-1} * R * T_1 * \left(\left(\frac{p_2}{p_1} \right)^{\frac{n-1}{n}} - 1 \right) \tag{8.83}$$

Where n is the polytropic index, R is the gas constant, T_1 is the temperature of the H_2-mixture entering the compressor and p_1 and p_2 is the pressure of the H_2-mixture in and out of the compressor respectively.
By multiplying the specific work of the polytropic compression with the yearly mass flow, $\dot{m}_{\text{gas}}$, the energy supplied by the compressor, $E_{\text{compressor}}$, can be stated as seen in equation 8.84.

$$E_{\text{compressor}} = \dot{m}_{\text{gas}} * w_{\text{poly.}} \tag{8.84}$$

The compressor is assumed to have an efficiency, $\eta_{\text{compressor}}$, of 0,9, and the electric induction motor driving it is assumed to have an efficiency, η_{motor}, of 0,95. The electric energy, $E_{\text{el. comp.}}$ consumed by the motor is stated in equation 8.85.

$$E_{\text{el. comp.}} = \frac{E_{\text{compressor}}}{\eta_{\text{compressor}} * \eta_{\text{el. motor}}} \tag{8.85}$$

The electric energy consumed by the H_2 compression is calculated to be *0,0014 GWh/year.*

Battery

The response time of an alkaline fuel cell is stated by Weydahl to be in the range from 10 milliseconds to 10 seconds, depending on initial and final cell voltages. In some scenarios, significant voltage ripples were observed, which interfered with the AFC's steady-state operation for as long as 200 seconds after the initial step up in needed effect. On this basis, the response time for the AFC, based on the charge transfer reaction at the cathode, is set to 100 seconds. The energy which must be delivered by the battery, $E_{batterydelivered}$, to the system is given through equation 8.86.[70]

$$E_{\text{battery delivered}} = P_{\text{increase}} * t_{\text{response}} \tag{8.86}$$

Where $P_{increase}$ is the increase in electric effect, which is 2 MW, and $t_{response}$ is the maximum response time of the AFC, which is set to 100 seconds. *The electric energy which must be supplied by the battery* is calculated to be *55,6 kWh*.
The efficiency of unloading for the battery, $\eta_{battery}$ is assumed to be 90%, and the needed battery capacity is stated in equation 8.87.

$$E_{\text{battery capacity}} = \frac{E_{\text{battery delivered}}}{\eta_{\text{battery}}} \tag{8.87}$$

The capacity of the battery is calculated to be *61,7 kWh*.

8.10 Pumps, compressors and fans

Pumps

The power a pump generates on its working medium is described in equation 8.88.[113]

$$P_{\text{pump}} = \Delta p * \dot{V} \tag{8.88}$$

Where P_{pump} is the effect, Δp is the working mediums pressure increase and $\dot{V}$ is the volume flow of the medium. The electric energy needed to drive the pump is given in equation 8.89.

$$P_{\text{el. pump}} = \frac{P_{\text{pump}}}{\eta_{\text{compressor}} * \eta_{\text{el. motor}}} \tag{8.89}$$

Where $\eta_{\text{compressor}}$ is the efficiency of the compressor, assumed to be 0,85, and $\eta_{\text{el. motor}}$ is the efficiency of the electric motor and is assumed to be 0,95
Under steady operating conditions, the energy consumed by the pump is given by multiplying with the 4380 operating hours in a year.

Compressors

The specific polytropic work, $w_{\text{poly.}}$, needed to increase the pressure of a gas is given through equation 8.90.[112].

$$w_{\text{poly.}} = \frac{n}{n-1} * R * T_1 * \left(\left(\frac{p_2}{p_1} \right)^{\frac{n-1}{n}} - 1 \right) \tag{8.90}$$

Where n is the polytropic index of the gas which is compressed. The gas constant is represented by R, T_1 is the temperature of the entering gas and p_2 and p_1 is the pressure of the gas exiting and entering respectively.
The energy supplied by the compressor, $E_{\text{compressor}}$, to the gas stream is given by multiplying the specific polytropic work with the mass flowing through the compressor in a year, $\dot{m}_{\text{gas}}$, as stated in equation 8.91.

$$E_{\text{compressor}} = \dot{m}_{\text{gas}} * w_{\text{poly.}} \tag{8.91}$$

The electric energy needed to drive the pump, is stated in equation 8.92.

$$E_{\text{el. comp.}} = \frac{E_{\text{compressor}}}{\eta_{\text{compressor}} * \eta_{\text{el. motor}}} \tag{8.92}$$

Where $\eta_{\text{compressor}}$ is the efficiency of the compressor, stated to be 0,9 by Fossmark.[114]

Fans

The mechanical effect needed to move air into the system is expressed through equation 8.93.

$$P_{\text{fan}} = \Delta p_{\text{air}} * \dot{V}_{\text{air}} \tag{8.93}$$

Where Δp_{air} is the air's pressure increase through the fan and $\dot{V}_{\text{air}}$ is the air's volume flow. The electric effect needed to drive the fan is stated in equation 8.94. Fossmark states that the pressure increase caused by a fan is in the range between 200 and 9000 Pa, and is selected depending on the application. As the air passes through the MEA-solution of the CO_2-scrubber, it is assumed that the air pressure needs to be in the higher end of the range spectrum, and a pressure increase of 7000 Pa is assumed.
The electric effect needed to drive the fan is expressed in equation 8.94.

$$P_{\text{el. fan}} = \frac{P_{\text{fan}}}{\eta_{\text{fan}} * \eta_{\text{el. motor}}} \tag{8.94}$$

Where η_{fan} is the efficiency of the fan, Fossmark states that 0,85 is a common value for both axial-flow and centrifugal fans.[79]
Under steady operating conditions, the energy consumed by the pump is given by multiplying with the 4380 operating hours in a year.

Total

The complete overview of the electric energy consumed by the fan, compressor and pumps, is stated in table 8.12.

Type	**Medium**	**2030** $(\frac{GWh}{year})$	**2050** $(\frac{GWh}{year})$
Fan	Air	0,218	0,147
Compressor 1	H_2-mixture	0,182	0,123
Compressor 2	H_2-mixture	0,183	0,123
Compressor 3	Air-mixture	0,489	0,329
Compressor 4	Air-mixture	3,31	2,23
Compressor 5	H_2-mixture	0,0014	0,0014
Pump 1	Ammonia	0,0009	0,0006
Pump 2	MEA-solution	0,00001	0,00001
Pump 3	KOH-solution	0,015	0,010
Total	-	4,39	2,96

Table 8.12: Summary of the electric energy consumed by the electric motors driving

8.11 Total system

The AFC-system is a combined heat and power plant, taking the chemical energy of the H_2, stored in ammonia, and converting it to electricity and heat, as seen in the schematic of 8.9. It provides heat for the district heating system, which has three stated viable scenarios, at operating temperatures of 60°C, 80°C and 120°C. Over the following subsections, the AFC-system's heat and electric energy output for these scenarios are accounted for.

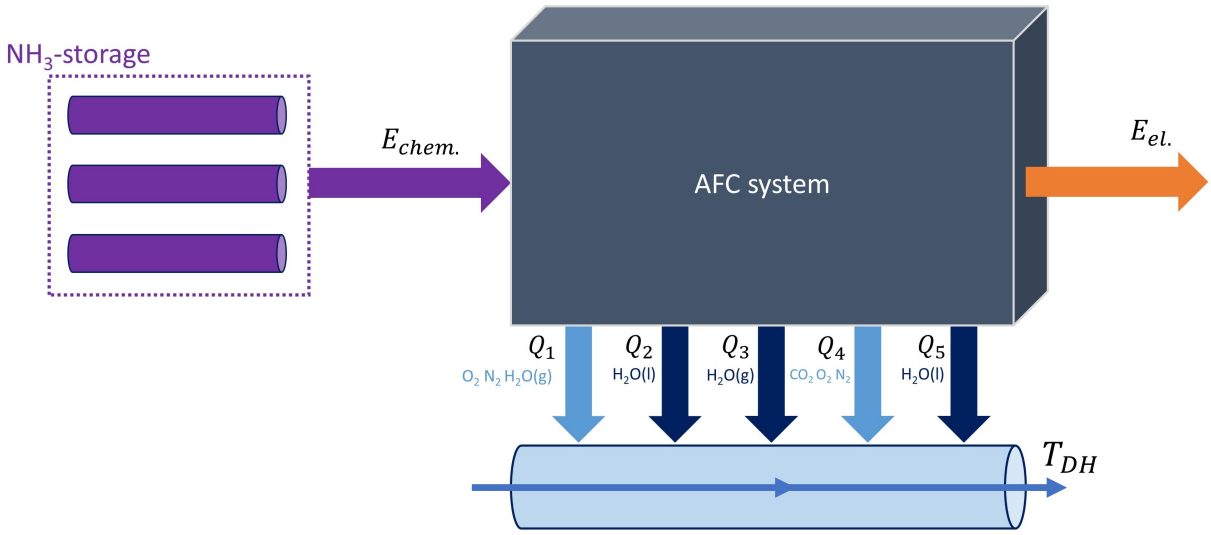

Figure 8.9: Simplified schematic for the energy balance of the complete system. System losses are not shown.

Electric energy

The electric energy available for the Longyearbyen settlement is the electric energy produced by the AFC minus the electric energy needed to cover the systems internal consumption, as stated in equation 8.95.

$$E_{\text{Output}} = E_{\text{AFC}} - E_{\text{Internal}} \tag{8.95}$$

The electric energy output of the system is calculated to be *31,62 GWh/year* in 2030 and *21,32 GWh/year* in 2050, having an electric efficiency of 0,355 in both 2030 and 2050.

District heat

Through figure 8.9, it is evident that five different heat source contributes to the system's total heat output. The various heat contributions, and their notations, are summarized in table 8.13, and their equations are accounted for over the next paragraphs. The efficiency for all heat transfers, η_{HT}, is assumed to be 0,9.

Notation	Origin
$\dot{Q}_1$	Heat derived from the exhaust gas of the ammonia cracker. The gas assumed to be at atmospheric pressure, meaning its containing water condensates at 100°C.
$\dot{Q}_2$	Heat derived from the liquid water separated from the anode gas stream.
$\dot{Q}_3$	Heat derived from the condensation of water in the anode gas stream.
$\dot{Q}_4$	Heat derived from the air-mixture exiting the CO_2-scrubber.
$\dot{Q}_5$	Heat derived from the electrolyte stream.

Table 8.13: Operational parameter values and mass flow for the regenerator

The heat derived from the ammonia cracker's exhaust gas, $\dot{Q}_1$, is given by either equation 8.96 or 8.97. Equation 8.96 is used when the working temperature of the district heating

is 100°C or more, while equation 8.97 takes account for the condensing water, and its further temperature decrease, and is used for temperatures lower than 100 °C.
The derived heat at operating temperatures above 100 have been calculated through equation 8.96.

$$\dot{Q}_{1_{T_{DH} > 100°C}} = \eta_{HT} * \dot{m}_{exhaust} * C_{p_{combined,\ H_2O(g)}} * (T_{exhaust} - T_{DH}) \tag{8.96}$$

Here, $\dot{m}_{exhaust}$ is the total mass of the exhaust gas, $C_{p_{combined,\ H_2O(g)}}$ is the gas' combined specific heat with the water in gaseous state and $T_{Exhaust}$ and T_{DH} is the temperature of the exhaust gas and the district heating respectively. The temperature of the exhaust gas is assumed to be 125°C.
For district heating temperatures below 100°C, the heat derived from the exhaust gas is calculated through equation 8.97.

$$\begin{aligned}\dot{Q}_{1_{T_{DH} < 100°C}} =& \eta_{HT} * (\dot{m}_{exhaust} * C_{p_{combined,\ H_2O(g)}} * (T_{exhaust} - 100°C) \\ &+ \dot{m}_{H_2O\ (g)} * L_{H_2O} + \dot{m}_{exhaust} * C_{p_{combined,\ H_2O(l)}} * (100°C - DH))\end{aligned} \tag{8.97}$$

Where $\dot{m}_{H_2O\ (g)}$ is the mass of the condensing water, L_{H_2O} is the latent heat of water and $C_{p_{combined,\ H_2O(l)}}$ is the mixture's combined specific heat when the water is in liquid form.
The heat derived from the liquid water which is separated from the anode gas stream is stated in equation 8.98.

$$\dot{Q}_2 = \eta_{HT} * \dot{m}_{H_2O(tot)} * C_{p_{H_2O}} * (T_{H_2O} - T_{DH}) \tag{8.98}$$

Where $\dot{m}_{H_2O(tot)}$ is the mass of the water leaving the anode, $C_{p_{H_2O}}$ is the specific heat of water and T_{H_2O} is the temperature of the water which is 125°C.
The heat derived from the condensing water leaving the anode is stated in equation 8.99.

$$\dot{Q}_3 = \eta_{HT} * m_{H_2O(g)} * L_{H_2O} \tag{8.99}$$

Where $m_{H_2O(g)}$ is the mass flow of water in gaseous state.
The heat derived from the air-mixture exiting the CO_2-scrubber is stated in equation 8.100.

$$\dot{Q}_4 = \eta_{HT} * \dot{m}_{air} * C_{p_{air}} * (T_{air} - T_{DH}) \tag{8.100}$$

Where $\dot{m}_{air}$ is the mass of air passing through the CO_2-scrubbers regenerator, $C_{p_{air}}$ is the specific heat of air and T_{air} is the temperature of the air, which is calculated to be 121,1°C.
The heat derived from the electrolyte is stated in equation 8.101.

$$\dot{Q}_5 = \eta_{HT} * \dot{m}_{electrolyte} * C_{p_{electrolyte}} * (T_{electrolyte} - T_{DH}) \tag{8.101}$$

Where $\dot{m}_{electrolyte}$ is the mass flow of the electrolyte, $C_{p_{electrolyte}}$ is the specific heat of the electrolyte solution and $T_{electrolyte}$ is the temperature of the electrolyte leaving the AFC, which is assumed to be 125°C.
The heat contributions have been calculated and summed up for the temperature range from 60-120°C in excel, and the results for district heating temperatures of 60°C, 80°C and 120°C are presented in the following paragraphs.

60°C district heating

The heat transferred to the district heating operating at 60°C, by each of the heat contributions, is stated in table 8.14.

Heat	**Medium**	**2030** ($\frac{GWh}{year}$)	**2050** ($\frac{GWh}{year}$)
1	Exhaust gas	2,80	1,89
2	Separated H_2O	1,36	0,91
3	Latent heat of H_2O	5,00	3,37
4	Air CO_2-scrubber	1,66	1,19
5	Electrolyte H_2O	10,13	6,83
Total	-	20,95	14,12

Table 8.14: Heat transferred to the district heating at a working temperature of 60°C.

If the district heating has an operating temperature of 60°C, *the heat derived from the AFC system* is calculated to be *20,95 GWh/year in 2030* and *14,12 GWh/year in 2050*. The combined heat and power, CHP, produced by the AFC system and its efficiencies are presented in 8.15.

Form	**2030** ($\frac{GWh}{year}$)	**2050** ($\frac{GWh}{year}$)	**Efficiency**
Electric	31,62	21,32	0,355
Heat	20,95	14,12	-
CHP	52,57	35,44	0,590

Table 8.15: Electric energy and heat extracted from the system with a district heating temperature of 60°C. Efficiencies are calculated in regard to the chemical input energy.

When supplying heat for a district heating system operating at *60°C*, the *CHP* is calculated to be *52,57 GWh/year in 2030* and *35,44 GWh/year in 2050*, giving a system efficiency of 0,590. The average electric power output is calculated to be *7,22 MW in 2030* and *4,87 MW in 2050*, while the average heat power output is calculated to be *4,78 MW in 2030* and *3,22 MW in 2050*.

80°C district heating

The heat transferred to the district heating, when operating at 80°C, is stated in table 8.16.

Heat	**Medium**	**2030** ($\frac{GWh}{year}$)	**2050** ($\frac{GWh}{year}$)
1	Exhaust gas	2,58	1,74
2	Separated H_2O	0,93	0,63
3	Latent heat of H_2O	5,00	3,37
4	Air CO_2-scrubber	1,11	0,75
5	Electrolyte H_2O	7,02	4,73
Total	-	16,65	11,22

Table 8.16: Heat transferred to the district heating at a working temperature of 80°C.

When operating at *80°C*, the district heating derives *16,65 GWh/year from the AFC system in 2030* and *11,22 GWh/year in 2050*. The CHP and the efficiencies of the system is presented in table 8.17.

Form	**2030** ($\frac{GWh}{year}$)	**2050** ($\frac{GWh}{year}$)	**Efficiency**
Electric	31,62	21,32	0,355
Heat	16,65	11,22	-
CHP	48,28	32,54	0,542

Table 8.17: Electric energy and heat extracted from the system with a district heating temperature of 80°C. Efficiencies are calculated in regard to the chemical input energy.

The CHP is calculated to be *48,28 GWh/year in 2030* and *32,54 GWh/year in 2050*, which leads to a system efficiency of 0,542. The average electric power output is calculated to be *7,22 MW in 2030* and *4,87 MW in 2050*, while the average heat power output is calculated to be *3,80 MW in 2030* and *2,56 MW in 2050*.

120°C district heating

The heat transferred to the district heating when its working temperature is 120°C, is stated in table 8.18.

Heat	**Medium**	**2030** ($\frac{GWh}{year}$)	**2050** ($\frac{GWh}{year}$)
1	Exhaust gas	0,045	0,030
2	Separated H_2O	0,10	0,07
3	Latent heat of H_2O	5,00	3,37
4	Air CO_2-scrubber	0,030	0,020
5	Electrolyte H_2O	0,78	0,53
Total	-	5,96	4,01

Table 8.18: Heat transferred to the district heating at a working temperature of 120°C.

When operating at *120°C*, the heat derived by the district heating is calculated to be *5,97 GWh/year in 2030*, and *4,01 GWh/year in 2050*. The CHP and the system efficiencies are presented in table 8.19.

Form	**2030** ($\frac{GWh}{year}$)	**2050** ($\frac{GWh}{year}$)	**Efficiency**
Electric	31,62	21,32	0,355
Heat	5,96	4,01	-
CHP	37,58	25,33	0,422

Table 8.19: Electric energy and heat extracted from the system with a district heating temperature of 120°C. Efficiencies are calculated in regard to the chemical input energy.

When operating at 120°C, the for the system is calculated to be *37,58 GWh/year in 2030* and *25,33 GWh/year in 2050*, while the system efficiency is calculated to be 0,422. The average electric power output is calculated to be *7,22 MW in 2030* and *4,87 MW in 2050*, while the average heat power output is calculated to be *1,36 MW in 2030* and *0,92 MW in 2050*.

9. Discussion

The discussion is organized in sections to promote the readability and train of thought

9.1 Presented system

The system presented by Longyearbyen Community Council in figure 2.1 is a concept in development. For both the Longyearbyen energy conversion project and this thesis, it was important to evaluate the system's feasibility before moving forward with calculations. The modeling study by Ringkjøb et al. showed that a stand-alone energy system based solely on local renewable energy was feasible, calling for large investments in solar PV and wind power as well as a large hydrogen production and storage, to cover for seasonal variations in power access and energy demand. As concluded in chapter 3, the cost linked with a stand-alone energy system model case, far outweighs the cost of the other model cases, which allows the import of hydrogen and the use fossil fuels.
At the time of writing, the energy modeling study by Ringkjøb et al. is the only known attempt to test for the feasibility of a stand-alone system solely based on local renewable power. There is no reason to question the results of the study. Its scaling of solar PV, wind power and hydrogen storage correlates with the fluctuations seen in both the renewable power access and energy demand in Longyearbyen. The only event that could have changed the result of the study in favor of the concept system, was if renewable sources which are not included in the study, such as hydropower from a remote location on Svalbard, proved to be viable, which is regarded as highly unlikely.
As costs are assumed to be of high priority when Longyearbyen's future energy system is implemented, the system concept provided by Longyearbyen Community Council is not financially viable.

9.2 Modeling study

Ringkjøb et al. applied the techno-economic framework TIMES for modeling the future energy system of Longyearbyen. TIMES, with its split engineering and economic approach, will produce the lowest cost energy system, based on estimated cost development and probable technology development. There are a range of other energy modeling frameworks, often specializing in certain niches, like HYDROGEMS, which is a framework for the simulation of integrated hydrogen energy systems, particularly renewable energy based stand-alone power systems. HOMER is another framework, coming with multiple extensions pack, one of which is similar to TIMES techno-economic approach was utilized to model similar arctic settlements Grimsey, Iceland. The fact is, different frameworks given the same data input is very likely to present two different solutions to the same problem, as the frameworks are set to favor different aspects in a simulation. With this

said, the quality of the data given to the framework is highly important for the feasibility of the generated solution.[115]
An interesting result of the modeling study done by Ringkjøb et al. is that if a small portion of fossil energy is allowed in the energy mix, it would reduce the total cost of the system immensely, as visualized in figure 9.1.

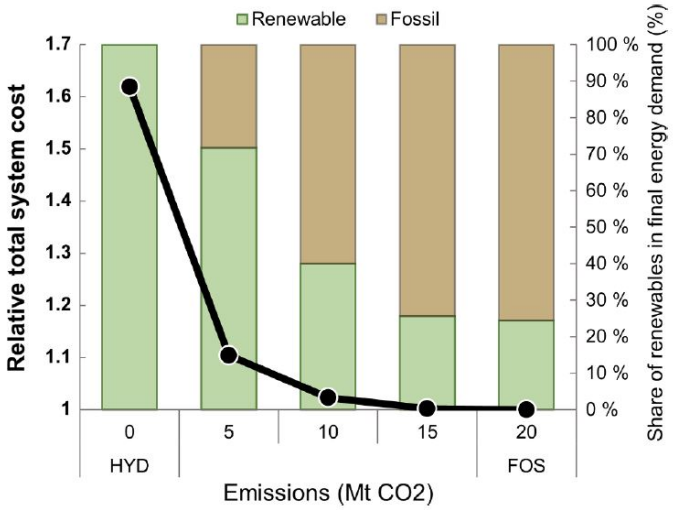

Figure 9.1: The impact of allowing CO_2-emissions on the total system cost[19]

If a yearly CO_2-emission of 5 megatonnes was tolerated, equaling a 25% share fossil energy in the fuel mix, it would result in a relative system cost reduction of 50%. At emissions larger than 5 megatonnes, the gain in cost reduction decrease rapidly. At the same time, it should be stated that the value of making the arctic settlement of Longyearbyen fully based on renewable energy could be seen as a worldwide milestone, and an important step in the shift towards a green economy.
At the same time, this project can serve as a milestone for the implementation of hydrogen- and ammonia-based technology on a global scale, as it would be a steady consumer of 10000-15000 tonnes of green or blue ammonia yearly. With this in mind, the argument for the addition of a fossil fuel-based solution in the energy mix to lower the cost of the project appears narrow-minded. The proof of hydrogen and ammonia being viable options for projects of this scale could provide large ripple-effects for an industry on the brink of massive expansion, as means of mass production would contribute to lowering prices for renewable, hydrogen-based projects worldwide.

9.3 Large-scale storage and method for power generation

With ammonia selected as method for hydrogen storage, it provides the basis for a wide range of technologies that can be utilized for energy generation. Gas-turbines, piston engines and direct ammonia fuel cells have already been discussed, and their technological development should be watched carefully in the years to come.
Lately, the possibility of producing ammonia directly from off-shore wind has emerged. ZEEDS, a consortium established where Equinor, Kværner and Aker Solutions among others, are set to provide a solution that provides the continuous production and storage

of ammonia at open seas in relation with the shipping industry. This type of solution should be seen as a possibility for ammonia production near Longyearbyen, even producing ammonia specifically for the settlement.[116]
It should also be mentioned that a small-scale thorium power plant would be very favorable in regards to its small footprint per kilowatt-hour. Solar PV and wind power will occupy large areas, which will be harmful to the local wildlife.

9.4 Selected system and its technologies

The selected system is an adaptation of a fuel cell city car system developed by Karl Kordesch in the 1970s. To be utilized in Longyearbyen, it is assumed that the 6 kW system can be linearly scaled up, without the addition of supplementary components or major design changes being made. The adapted system is calculated to have an average electric power output of 7,22 MW in 2030, which gives that system needs to be scaled up by a factor of at least 1200. With no detailed reference systems available, it is hard to say for certain if the AFC-system by Kordesch is capable of a linear scale-up of such an extent. Through the work with this thesis, no data have been found discussing that AFC-systems must take special precautions when being scaled up, or reaching a certain size of power output. With no data stating the opposite, it is assumed that AFC-system by Kordesch can handle a scale-up.

During the late stage of working with this thesis, a work note presented to the Ministry of Petroleum and Energy by Statkraft and Sintef Industri was found. The work note intended to present an alternative to a feasibility study conducted by THEMA and Multiconsult, which concluded with an LNG power plant and the addition of small amounts of solar PV as the most favorable solution for the settlement. The work note by Statkraft and Sintef Industri introduces the possibility of using hydrogen produced from wind power on Varangerhalvøya in eastern Finnmark to serve as an energy supply for Longyearbyen. Further, the work note focus' on the economic aspects of various types of hydrogen storage, the employed technologies are compressed hydrogen, liquefied hydrogen, methanol and ammonia, concluding with ammonia being the most suited and economically viable option. As for the energy production from ammonia, the work note suggests using a 10 MW direct ammonia SOFC combined with a 10 MW gas turbine. Emphasizing that the preferred solution over time being fuel cell technology.[117][118][119]
The system presented in the work note is the only statement found throughout this process, that suggests an energy system for a scenario where ammonia is imported to Longyearbyen. In retrospect, the system in the work note, along with articles regarding a prototype for a direct ammonia SOFC and ammonia fueled gas turbines, should have been used as a reference system. In the work note, yearly ammonia import to Longyearbyen is calculated to 26 500 tonnes, compared with 15 037 tonnes calculated from energy demand given by Ringkjøb et al. The deviation is assumed to be caused by differences in energy modeling, such as constrains or available energy technologies.

By ensuring sufficient oxygen levels to improve the slow reaction rate of the cathode, the AFC is fueled with twice the theoretic air need, surplus air is then used for combustion in the ammonia cracker and as flush gas of the CO_2-scrubber. The fact is, only 13 mass% of the surplus air is used for combustion. This means that 43,5 mass% of the air entering the system through the fan, passing through the CO_2-absorber, getting is

compressed to 2,2, before consuming heat from the condensing heat exchanger to reach the operating temperature of the AFC. In return it transfers a small amount of heat to the CO_2-regenerator before being applied to the district heating.
With the compression of incoming air being by far the largest internal electric energy consumption of the system, and the latent heat of the anode exhaust gas being one of the biggest source of heat in the system, the excess air moved through the system leads substantial internal energy losses.
In further work, the amount of air let into the system should be optimized for the cathode to have a steady reaction rate, proper operation of the AFC, while keeping the internal electricity and heat consumption due to air compression and heating to a minimum. This would probably improve the total system efficiency of several percent. The use of an air separation unit, to removing nitrogen from the air should be considered, as it would lead to a further decrease of the internal losses.
A report commissioned by The Norwegian Environment Agency set to provide basic information in climate change adaption in Svalbard, states that permafrost warming and thawing may strongly affect the rock stability, which could trigger large scale rockslides. Another typical landslide phenomenon in arctic environments with thawing permafrost is quick clay slides, which typically occurs in relatively flat terrain. With Longyearbyen being situated at Adventelva's outlet to Isfjorden, and parts of the settlement extending along the valley of Adventsdalen, Longyearbyen might be exposed to the emerging risk of both clay and rock slides. This calls for the possibility that parts of the settlement might need to be relocated in the coming years, which points towards a modular energy system is advantageous in case of a sudden relocation is needed.[120]

9.5 System components

Ammonia storage

With the possibility of ammonia being delivered in a single shipping, its time of delivery becomes crucial. If the ammonia arrives weeks in advance, this would result in large needs for cooling, which is highly unfavorable for a small energy system such as Longyearbyen. In the technological review performed by Andersson et al, salt cavity storage is referred to as a successful, low-cost method for storing compressed hydrogen. For future work, the possibility of storing compressed hydrogen in nearby decommissioned coal mines should be looked into.[21]

Heat exchangers

For the heat exchanger calculations, a simplified version of the effectiveness-NTU method has been applied, with a heat transfer effectiveness of 0,9 for all heat exchangers. This is regarded to be a sufficient approximation, but the real effectiveness of the heat transfer will vary with materials, gas-mixtures and gas velocities. In further work the LMTD-method should be applied to determine the size needed for each heat exchanger to realize the prescribed temperatures at set flow rates.[121]
The assumption that all the water is separated from the H_2-mixture in the condensing heat exchanger is a simplification that may affect the efficiency of the system significantly. In real life, a small share of the water will remain in gaseous state, and end up lowering the heat released in the combustion of the H_2-mixture in the ammonia cracker. This

simplification should be accounted for in further work.
The assumption of 50% of the ammonia being in gaseous state before entering the vaporizing heat exchanger is regarded as plausible, as the electrical energy not converted to mechanical energy by the pump is converted to heat in the ammonia.

Ammonia cracker

The reactor was simplified by assuming the temperature to be evenly distributed at 600°C under operation. In real life, the temperature will vary throughout the reactor, making the decomposition occur at different rates in the different areas of the reactor. Making it important that the heat from the combustion is evenly distributed throughout the reactor.[122]
The combustion of ammonia and hydrogen with large amounts of nitrogen present will cause NOx to form. In further design revisions, a selective catalytic reactor should be added, and the formation of the highly active greenhouse gas nitrous oxide (N_2O) must be avoided by all means.
The selection of catalyst for the ammonia cracker could prove to have a solid impact on the system as a whole. The catalyst determines the cracker's needed operating temperature, and the use of noble metals such as Ruthenium with a surface of CeO_2 makes ammonia decomposition viable at a temperature of 450°C, see figure 6.3. Further work should look into the cracker catalyst's effect on the total system efficiency, and a cost-benefit analysis should be provided.
For future design revisions, the feasibility of a big scale membrane reactor should be researched. A membrane reactor enables the splitting of nitrogen and hydrogen in the reactor chamber, which could lead to significant improvements regarding internal energy losses and efficiency.

Alkaline fuel cell

With both hydrogen and oxygen being components of gas-mixtures, clogging of the electrodes could be a problem for the AFC. On the anode side, hydrogen molecules constitutes 75 mol% of the gas-mixture, and are tiny compared to nitrogen- and ammonia molecules, making it viable to assume that clogging on the anode side will not be a cause for significant voltage loss. On the cathode side, the air mixture constitutes of 21 mol% oxygen, and with nitrogen molecules being of roughly the same size as oxygen molecules, it is understandable that oxygen molecules are in hard competition for a place in the porous matrix. To avoid clogging of the cathode, which could lead to the AFC having slow reaction times, further design revisions should look into the addition of an air-separating unit, for the AFC to be fed with pure oxygen.

CO_2-scrubber

As of today, continous CO_2-scrubbing systems are still a field of development, and for further works an extensive literature research should be peformed.
To avoid CO_2 building up in the MEA-solution, it is very important that the regeneration process is nearly 100% successful before the MEA-solution re-enters the absorber column. For further design revisions an extensive regeneration system should be considered. This could be that part of MEA-solution is recirculated from the reservoir through the regenerator, or that the MEA-solution flows through multiple regeneration columns before

reaching the reservoir.
The air-mixture flow transferring heat to the regenerator is considered as massive compared to the MEA-flow. For a real life implementation, a heat transferring fluid must probably be used for practically feasible.
Since the reservoir is situated outdoors in an arctic climate, the addition of anti-freeze liquids in the MEA-solution is a must for real life implementation.

Electrolyte system

An issue regarding the sizing of needed mass for the KOH-solution is that it is only dimensioned by the heat given from the electrolyte. For the AFC to receive the proper cooling, the KOH-solution needs enough time to cool in the reservoir. In further works, an estimation for the mass of KOH-solution to achieve the desired temperature is needed.

Power conditioner

The selected storage technologies for short-time fluctuations in energy demand are a lithium-ion battery and a compressed H_2-mixture storage tank. Another technology capable of answering to short-time power increase is the flywheel, and could be considered in future design revisions of the system.
For further works, a cost-risk analysis should be performed to find the critical point of sudden load change, for the battery and short time hydrogen storage to be sized accordingly. As an example, the cost of a system capable of withstanding a 1 MW leap in energy demand, is highly in-linear with a system that can withstand 2 MW. This would be an important topic in further works of the thesis.
With the Longyearbyen energy system potentially being based upon large shares of solar PV and fuel cells, and the load-side of the grid containing few rotating masses, the widespread utilization of DC-voltage for power distribution could be considered. Small DC-grids have been used in major solar PV projects throughout Africa, and has proved its worth, for systems without large shares of rotating masses.
To improve the efficiency of this system further, it is essential to find low-temperature applications for the remaining heat after the district heating has had its share. This could be anti-freezing applications, which are plentiful throughout Longyearbyen.

10. Conclusion

The concept energy system proposed by the Longyearbyen Community Council was deemed unfit for the application, due to a modelling study by Ringkjøb et al. proving it to be highly cost-intensive. Based on a review of large-scale hydrogen storage technology conducted by Andersson et al., ammonia was selected as the preferred form for hydrogen storage, and an alkaline fuel cell system by Kordesch was adapted for combined power and heat generation. The calculations were based on a hydrogen import estimation of 89 GWh and 60 GWh worth of hydrogen in 2030 and 2050 respectively, made by Ringkjøb et al. in the modelling study. The combined electric energy and heat output of the alkaline fuel cell system, when operating at set district heating temperatures, are summarized in table 10.1, along with the efficiencies.

	60°C		**80°C**		**120°C**	
Form	**2030**	**2050**	**2030**	**2050**	**2030**	**2050**
Electric	31,62	21,32	31,62	21,32	31,62	21,32
Heat	20,95	14,12	16,65	11,22	5,96	4,01
CHP	52,57	35,44	48,28	32,5	37,58	25,34
Efficiency	*0,59*	*0,59*	*0,54*	*0,54*	*0,42*	*0,42*

Table 10.1: Summary of calculated energy production for 2030 and 2050, with basis in operating temperatures of the district heating. All values have the denomination $\frac{GWh}{year}$, except values in *italic*, which are dimensionless.

This thesis adds to the point that converting the Longyearbyen energy system to be solely based on renewables is feasible, and by importing hydrogen in the form of ammonia from the mainland, costs can be cut significantly.
The proposed further work based on this thesis is predominantly to look into other, state of the art technologies for power generation from ammonia. Primarily systems that are modular and can be transported easily, as the thawing permafrost can cause both rockslides and clayslides near the Longyearbyen settlement. For the AFC system developed in this thesis, optimization of internal energy loss should be the main focus during further work. Minor design changes can provide a significant increase in system efficiency.

Bibliography

[1] Nils Petter Thuesen and Susan Barr. Svalbard – store norske leksikon. https://snl.no/Svalbard, April 2020.

[2] Trond Meyer Smith and Susan Barr. Longyearbyen – store norske leksikon. https://snl.no/Longyearbyen, January 2020.

[3] Lars Egil Mogård Rune N. Andreassen and Petter Strøm. Det ligger rundt 10 millioner tonn kull igjen i gruvene – i dag ble svea nord-gruva låst. https://www.nrk.no/tromsogfinnmark/svea-nord-gruva-pa-svalbard-ble-onsdag-offisielt-stengt-og-las-1.14928672, March 2020.

[4] Jan A. Holtet. Eiscat svalbard radar – store norske leksikon. https://snl.no/EISCAT_Svalbard_Radar, March 2020.

[5] Magnar Gulliksen Johnsen. Svalbard satellittstasjon – store norske leksikon. https://snl.no/Svalbard_satellittstasjon, February 2020.

[6] Kent Roar Nybø. Ll ber staten ta hele regningen. https://svalbardposten.no/ber-staten-ta-hele-regningen/19.10866, March 2020.

[7] THEMA Multiconsult. Alternativer for framtidig energiforsyning på svalbard, chapter 2.3.1, p. 19-21. https://www.regjeringen.no/contentassets/cdaceb5f6b5e4fb1aa4e5e151a87859a/thema-og-multiconsult---energiforsyningen-pa-svalbard.pdf, June 2018.

[8] Christopher Engås Svalbardposten. Reservekraft til 59 millioner. https://svalbardposten.no/reservekraft-til-59-millioner/19.11144, June 2019.

[9] THEMA Multiconsult. Alternativer for framtidig energiforsyning på svalbard, chapter 2.3.3, p. 23-24. https://www.regjeringen.no/contentassets/cdaceb5f6b5e4fb1aa4e5e151a87859a/thema-og-multiconsult---energiforsyningen-pa-svalbard.pdf, June 2018.

[10] THEMA Multiconsult. Alternativer for framtidig energiforsyning på svalbard, chapter 2.3.4, p. 24. https://www.regjeringen.no/contentassets/cdaceb5f6b5e4fb1aa4e5e151a87859a/thema-og-multiconsult---energiforsyningen-pa-svalbard.pdf, June 2018.

[11] NVE Norsk vassdrags-og energidirektorat. Production and consumption of electric energy. https://www.nve.no/Media/5143/folde2011.pdf, January 2011.

[12] Ellen Synnøve Viseth Teknisk ukeblad. Longyearbyen fyrer for kråka: Bruker dobbelt så mye varme om vinteren som hus på fastlandet. https://www.tu.no/artikler/longyearbyen-fyrer-for-kraka-bruker-dobbelt-sa-mye-varme-om-vinteren-som-hus-pa-450263, 2018.

[13] THEMA Multiconsult. Alternativer for framtidig energiforsyning på svalbard, chapter 2.3.5, p. 24-25. https://www.regjeringen.no/contentassets/cdaceb5f6b5e4fb1aa4e5e151a87859a/thema-og-multiconsult---energiforsyningen-pa-svalbard.pdf, June 2018.

[14] THEMA Multiconsult. Alternativer for framtidig energiforsyning på svalbard, chapter 2.2.4, p. 16-19. https://www.regjeringen.no/contentassets/cdaceb5f6b5e4fb1aa4e5e151a87859a/thema-og-multiconsult---energiforsyningen-pa-svalbard.pdf, June 2018.

[15] Multiconsult. Feasibility study for an energy storage system for longyearbyen energiverk, chapter 2.2, p. 14-15, May 2019.

[16] THEMA Multiconsult. Alternativer for framtidig energiforsyning på svalbard, chapter 2.2.3, p. 13-16. https://www.regjeringen.no/contentassets/cdaceb5f6b5e4fb1aa4e5e151a87859a/thema-og-multiconsult---energiforsyningen-pa-svalbard.pdf, June 2018.

[17] Chungen Yin. Microwave-assisted pyrolysis of biomass for liquid biofuels production. *Bioresource technology*, 120:273–284, 2012.

[18] Energy Technology Systems Analysis Programme. Documentation for the times model, part i. https://iea-etsap.org/docs/TIMESDoc-Intro.pdf.

[19] Hans-Kristian Ringkjøb, Peter M Haugan, and Astrid Nybø. Transitioning remote arctic settlements to renewable energy systems–a modelling study of longyearbyen, svalbard. *Applied Energy*, 258:114079, 2020.

[20] Terje Aven. stokastisk – store norske leksikon. https://snl.no/stokastisk, February 2018.

[21] Joakim Andersson and Stefan Grönkvist. Large-scale storage of hydrogen. *International Journal of Hydrogen Energy*, 2019.

[22] Andrew L Dicks and David AJ Rand. *Fuel cell systems explained, chapter 10.8.1, p. 305-307.* John Wiley & Sons, 2018.

[23] Glomfjord Hydrogen. Hydrogen? glomfjord, selvfølgelig! https://www.glomfjordhydrogen.no/ac/glomfjord-hydrogen-as, June 2020.

[24] Andrew L Dicks and David AJ Rand. *Fuel cell systems explained, chapter 10.4.3, p. 277-280.* John Wiley & Sons, 2018.

[25] Europower Energi. Skal produsere hydrogen på mongstad. europower-energi.no/nyheter/skal-produsere-hydrogen-pa-mongstad/2-1-806023, June 2020.

[26] Ibrahim Dincer and Calin Zamfirescu. *Sustainable energy systems and applications, chapter 7.2, p. 204-207.* Springer Science & Business Media, 2011.

[27] Ibrahim Dincer and Calin Zamfirescu. *Sustainable energy systems and applications, chapter 7.3, p. 207-209.* Springer Science & Business Media, 2011.

[28] Jeffrey Ralph Bartels. A feasibility study of implementing an ammonia economy. 2008.

[29] Kawasaki Heavy Industries. World's first liquefied hydrogen carrier suiso frontier launches building an international hydrogen energy supply chain aimed at carbon-free society. https://global.kawasaki.com/en/corp/newsroom/news/detail/?f=20191211_3487, December 2019.

[30] Vanessa Tietze, Sebastian Luhr, and Detlef Stolten. Bulk storage vessels for compressed and liquid hydrogen. *Hydrogen Science and Engineering: Materials, Processes, Systems and Technology*, pages 659–690, 2016.

[31] Höegh LNG. Höegh lng - fleet. https://hoeghlng.com/fleet/default.aspx#section=lngc, June 2020.

[32] McDermott International. Qafco ammonia storage tanks. https://www.mcdermott.com/What-We-Do/Project-Profiles/QAFCO-Ammonia-Storage-Tanks#:~:text=They%20are%20currently%20the%20largest,tanks%20(concrete%20containment%20walls)., June 2020.

[33] Ibrahim Dincer and Osamah Siddiqui. *Ammonia Fuel Cells, chapter 4.1, p. 90-97.* Advances in Librarianship, 2020.

[34] GenCell Energy. A5™ off grid power solution | gencell. https://www.gencellenergy.com/our-products/gencell-a5/, May 2020.

[35] AFC Energy. Hydrox-cell (l)™ - afc energy. https://www.afcenergy.com/products/hydrox-cell_l/#, June 2020.

[36] Teknisk Ukeblad v/Tore Stensvold og Adrian Broch Jensen. Eidesvik skal få verdens første utslippsfrie offshore-fartøy: Bruker ammoniakk. https://www.tu.no/artikler/verdens-forste-eidesvik-bygger-om-viking-energy-til-ammoniakk-drift/483392?key=xX98Lz4k, January 2020.

[37] Pavlos Dimitriou and Rahat Javaid. A review of ammonia as a compression ignition engine fuel. *International Journal of Hydrogen Energy*, 45(11):7098–7118, 2020.

[38] Ibrahim Dincer and Osamah Siddiqui. *Ammonia Fuel Cells, chapter 8.1, p. 235.* Advances in Librarianship, 2020.

[39] Teknisk ukeblad v/Tore Stensvold. Motorprodusentene tester ammoniakk – kan gi nullutslippsskip før 2030. https://www.tu.no/artikler/motorprodusentene-tester-ammoniakk-kan-gi-nullutslippsskip-for-2030/488522?key=92fI0Ztm, March 2020.

[40] MAN Energy. Engineering the future two-stroke green-ammonia engine. `https://marine.man-es.com/docs/librariesprovider6/test/5510-0241-00web.pdf?sfvrsn=7f4dca2_6`, November 2019.

[41] Ibrahim Dincer and Osamah Siddiqui. *Ammonia Fuel Cells, chapter 8.2, p. 235-236.* Advances in Librarianship, 2020.

[42] Osamu Kurata, Norihiko Iki, Takayuki Matsunuma, Takahiro Inoue, Taku Tsujimura, Hirohide Furutani, Akihiro Hayakawa, and Hideaki Kobayashi. Success of ammonia-fired, regenerator-heated, diffusion combustion gas turbine power generation and prospect of low nox combustion with high combustion efficiency. In *ASME Power Conference*, volume 57601, page V001T04A026. American Society of Mechanical Engineers, 2017.

[43] K Kordesch. City car with h2-air fuel cell and lead-battery. *SAE Paper*, (719015), 1971.

[44] Karl Kordesch, Viktor Hacker, Josef Gsellmann, Martin Cifrain, Gottfried Faleschini, Peter Enzinger, Robert Fankhauser, Markus Ortner, Michael Muhr, and Robert R Aronson. Alkaline fuel cells applications. *Journal of Power Sources*, 86(1-2):162–165, 2000.

[45] Bjørn Pedersen. varmeveksler – store norske leksikon. `https://snl.no/varmeveksler`, September 2017.

[46] Kuppan Thulukkanam. *Heat exchanger design handbook, chapter 1.3, p. 57-84.* CRC press, 2013.

[47] Kuppan Thulukkanam. *Heat exchanger design handbook, chapter 1.4, p. 84-89.* CRC press, 2013.

[48] Yunus Cengel. *Heat and mass transfer: fundamentals and applications, chapter 11.2, p. 653-660.* McGraw-Hill Higher Education, 2014.

[49] Sébastien E Gay and Mehrdad Ehsani. Ammonia hydrogen carrier for fuel cell based transportation. *SAE transactions*, pages 1748–1773, 2003.

[50] Vyjayanthi Alagharu, Srinivas Palanki, and Kevin N West. Analysis of ammonia decomposition reactor to generate hydrogen for fuel cell applications. *Journal of Power Sources*, 195(3):829–833, 2010.

[51] Bjørn Pedersen. katalysator – store norske leksikon. `https://snl.no/katalysator`, September 2019.

[52] Ibrahim Dincer and Calin Zamfirescu. *Sustainable energy systems and applications, chapter 7.6, p. 216-218.* Springer Science & Business Media, 2011.

[53] Ilaria Lucentini, Albert Casanovas, and Jordi Llorca. Catalytic ammonia decomposition for hydrogen production on ni, ru and niru supported on ceo2. *International Journal of Hydrogen Energy*, 44(25):12693–12707, 2019.

[54] Andrew L Dicks and David AJ Rand. *Fuel cell systems explained, chapter 5.1, p.135-137.* John Wiley & Sons, 2018.

[55] F Bidault, DJL Brett, PH Middleton, N Abson, and NP Brandon. A new application for nickel foam in alkaline fuel c-ells. *International journal of hydrogen energy*, 34(16):6799–6808, 2009.

[56] Andrew L Dicks and David AJ Rand. *Fuel cell systems explained, chapter 5.3, p.147-150.* John Wiley & Sons, 2018.

[57] Middleton P.H. Bidault, F. *Comprehensive renewable energy, volume. 4, chapter 4.07.3, p. 185-190.* Elsevier, 2012.

[58] Patience C Ho, Donald A Palmer, and Robert H Wood. Conductivity measurements of dilute aqueous lioh, naoh, and koh solutions to high temperatures and pressures using a flow-through cell. *The Journal of Physical Chemistry B*, 104(50):12084–12089, 2000.

[59] Andrew L Dicks and David AJ Rand. *Fuel cell systems explained, chapter 1.4, p. 11-15.* John Wiley & Sons, 2018.

[60] AFC Energy. Hydrox-cell (l)™ - afc energy. `https://www.afcenergy.com/products/hydrox-cell_l/#`, May 2020.

[61] Andrew L Dicks and David AJ Rand. *Fuel cell systems explained, Appendix 1.1, p. 401-403.* John Wiley & Sons, 2018.

[62] Kuppan Thulukkanam. *Heat exchanger design handbook, chapter 6.2.1, p. 395-396.* CRC press, 2013.

[63] V Ahuja and RK Green. Co2 removal from air for alkaline fuel cells operating with liquid hydrogen—heat exchanger development. *International journal of hydrogen energy*, 21(5):415–421, 1996.

[64] J Wallace and S Krumdieck. Carbon dioxide scrubbing from air for alkaline fuel cells using amine solution in a packed bubble column. *Proceedings of the Institution of Mechanical Engineers, Part C: Journal of Mechanical Engineering Science*, 219(11):1225–1233, 2005.

[65] Karl Kordesch, Viktor Hacker, Klaus Reichmann, Martin Cifrain, Thomas Hejze, and Robert R Aronsson. The safe and economic revival of alkaline hydrogen/air fuel cells with circulating electrolytes, recommended for vehicles using battery hybrid systems and h2 from ammonia crackers. *ECS Transactions*, 11(32):167–185, 2008.

[66] Susan Krumdieck, Jamie Wallace, and Owen Curnow. Compact, low energy co2 management using amine solution in a packed bubble column. *Chemical Engineering Journal*, 135(1-2):3–9, 2008.

[67] Yunus Cengel. *Heat and mass transfer: fundamentals and applications, chapter 11.1, p. 650-653.* McGraw-Hill Higher Education, 2014.

[68] Andrew L Dicks and David AJ Rand. *Fuel cell systems explained, chapter 12.2.1, p. 366-368.* John Wiley & Sons, 2018.

[69] Alexandra Von Meier. *Electric power systems: a conceptual introduction, chapter 8.4, p.250-251.* John Wiley & Sons, 2006.

[70] Helge Weydahl. Dynamic behaviour of fuel cells, chapter 5.5, p. 83. 2006.

[71] AS Chellappa, CM Fischer, and WJ Thomson. Ammonia decomposition kinetics over ni-pt/al2o3 for pem fuel cell applications. *Applied Catalysis A: General*, 227(1-2):231–240, 2002.

[72] Karl Kordesch, Viktor Hacker, Robert Fankhauser, and Gottfried Faleschnin. Ammonia cracker for production of hydrogen, August 30 2005. US Patent 6,936,363.

[73] Viktor Hacker and Karl Kordesch. Ammonia crackers. *Handbook of fuel cells*, 2010.

[74] Alexandra Von Meier. *Electric power systems: a conceptual introduction, chapter 4.6, p.123-126*. John Wiley & Sons, 2006.

[75] Knut Brautaset. *Innføring i oljehydraulikk, chapter 4.3.2, p. 110-127*. Universitetsforl., 2004.

[76] Janne Koivumäki and Jouni Mattila. Adaptive and nonlinear model-based control of variable displacement pumps for variable loading conditions. In *2017 IEEE Conference on Control Technology and Applications (CCTA)*, pages 1967–1974. IEEE, 2017.

[77] Andrew L Dicks and David AJ Rand. *Fuel cell systems explained, chapter 12.1.1, p. 351-361*. John Wiley & Sons, 2018.

[78] Xiaohan Jia, Jiahao Chen, Han Wu, and Xueyuan Peng. Study on the diaphragm fracture in a diaphragm compressor for a hydrogen refueling station. *International Journal of Hydrogen Energy*, 41(15):6412–6421, 2016.

[79] O.R. Fossmark. *Roterende maskiner, vifter, kompressorer, pumper, vannkraftturbiner, vindturbiner, chapter 6, p. 6.1-6.50*. FoxForlag, Stavanger, Norway, 2006.

[80] Direktoratet for samfunnssikkerhet og beredskap. Temaveiledning om oppbevaring av farlig stoff, chapter. 4, p. 72, 2020.

[81] Yunus A Cengel and Michael A Boles. Thermodynamics: an engineering approach, 9th edition chapter. chapter 15.2, page 752-757, 2019.

[82] Andrew L Dicks and David AJ Rand. *Fuel cell systems explained, chapter 2.4, p. 35-36*. John Wiley & Sons, 2018.

[83] Young Eun Kim, Jin Ah Lim, Soon Kwan Jeong, Yeo Il Yoon, Shin Tae Bae, and Sung Chan Nam. Comparison of carbon dioxide absorption in aqueous mea, dea, tea, and amp solutions. *Bulletin of the Korean Chemical Society*, 34(3):783–787, 2013.

[84] RJ Gilliam, JW Graydon, DW Kirk, and SJ Thorpe. A review of specific conductivities of potassium hydroxide solutions for various concentrations and temperatures. *International Journal of Hydrogen Energy*, 32(3):359–364, 2007.

[85] Y Cengel. *Heat transfer - A practical approach, chapter 13.3, p. 678-680*. Mc-Graw Hill Education, Columbus, GA, USA, 2003.

[86] Sigurd Skogestad. *Chemical and energy process engineering, Chapter 5.2, p. 131-139*. CRC press, 2008.

[87] Bjørn Pedersen. Germain henri hess – store norske leksikon. `https://snl.no/Germain_Henri_Hess`, July 2013.

[88] Yunus A Cengel and Michael A Boles. Thermodynamics: an engineering approach, 9th edition chapter. chapter 15.3, page 758-762, 2019.

[89] Yunus A Cengel and Michael A Boles. Thermodynamics: an engineering approach, 9th edition chapter. chapter 15.4, page 762-767, 2019.

[90] Yunus A Cengel and Michael A Boles. Thermodynamics: an engineering approach, 9th edition chapter. appendix a, page 881-930, 2019.

[91] Lester Haar and John S Gallagher. Thermodynamic properties of ammonia, chapter. appendix b, p. 69. *Journal of Physical and Chemical Reference Data*, 7(3):635–792, 1978.

[92] Andrew L Dicks and David AJ Rand. *Fuel cell systems explained, appendix 2.6, p. 410*. John Wiley & Sons, 2018.

[93] Andrew L Dicks and David AJ Rand. *Fuel cell systems explained, chapter 2.1, p. 27-31*. John Wiley & Sons, 2018.

[94] Yunus A Cengel and Michael A Boles. Thermodynamics: an engineering approach, 9th edition chapter. chapter 6.6, page 288-291, 2019.

[95] Bjørn Pedersen. Gibbs fri energi – store norske leksikon. `https://snl.no/Gibbs_fri_energi`, June 2018.

[96] Andrew L Dicks and David AJ Rand. *Fuel cell systems explained, chapter 2.5.1, p. 36-38*. John Wiley & Sons, 2018.

[97] Anton Hauge. Partialtrykk – store norske leksikon. `https://snl.no/partialtrykk`, March 2020.

[98] Einar Jacobsen. Nernsts ligning – store norske leksikon. `https://snl.no/Nernsts_ligning`, April 2020.

[99] Andrew L Dicks and David AJ Rand. *Fuel cell systems explained, chapter 3.3, p. 46*. John Wiley & Sons, 2018.

[100] Andrew L Dicks and David AJ Rand. *Fuel cell systems explained, chapter 3.5, p. 52-54*. John Wiley & Sons, 2018.

[101] Andrew L Dicks and David AJ Rand. *Fuel cell systems explained, chapter 3.8, p. 57*. John Wiley & Sons, 2018.

[102] Andrew L Dicks and David AJ Rand. *Fuel cell systems explained, chapter 3.4.1, p. 46-48*. John Wiley & Sons, 2018.

[103] Andrew L Dicks and David AJ Rand. *Fuel cell systems explained, chapter 3.4.2, p. 48-51*. John Wiley & Sons, 2018.

[104] Andrew L Dicks and David AJ Rand. *Fuel cell systems explained, chapter 3.6, p. 54-55.* John Wiley & Sons, 2018.

[105] Andrew L Dicks and David AJ Rand. *Fuel cell systems explained, chapter 3.7, p. 55-57.* John Wiley & Sons, 2018.

[106] FuelSaver-MPG Inc. Koh freezing temps. `https://www.fuelsaver-mpg.com/koh-freezing-temps`, June 2020.

[107] Knut Brautaset. *Innføring i oljehydraulikk, chapter 4.1, p. 83-87.* Universitetsforl., 2004.

[108] Theodore Wildi et al. *Electrical machines, drives, and power systems, chapter 13.13, p. 278-281.* 2014.

[109] Dragan Jovcic. Step-up dc–dc converter for megawatt size applications. *IET Power Electronics*, 2(6):675–685, 2009.

[110] ABB. Abb megawatt solar station. `https://www.fuelsaver-mpg.com/koh-freezing-temps`, June 2020.

[111] Qing-he Luo, Bai-gang Sun, and Hua-yu Tian. The characteristic of polytropic coefficient of compression stroke in hydrogen internal combustion engine. *International journal of hydrogen energy*, 39(25):13787–13792, 2014.

[112] O.R. Fossmark. *Roterende maskiner, vifter, kompressorer, pumper, vannkraftturbiner, vindturbiner, chapter 8, p. 8.1-8.24.* FoxForlag, Stavanger, Norway, 2006.

[113] O.R. Fossmark. *Roterende maskiner, vifter, kompressorer, pumper, vannkraftturbiner, vindturbiner, chapter 10, p. 10.1-10.38.* FoxForlag, Stavanger, Norway, 2006.

[114] O.R. Fossmark. *Roterende maskiner, vifter, kompressorer, pumper, vannkraftturbiner, vindturbiner, chapter 9, p. 9.1-9.28.* FoxForlag, Stavanger, Norway, 2006.

[115] David Connolly, Henrik Lund, Brian Vad Mathiesen, and Martin Leahy. A review of computer tools for analysing the integration of renewable energy into various energy systems. *Applied energy*, 87(4):1059–1082, 2010.

[116] Kværner. A small step towards zero emission shipping. `https://www.kvaerner.com/a-small-step-towards-zero-emission-shipping/`, July 2020.

[117] Kyrre Sundseth Anders Ødegård Geir Magnar Brekke, Steffen Møller-Holst and Dag Ivar Brekke. Fornybar energiforsyning til svalbard - longyearbyen, chapter 1, p. 5. `https://www.statkraft.com/globalassets/explained/svalbard_rapport_0911_final.pdf/`, November 2018.

[118] Kyrre Sundseth Anders Ødegård Geir Magnar Brekke, Steffen Møller-Holst and Dag Ivar Brekke. Fornybar energiforsyning til svalbard - longyearbyen, chapter 9, p. 25-28. `https://www.statkraft.com/globalassets/explained/svalbard_rapport_0911_final.pdf/`, November 2018.

[119] Kyrre Sundseth Anders Ødegård Geir Magnar Brekke, Steffen Møller-Holst and Dag Ivar Brekke. Fornybar energiforsyning til svalbard - longyearbyen, chapter 10, p. 29-30. https://www.statkraft.com/globalassets/explained/svalbard_rapport_0911_final.pdf/, November 2018.

[120] H.Hisdal S.Mayer-A.B.Sandø A.Sorteberg I.Hanssen-Bauer, E.J.Førland. Climate in svalbard - a knowledge base for climate adaption, nccs report 1/2019, commisioned by miljødirektoratet, chapter 7.1, p. 113-118. https://www.miljodirektoratet.no/globalassets/publikasjoner/M1242/M1242.pdf?fbclid=IwAR3r735a_UW8rgBnlDjUEfd9vfHXgk4lTXnnugMmDXaXV2JhqTFe6vY26pk, January 2019.

[121] Yunus Cengel. *Heat and mass transfer: fundamentals and applications, chapter 13.5, p. 690-700.* McGraw-Hill Higher Education, 2014.

[122] Viorel Badescu. Optimal design and operation of ammonia decomposition reactors. *International Journal of Energy Research.*

Norges miljø- og biovitenskapelige universitet
Noregs miljø- og biovitskapelege universitet
Norwegian University of Life Sciences

Postboks 5003
NO-1432 Ås
Norway